REPORT DOCUMENTATION PAGE

1

Form Approved OMB NO. 0704-0188

1. REPORT DATE (DD-MM-YYYY)	2. REPORT TYPE	3. DATES COVERED (From - To)
31-08-2014	Ph.D. Dissertation	-

4. TITLE AND SUBTITLE	5a. CONTRACT NUMBER
Magnetic Field Sensing with Nitrogen Vacancy Color Centers in Diamond	W911NF-11-1-0400
	5b. GRANT NUMBER
	5c. PROGRAM ELEMENT NUMBER
	611103

6. AUTHORS	5d. PROJECT NUMBER
Linh My Pham	
	5e. TASK NUMBER
	5f. WORK UNIT NUMBER

7. PERFORMING ORGANIZATION NAMES AND ADDRESSES	8. PERFORMING ORGANIZATION REPORT NUMBER
Massachusetts Institute of Technology (MIT 77 Massachusetts Ave. NE18-901 Cambridge, MA 02139 -4307	

9. SPONSORING/MONITORING AGENCY NAME(S) AND ADDRESS (ES)	10. SPONSOR/MONITOR'S ACRONYM(S) ARO
U.S. Army Research Office P.O. Box 12211 Research Triangle Park, NC 27709-2211	11. SPONSOR/MONITOR'S REPORT NUMBER(S) 59745-PH-MUR.83

12. DISTRIBUTION AVAILIBILITY STATEMENT

Approved for public release; distribution is unlimited.

13. SUPPLEMENTARY NOTES

The views, opinions and/or findings contained in this report are those of the author(s) and should not contrued as an official Department of the Army position, policy or decision, unless so designated by other documentation.

14. ABSTRACT

In recent years, the nitrogen-vacancy (NV) center has emerged as a promising magnetic sensor capable of measuring magnetic fields with high sensitivity and spatial resolution under ambient conditions. This combination of characteristics allows NV magnetometers to probe magnetic structures and systems that were previously inaccessible with alternative magnetic sensing technologies. This dissertation presents and discusses a number of the initial efforts to demonstrate and improve NV magnetometry. In particular, a wide-field CCD based NV magnetic field imager capable of micron-scale spatial resolution is demonstrated; and magnetic field alignment

15. SUBJECT TERMS

QuISM

16. SECURITY CLASSIFICATION OF:			17. LIMITATION OF ABSTRACT	15. NUMBER OF PAGES	19a. NAME OF RESPONSIBLE PERSON
a. REPORT	b. ABSTRACT	c. THIS PAGE			Paola Cappellaro
UU	UU	UU	UU		19b. TELEPHONE NUMBER 617-253-8137

Report Title

Magnetic Field Sensing with Nitrogen Vacancy Color Centers in Diamond

ABSTRACT

In recent years, the nitrogen-vacancy (NV) center has emerged as a promising magnetic sensor capable of measuring magnetic fields with high sensitivity and spatial resolution under ambient conditions. This combination of characteristics allows NV magnetometers to probe magnetic structures and systems that were previously inaccessible with alternative magnetic sensing technologies. This dissertation presents and discusses a number of the initial efforts to demonstrate and improve NV magnetometry. In particular, a wide-field CCD based NV magnetic field imager capable of micron-scale spatial resolution is demonstrated; and magnetic field alignment, preferential NV orientation, and multipulse dynamical decoupling techniques are explored for enhancing magnetic sensitivity. The further application of dynamical decoupling control sequences as a spectral probe to extract information about the dynamics of the NV spin environment is also discussed; such information may be useful for determining optimal diamond sample parameters for different applications. Finally, several proposed and recently demonstrated applications which take advantage of NV magnetometers' sensitivity and spatial resolution at room temperature are presented; with particular focus on bio-magnetic field imaging.

Magnetic Field Sensing with Nitrogen-Vacancy Color Centers in Diamond

A dissertation presented

by

Linh My Pham

to

The School of Engineering and Applied Sciences

in partial fulfillment of the requirements

for the degree of

Doctor of Philosophy

in the subject of

Applied Physics

Harvard University

Cambridge, Massachusetts

May 2013

Thesis advisors   Author
Ronald Walsworth, Marko Lončar   **Linh My Pham**

Magnetic Field Sensing with Nitrogen-Vacancy Color Centers in Diamond

Abstract

In recent years, the nitrogen-vacancy (NV) center has emerged as a promising magnetic sensor capable of measuring magnetic fields with high sensitivity and spatial resolution under ambient conditions. This combination of characteristics allows NV magnetometers to probe magnetic structures and systems that were previously inaccessible with alternative magnetic sensing technologies

This dissertation presents and discusses a number of the initial efforts to demonstrate and improve NV magnetometry. In particular, a wide-field CCD based NV magnetic field imager capable of micron-scale spatial resolution is demonstrated; and magnetic field alignment, preferential NV orientation, and multipulse dynamical decoupling techniques are explored for enhancing magnetic sensitivity. The further application of dynamical decoupling control sequences as a spectral probe to extract information about the dynamics of the NV spin environment is also discussed; such information may be useful for determining optimal diamond sample parameters for different applications. Finally, several proposed and recently demonstrated applications which take advantage of NV magnetometers' sensitivity and spatial resolution at room temperature are presented, with particular focus on bio-magnetic field imaging.

Contents

Contents

Contents

List of Figures

Citations to Previously Published Work

A large portion of Chapter 3 has been published in the following paper:

"Coherence of Nitrogen-Vacancy Electronic Spin Ensembles in Diamond", P.L. Stanwix, L.M. Pham, J.R. Maze, D. Le Sage, T.K. Yeung, P. Cappellaro, P.R. Hemmer, A. Yacoby, M.D. Lukin, R.L. Walsworth. Phys. Rev. B 82, 201201(R) (2010).

A large portion of Chapter 4 has been published in the following paper:

"Magnetic field imaging with nitrogen-vacancy ensembles", L. M. Pham, D. Le Sage, P.L. Stanwix, T.K. Yeung, D. Glenn, A. Trifonov, P. Cappellaro, P.R. Hemmer, M.D. Lukin, H. Park, A. Yacoby R.L. Walsworth. New J. Phys. 13, 045021 (2011).

Chapter 5 has been published with minor changes as

"Enhanced metrology using preferential orientation of nitrogen-vacancy centers in diamond", L. M. Pham, N. Bar-Gill, D. Le Sage, C. Belthangady, A. Stacey, M. Markham, D. J. Twitchen, M. D. Lukin, R. L. Walsworth. Phys. Rev. B 86, 121202(R) (2012).

Chapter 6 combines work published in the following two papers:

"Enhanced solid-state multispin metrology using dynamical decoupling", L. M. Pham, N. Bar-Gill, C. Belthangady, D. Le Sage, P. Cappellaro, M. D. Lukin, A. Yacoby, R. L. Walsworth. Phys. Rev. B 86, 045214 (2012).

"Solid-state electronic spin coherence time approaching one second", N. Bar-Gill, L. M. Pham, A. Jarmola, D. Budker, R. Walsworth. Nat. Commun. 4, 1743 (2013).

Chapter 7 has been slightly modified from results published in the following paper:

"Suppression of spin-bath dynamics for improved coherence of multi-spin-qubit systems", N. Bar-Gill, L. M. Pham, C. Belthangady, D. Le Sage, P. Cappellaro, J. R. Maze, M. D. Lukin, A. Yacoby, R. Walsworth. Nat. Commun. 3, 858 (2012).

Acknowledgments

I have had the opportunity over the past six years to meet and work with many extraordinary people, and it is only thanks to their guidance, support, and friendship that I've accomplished anything at all in graduate school. First of all, I am incredibly grateful to my advisor, Ronald Walsworth, for his guidance in matters both scientific and professional, for his encouragement, and for his unending enthusiasm in the innumerably diverse research projects we have pursued. I admire him as a scientist, as a leader, and as a genuinely good and fun person to be around.

I am also sincerely grateful to the post-docs I've worked with over the years. Paul Stanwix and I built the first Walsworth Lab NV-diamond setup on a corner of an optics table in the the slowed- and stored-light room, and during the (long, dark) three month period between the first implementation of the experimental setup and our first measurement of a Rabi nutation, Paul taught me everything I know about aligning optics, thinking about problems systematically, and keeping a good sense of humor in the face of frustration.

David Le Sage has thought up so many useful improvements to our NV measurement techniques over the years; he has taught me again and again the importance of taking the time to step back and ask, "How can we make this better?" Also, his steadfastness and good humor (in addition, of course, to doing half the work) are the reason I got through the NV magnetic field imager demonstration and writing my first paper with any sanity left at all.

Nir Bar-Gill and I have worked together closely on four published works (represented in three chapters of this dissertation) and numerous other ongoing projects in the three years we've known each other. He is someone I go to for scientific questions, career guidance, personal advice, and everything in between. He reminds me to think of the bigger picture both in research and in life. And whether we're trying to figure out unexpectedly long nitrogen spin bath correlation times or troubleshooting an experiment from across the country or pulling a week of 16-hour days telling each other the same five jokes over and over again, he always, always, *always* makes me laugh. I count myself truly fortunate to have him as a co-worker, mentor, and friend.

In addition to Paul, David, and Nir with whom I've worked most closely, the Walsworth NV subgroup has grown considerably over the past five years, and I have worked with, learned from, and am grateful to everyone in it: Tsun Yeung, David Glenn, Alexei Trifonov, Chinmay Belthangady, Stephen DeVience, Keigo Arai, Huiliang Zhang, Jean-Christophe Jaskula, Anat Bar-Gill, Erik Bauch, and Maddy Corbett. I'd also like to thank the rest of the Walsworth Group in Team Astro-comb (David Phillips, Chih-Hao Li, Alex Glenday, and Nick Langellier) for providing an outside eye to keep us grounded and helping us with data analysis.

I am also grateful to have had the opportunity to collaborate with a very rich and active diamond community both within Harvard and around the world. In particular, I'd like to thank Matthew Markham, Alastair Stacey, and Daniel Twitchen at Element

Chapter 1

NV Background

1.1   Introduction

The nitrogen-vacancy (NV) color center in diamond has recently emerged as a promising candidate platform for a number of applications in quantum sensing, metrology, and information processing. In particular, the NV system possesses a combination of remarkable properties which make it well-suited for these applications. Chief among these properties is the addressability of the NV electronic spin state, which can be initialized via optical pumping, coherently manipulated by applying microwave (MW) fields and standard electron spin resonance (ESR) techniques, and optically detected from the spin-state-dependent fluorescence intensity. The NV electronic spin also exhibits long coherence times (T_2), even at room temperature; in fact, at $T_2 \approx 2$ ms [1, 2, 3], the NV center holds the record for longest room temperature coherence time of an electronic spin in a solid. Finally, the multitude of solid-state processing techniques that have been developed over the past fifty years by the semiconductor industry can be adapted for diamond. Standard semiconductor processes such as chemical vapor deposition (CVD), ion implantation, and annealing can all be applied to diamond in order to optimize NV concentration and spin impurity environment for a variety of different applications.

This dissertation focuses on the application of NV centers to magnetic field sensing, particularly with NV ensembles, though many of the techniques for improving magnetic sensitivity that are discussed are applicable to single centers as well. The rest of Chapter 1 provides a brief introduction to NV centers, including an overview of the processes by which NV centers may be formed in bulk diamond, the NV electronic structure, the standard techniques for manipulating and detecting the NV spin state, and the NV spin's interaction with its environment. Chapter 2 describes several measurement schemes for using NV centers to detect magnetic fields. The remaining

chapters present an initial demonstration of a CCD-based NV magnetic field imager (Chapter 4), discuss several approaches for improving NV magnetic sensitivity (Chapters 3, 5, 6), and demonstrate a spectral decomposition technique that can be applied to gain a better understanding of NV spin bath dynamics (Chapter 7). A brief summary of the current state of NV magnetic field sensing technology and a discussion of some promising applications are presented in Chapter 8.

1.2   NV Physical Structure

The NV center is a stable defect in diamond's crystal structure; it consists of a substitutional nitrogen atom and a vacancy on adjacent lattice sites, such that the defect's symmetry axis may be oriented along one of four possible crystallographic directions (see Figure 1.1). These four NV orientation classes are almost always equally populated; however, preferential NV orientation has been observed in some CVD-grown diamond samples (see Chapter 5).

The NV center exists predominantly in one of two charge states: the neutral NV^0 state and the negatively charged NV^- state. The NV^- charge state, which is believed to receive its additional electron from a nearby substitutional nitrogen atom [4, 5], is the charge state which possesses the myriad useful properties described in the previous section. As a result, the NV^- is more well-studied, and it is common in the literature to drop the charge notation, where NV is understood to refer to the negatively charged state of the defect. As the NV^- charge state is the main focus of the current work, this convention will be adopted for the remainder of this dissertation. It is important to note, however, that the NV^0 charge state remains an area of research both to obtain further insight into the NV^- charge state and to explore its suitability as another candidate spin system for various quantum applications [6].

1.3   NV Formation

Most of the diamond material used in industrial and research applications today is synthesized using one of two production methods. The high-pressure high-temperature (HPHT) method was first demonstrated by Tracy Hall at General Electric in 1954 [7] and, as its name suggests, involves growing diamond from a seed crystal under high pressure ($> 50,000$ bar) and high temperature ($> 1400°C$) conditions, where diamond is the stable allotrope of carbon. HPHT synthesis allows for the mass production of high-quality diamond at relatively low cost and is therefore widely used in industrial applications.
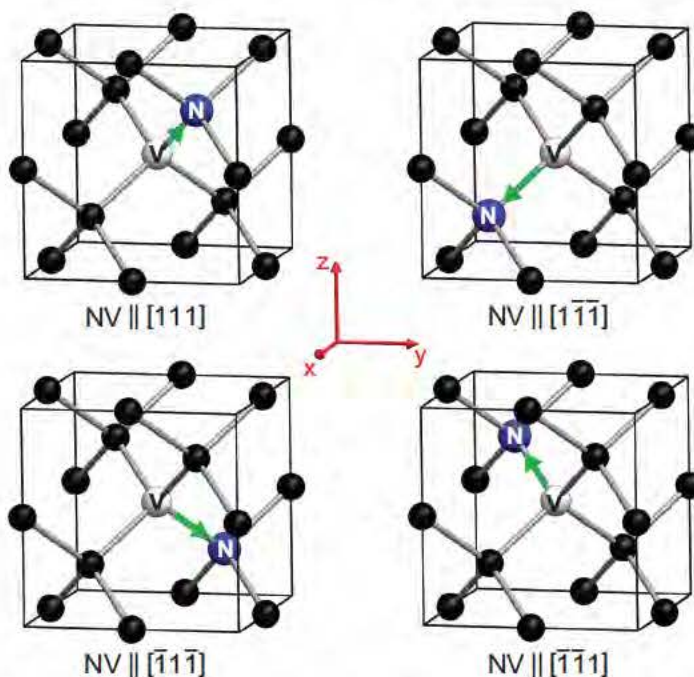
Figure 1.1: Four orientations of the NV center in diamond. Carbon atoms are depicted in black, nitrogen (N) atoms in blue, and vacancies (V) in white. The NV electronic spin is indicated by green arrows. Four additional orientations are possible by flipping the nitrogen atoms and vacancies in each configuration above; however, orientations with equivalent symmetry axes are spectrally indistinguishable and may therefore be considered in the same NV orientation class.

More recently, chemical vapor deposition (CVD) has emerged as another viable method for diamond production. In CVD synthesis, source gasses containing carbon are introduced into a growth chamber where they are energized to form a plasma that deposits carbon atoms onto a substrate. Compared to HPHT synthesis, CVD growth occurs at lower pressures ($0.01 - 1$ bar) and temperatures ($< 1000°C$), where the thermodynamically stable allotrope of carbon is graphite rather than diamond. However, by introducing hydrogen gas (H_2) in addition to carbon-providing methane gas (CH_4), any graphite deposits are rapidly and selectively etched, resulting in a net growth of diamond even under the described metastable conditions. Furthermore, CVD synthesis has a number of advantages over HPHT synthesis; diamonds can be grown over large areas and on different substrate materials. Also, the introduction of chemical impurities into the growth chamber can be finely controlled and so therefore can the properties of the diamond produced. These advantages make CVD the main synthesis technique for diamonds used in research applications.

One of the most common impurities found in diamond — both synthetic and

natural   is nitrogen, whether as a single substitutional defect (N_s), as part of a nitrogen-vacancy defect, or in larger complexes containing multiple nitrogen atoms and/or vacancies. A fair amount of research has been undertaken in recent years to increase the number of NV centers in diamond without increasing the concentration of other defects. This section briefly summarizes several common techniques applied for increasing NV concentration.

1.3.1   NV incorporation during CVD synthesis

Nitrogen impurities may be incorporated into diamond during CVD synthesis by flowing nitrogen gas (N_2) through the growth chamber. The majority of the resultant impurities are substitutional nitrogen defects (N_s); however a small fraction (typically $< 0.5\%$) form NV centers [8]. The concentration of nitrogen and NV defects that are incorporated into the diamond, as well as the diamond growth rate, growth mode, and surface morphology are determined by a combination of growth conditions: amount of nitrogen gas introduced into the growth chamber, substrate temperature, chamber pressure, etc. Better understanding of how these growth parameters are interrelated is the goal of much current CVD diamond research [9, 10, 11, 12, 13, 14, 8]. However, despite these open questions, Ohno et al. were recently able to CVD-grow a diamond containing a thin layer (~ 2 nm thick) of nitrogen-doped material on a high-purity substrate. By additionally electron-irradiating the sample and annealing, a fraction of the nitrogen defects in the thin layer were converted to NV centers [15]. The geometry of a thin NV-layer at the surface of a high-purity diamond is quite useful for a number of NV applications and, until this demonstration, had only been achieved using nitrogen ion implantation (discussed in the next section). Furthermore, the NV centers in these CVD nitrogen "delta-doped" layers are reported to exhibit less depth dispersion as well as better and more consistent spin coherence properties than those created via nitrogen ion implantation [15].

1.3.2   Nitrogen ion implantation and annealing

As mentioned previously, NV centers may also be introduced into diamond by implanting nitrogen ions, most commonly N^+ and N_2^+. These ion species often consist of ^{15}N isotopes in order to distinguish NV centers formed via ion implantation from native NV centers, which contain the more naturally abundant (99.6%) ^{14}N isotope. Other implant parameters which may be varied include ion fluence and implantation time to determine the total nitrogen dose, implantation energy to determine the depth and straggle of ions in the resulting implant layer, and substrate temperature during implantation. Optimizing these parameters to achieve stable NV centers and high N-to-NV conversion efficiency has been the subject of much study in recent years and

remains an area of open research [16, 17, 18, 19, 20]; several key topics of this research area are discussed below.

The implanted ion mean depth and straggle are functions of the ion species, implantation energy, and target material. The Stopping and Range of Ions in Matter (SRIM) software [21] is used almost exclusively to simulate ion implantation not only for diamond but also in the greater semiconductor community. However, there is one important caveat to consider when using SRIM: the software does not take into account crystalline structure (i.e., it assumes amorphous target material). As a result, channeling effects in crystals likely result in deeper implants than predicted; in fact, experimental evidence for this has been recently demonstrated in diamond [22, 23]). One suggested way to avoid these channeling effects is to implant with a small incidence angle; however, a systematic study in diamond of the actual implant depth compared to the depth predicted by SRIM simulations has still yet to be performed, due in part to the difficulty in determining the absolute distance between an NV center and the diamond surface with nanometer-scale resolution.

The bombardment of the diamond substrate with nitrogen ions during the implantation step performs the dual role of introducing nitrogen impurities into the diamond and damaging the crystal structure to form vacancies. Subsequent annealing of the sample above 600°C mobilizes the vacancies, which tend to become trapped adjacent to substitutional nitrogen impurities, thus relieving crystal strain due to the slight difference in the atomic radius of nitrogen compared to carbon. As with the implantation step, a number of parameters during the anneal may be varied to optimize NV stability and N-to-NV conversion efficiency (discussed in more detail in the next section).

Forming NV centers via ion implantation has several advantages over forming NV centers by nitrogen doping during CVD diamond growth. Ion implantation allows for more fine control over the dopant dosage and, until recently, the depth and thickness of the dopant layer as well. Also, despite the recent progress demonstrating a nanometers-thick delta-doped nitrogen layer in CVD-grown diamond [15], much work remains to make the process as reproducible, tunable in terms of layer thickness and nitrogen dosage, and widely available as ion implantation. Thus for now, ion implantation remains the far more accessible option for achieving thin shallow NV layers in diamond substrates. Furthermore, ion implantation allows NV centers to be positioned laterally with ~ 10 nm precision, which may achieved using a focused ion beam [16] or by masking off the diamond surface [24].

As mentioned in the previous section, there are also several disadvantages to ion implantation; implanted NV centers often exhibit poorer optical and spin properties compared to native NV centers. In particular, NV centers formed via ion implantation tend to be less photo-stable [25, 26, 27, 28], experience more photochromism (i.e., spend more time in the NV^0 charge state) [29, 25, 26, 27, 17, 28], and have shorter

spin coherence times [17, 30]. The exact causes of these issues are not definitively known; however, several possible culprits include crystal damage from the implantation, surface effects, and the formation of other defects. Better understanding of the ion implantation process will be necessary for improving the quality of implanted NV centers.

1.3.3   N-to-NV conversion

In both nitrogen-doped CVD diamond and high-purity diamond that has been implanted with nitrogen ions, substitutional nitrogen defects far outnumber NV centers. Despite efforts to optimize CVD growth conditions, the N-to-NV conversion efficiency achieved in as-grown CVD samples does not typically exceed 0.5% [8]. Efforts to improve N-to-NV conversion in implanted samples by optimizing implantation conditions [16, 31, 32, 18, 19] and annealing recipes [19] have been more successful, with a $\sim 50\%$ conversion efficiency demonstrated for very high nitrogen implantation energies ($> 2\,\mathrm{MeV}$) [16, 18]. However, the NV centers formed by these high-energy implants are located deeper in the diamond ($\gtrsim 1\mu\mathrm{m}$) with wider depth straggle ($\gtrsim 100$ nm) than is generally desired, and lower energy implants which create NV centers within 100 nm of the surface typically have lower N-to-NV conversion ($< 10\%$) [18].

For most NV applications, the expected optimum N-to-NV conversion efficiency is 50%, such that each substitutional nitrogen defect can donate its extra electron to an NV center in order to produce the more desirable negatively charged NV^- state. The limiting factor in NV yield for both implanted and as-grown CVD diamonds is believed to be the concentration of vacancies available in the crystal; as a result, a variety of processing techniques have been explored in recent years in order to create more vacancies and subsequently more NV centers. One popular approach is irradiation (e.g., electron, proton, and neutron) [33, 34, 35]; Another approach is implantation of additional ion species (e.g., He, Ni, C, Ga) [36, 25, 32, 17]. In particular, bombardment with carbon ions should cause damage to the crystal structure, thus forming vacancies without introducing unwanted impurities [17]. The balance in applying these various processing techniques lies in creating the proper concentration of vacancies without introducing other impurities into the crystal or forming defects that cannot be annealed out.

Regardless of whether the additional vacancies are introduced via irradiation or ion implantation, a subsequent anneal step is necessary in order to relieve crystal damage and to allow the vacancies to diffuse to substitutional nitrogen defects and form NV centers. As mentioned previously, there has been some effort in recent years to develop optimized annealing recipes. Vacancies become mobile at $\sim 600°\mathrm{C}$ [37] and as recently as five years ago, a standard annealing recipe consisting of a 2-hour anneal at $800°\mathrm{C}$ was thought to be sufficient to optimally create NV centers. However,

recent work has indicated that longer anneals may be needed to flush out unnecessary vacancies [38], or higher temperature anneals (e.g., up to 1200°) may be needed to break up other defects [17]. Developing processing recipes to achieve optimized N-to-NV conversion efficiency is a research topic of great import to NV ensemble magnetometry; improving N-to-NV conversion is expected to greatly enhance NV magnetic sensitivity, as discussed in detail in the next chapter.

1.4   NV Electronic Structure

This section presents a brief description of the NV center's electronic structure and behavior under optical excitation; for a more thorough discussion, refer to [39]. A simplified diagram of the NV center's energy level structure is depicted in Figure 1.2. There are six electrons associated with the negative charge state of the defect: three unpaired electrons from the three carbons nearest to the vacancy, a pair of electrons from the nitrogen (the other three valence electrons associated with the nitrogen form covalent bonds with the three carbons nearest to the nitrogen), and one extra electron believed to be donated from a nearby substitutional nitrogen defect. It is often simpler, however, to consider the NV center as having two holes rather than six electrons. As shown in Figure 1.2, the NV center's ground state is a spin-triplet with $^3A_2$ symmetry (C_{3v} point group), where the $m_s = 0$ ($|0\rangle$) and $m_s = \pm 1$ ($|\pm 1\rangle$) states experience a zero-field splitting ($D_{gs} \approx 2.87$ GHz) due to spin-spin interactions. Applying a small external magnetic field $B_{||}$ along the NV quantization axis lifts the degeneracy of the $|\pm 1\rangle$ energy levels with a Zeeman shift given by $\Delta = m_s \gamma B_{||}$, where the NV gyromagnetic ratio $\gamma = g\mu_B/h = 2.8$ MHz/G.

Optical transitions between the ground ($^3A_2$) and excited (^3E) triplet states have a characteristic zero-phonon line (ZPL) at 637 nm with a broad phonon-sideband ($640 - 800$ nm) at room temperature. These optical transitions are primarily spin conserving; however, there exists a primarily non-radiative alternative decay path which allows for the transfer of the spin population from the $|\pm 1\rangle$ state to the $|0\rangle$ state through the singlet states. The precise details of the singlet states including the exact number of singlet states, their symmetries, and their energies have been a source of contention for many years. The currently accepted model is that there are two singlets the lower state with ^1E symmetry and the upper state with $^1A_1$ symmetry separated by a 1043 nm ZPL. The energy spacing between the singlet and triplet states is, at the time of this writing, still unknown. For the purposes of describing the behavior of the NV spin state under optical excitation, it is often sufficient to treat the singlet states collectively as a manifold with an effective lifetime.

The resulting simplified electronic structure consists of five states, shown in Figure 1.3: the triplet ground $|0\rangle$ and $|\pm 1\rangle$ states ($|a\rangle$ and $|b\rangle$, respectively), the triplet
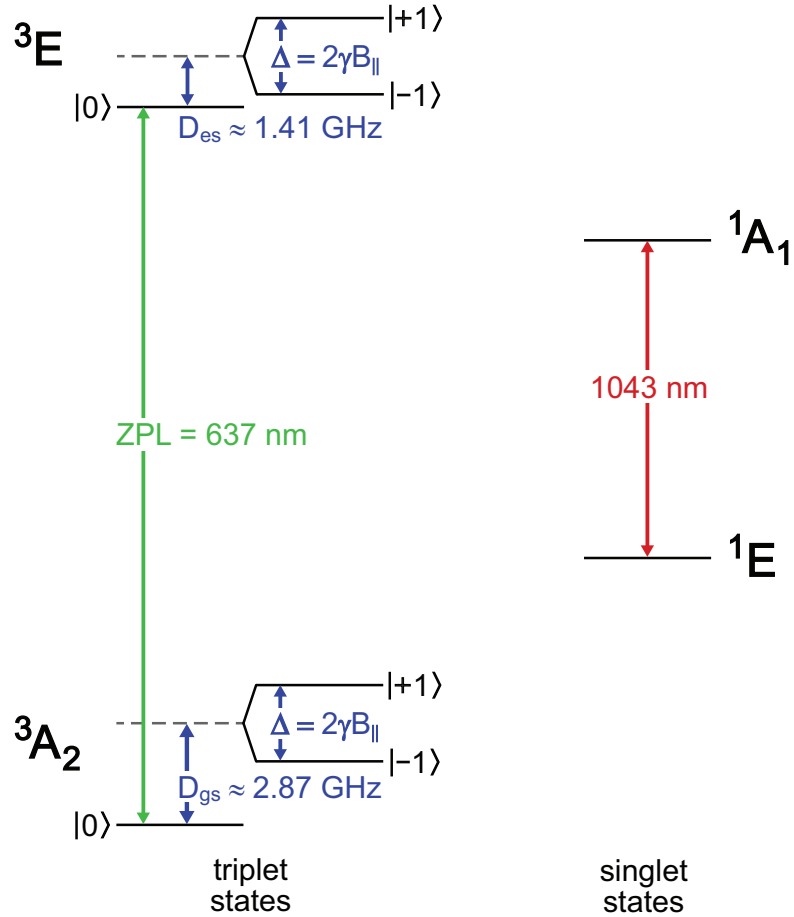
Figure 1.2: NV center electronic energy level structure at room temperature. The ground state, $^3A_2$, is a spin-triplet with a zero-field splitting $D_{gs} \approx 2.87$ GHz (1.2 μeV) between the $|0\rangle$ and $|\pm 1\rangle$ states. The excited triplet state, ^3E, has smaller a zero-field splitting $D_{es} \approx 1.41$ GHz (0.6 μeV) and is separated from the ground state by a 637 nm (1.945 eV) zero-phonon line. The $|\pm 1\rangle$ states experience additional splitting Δ proportional to the projection $B_{||}$ of an external magnetic field along the NV symmetry axis. The singlet states, ^1E and $^1A_1$, are separated by a 1043 nm (1.190 eV) zero-phonon line.
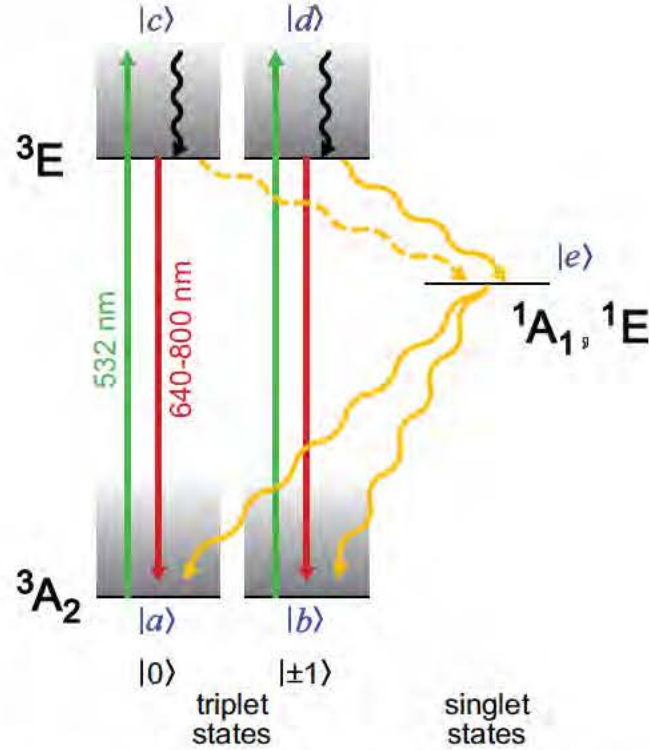
Figure 1.3: Behavior of the NV center under optical excitation described using an effective five-level system.

excited $|0\rangle$ and $|\pm1\rangle$ states ($|c\rangle$ and $|d\rangle$, respectively), and the singlet state manifold ($|e\rangle$). As mentioned previously, under above-band optical excitation, the cycling between the ground and excited states is primarily spin conserving, denoted by the solid red lines from $|c\rangle$ to $|a\rangle$ and $|d\rangle$ to $|b\rangle$. However, there exists a non-radiative decay path from excited states $|c\rangle$ and $|d\rangle$ to the metastable singlet manifold $|e\rangle$, which has an effective lifetime ~ 200 ns [40]. The transition rate from $|d\rangle$ to $|e\rangle$ is faster than the rate from $|c\rangle$ to $|e\rangle$, though the exact ratio of the transitions is not precisely known and likely dependent upon temperature, strain, and other extrinsic factors [39]. From the singlet manifold, the NV spin decays with approximately equal probability to either of the two ground states $|a\rangle$ and $|b\rangle$. As a result, continuous optical excitation will eventually pump the NV center into the $|0\rangle$ spin state, with maximum polarization determined by the ratio of decay rates from the spin sub-levels of ^{3}E ($|c\rangle$ and $|d\rangle$) to the single manifold $|e\rangle$. The degree of polarization reported in the literature most commonly falls in the range $80-95\%$ [41, 42, 30, 43, 44, 40]. Furthermore, since the alternate decay path does not result in the emission of a photon in the fluorescence band, the fluorescence intensity may be used to determine the spin state. At maximum optical driving (i.e., optical saturation, which corresponds to a

cycling frequency ~ 77 MHz), the time scale for optical pumping and subsequently the time scale over which the fluorescence intensity is integrated to determine the NV spin state is ~ 300 ns.

These key characteristics, which allow the NV center's electronic spin state to be initialized through optical pumping and detected via spin-state-dependent fluorescence, in combination with the ability to coherently manipulate the NV spin using conventional electron spin resonance techniques (discussed in the following sections), highlight the suitability of the NV center as a platform for applied magnetometry in a variety of areas, including biology, geology, and novel materials.

1.5 Coherent manipulation of NV spin state

This section describes several basic electron spin resonance (ESR) techniques that provide the foundation for coherent manipulation of the NV spin state.

1.5.1 Continuous-Wave Electron Spin Resonance Spectroscopy

To experimentally determine the NV spin resonances, simultaneous low intensity laser excitation (typically at 532 nm) and low power microwave (MW) radiation are applied. When the MW is off-resonant from all ground-state spin transitions, the MW driving has no effect and the laser excitation optically pumps the NV into the $|0\rangle$ spin state resulting in maximum fluorescence intensity. When the MW is resonant with one of the ground-state transitions, e.g., $|0\rangle \leftrightarrow |+1\rangle$, the spin state cycles between the $|0\rangle$ and $|+1\rangle$ states, reducing the fluorescence intensity. As a result, the NV resonances can be determined by sweeping the MW frequency and monitoring the NV fluorescence intensity.

When no magnetic field is applied, there is only one resonance at the zero-field splitting ≈ 2.87 GHz corresponding to the ground-state $|0\rangle \leftrightarrow |\pm 1\rangle$ transition [Figure 1.4(a)]. When a static magnetic field B_0 is applied along an arbitrary direction, the ESR spectrum of a single NV consists of two resonances: one corresponding to the ground-state $|0\rangle \leftrightarrow |-1\rangle$ transition and another corresponding to the ground-state $|0\rangle \leftrightarrow |+1\rangle$ transition. The splitting between the two resonances is determined by the projection of the magnetic field along the NV symmetry axis. In an ensemble measurement where the NV centers may occupy any of four possible orientation classes (Figure 1.1), the ESR spectrum may contain as many as eight transitions [Figure 1.4(b)]. At low enough laser intensities and MW powers, it is also possible to resolve the splitting due to Fermi contact hyperfine interactions between the NV electronic spin and the nuclear spin associated with the N in the NV complex, where $I = 1$ for ^{14}N [Figure 1.4(c)] and $I = 1/2$ for ^{15}N) [Figure 1.4(d)].
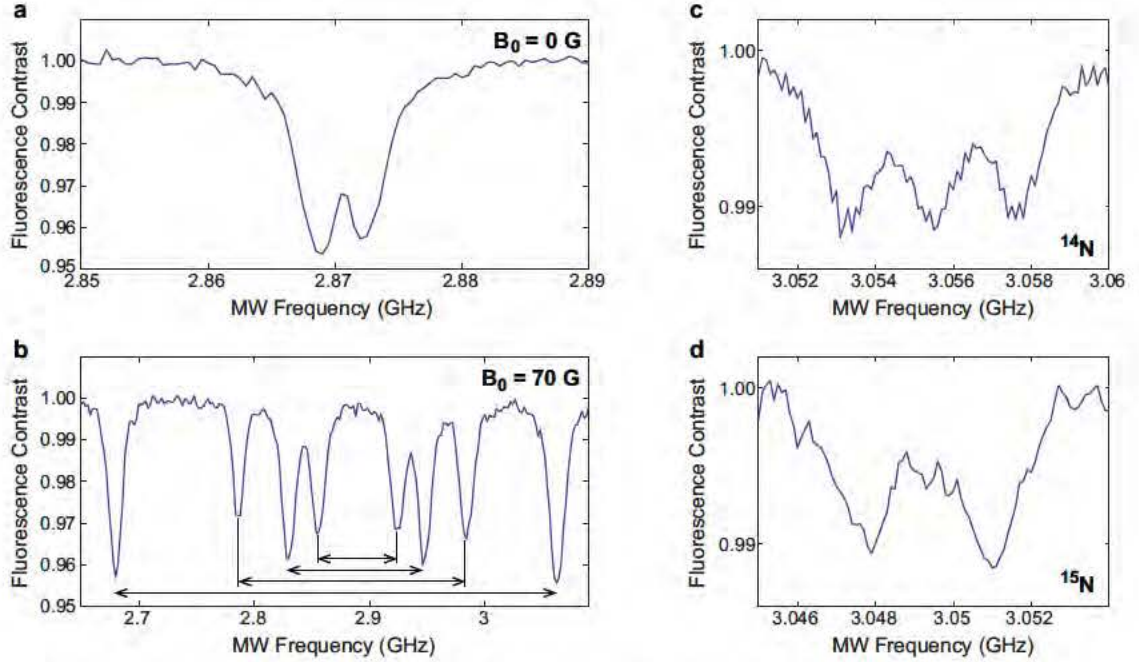
Figure 1.4: ESR spectra of NV ensembles. (a) ESR spectrum at zero applied static magnetic field. The small splitting is induced by local non-axial strain at the NV center [45, 1, 46, 47]. (b) ESR spectrum with an applied static magnetic field of ~ 65 G. The field is applied along an arbitrary direction, resulting in a different field projection on each of the four possible NV symmetry axes and subsequently four pairs of transitions. (c) Hyperfine-resolved ESR spectrum of a $|0\rangle \leftrightarrow |+1\rangle$ transition from an ^{14}N-containing NV ensemble. (d) Hyperfine-resolved ESR spectrum of a $|0\rangle \leftrightarrow |+1\rangle$ transition from an ^{15}N-containing NV ensemble.

1.5.2 Rabi Nutations

As mentioned previously, applying MW driving resonant with one of the ground-state transitions, e.g., $|0\rangle \leftrightarrow |+1\rangle$, induces coherent population oscillations between the two spin sublevels. The standard pulse sequence for measuring these population oscillations, known in conventional magnetic resonance nomenclature as Rabi nutations, is shown in Figure 1.5(a).

First, an optical excitation pulse polarizes the NV spin state to $|0\rangle$. Then, a resonant MW pulse coherently transfers the NV spin population between, e.g., the $|0\rangle$ and $|+1\rangle$ states, and the resultant NV spin state is subsequently detected by measuring the fluorescence intensity which results from a short (~ 300 ns at optical saturation) optical excitation pulse.

The degree of population transfer is a function of both the length and amplitude
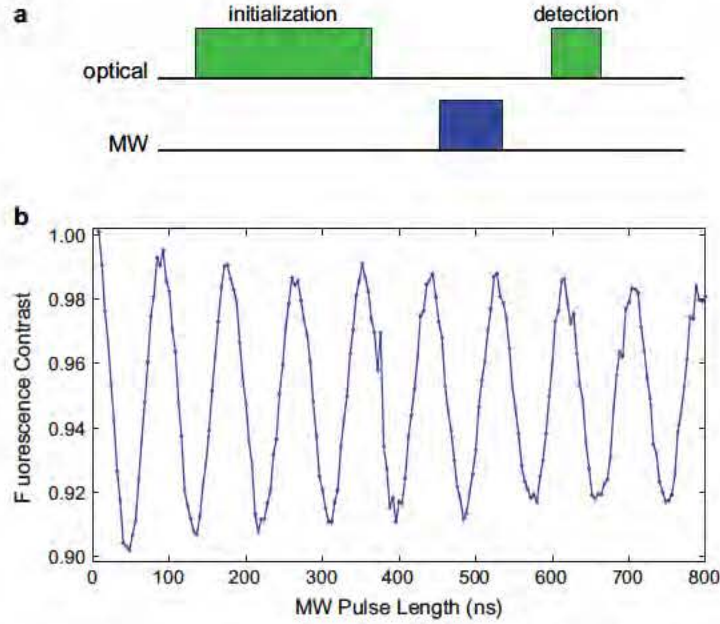
Figure 1.5: (a) Pulse sequence for measuring Rabi nutations. (b) Typical Rabi curve of an NV ensemble, where the fluorescence intensity is normalized against the fluorescence intensity measured after optical pumping.

of the MW pulse; in most NV experiments, however, varying only the MW pulse length is sufficient. An example of a typical Rabi curve is shown in Figure 1.5(b), where the normalized fluorescence intensity is plotted as a function of MW pulse length. Maximum fluorescence intensity corresponds to the NV spin population occupying the $|0\rangle$ state, whereas minimum fluorescence intensity corresponds to the NV spin population occupying the $|+1\rangle$ state (in this example). Therefore, by applying a series of MW pulses of specific lengths, the NV spin state can be coherently manipulated for a vast array of more complicated pulse sequences, as discussed in the following section.

It is important to note that Rabi nutations do not continue indefinitely. There is decay of the Rabi signal due to inhomogeneous broadening, and particularly, there is often beating due to the detuned driving of one or more hyperfine transitions associated with the N nuclear spin of the NV (see Figure 1.6). An in depth discussion of these effects is beyond the scope of this dissertation; however, NV Rabi nutations have been studied in great depth in other works [48]. In general, these effects can be mitigated by strong MW driving such that the Rabi nutation frequency is much larger than hyperfine detunings (~ 2 MHz) and inhomogeneous broadening (depends on the sample and may vary from ~ 100 kHz - 10 MHz). The Rabi nutation frequency
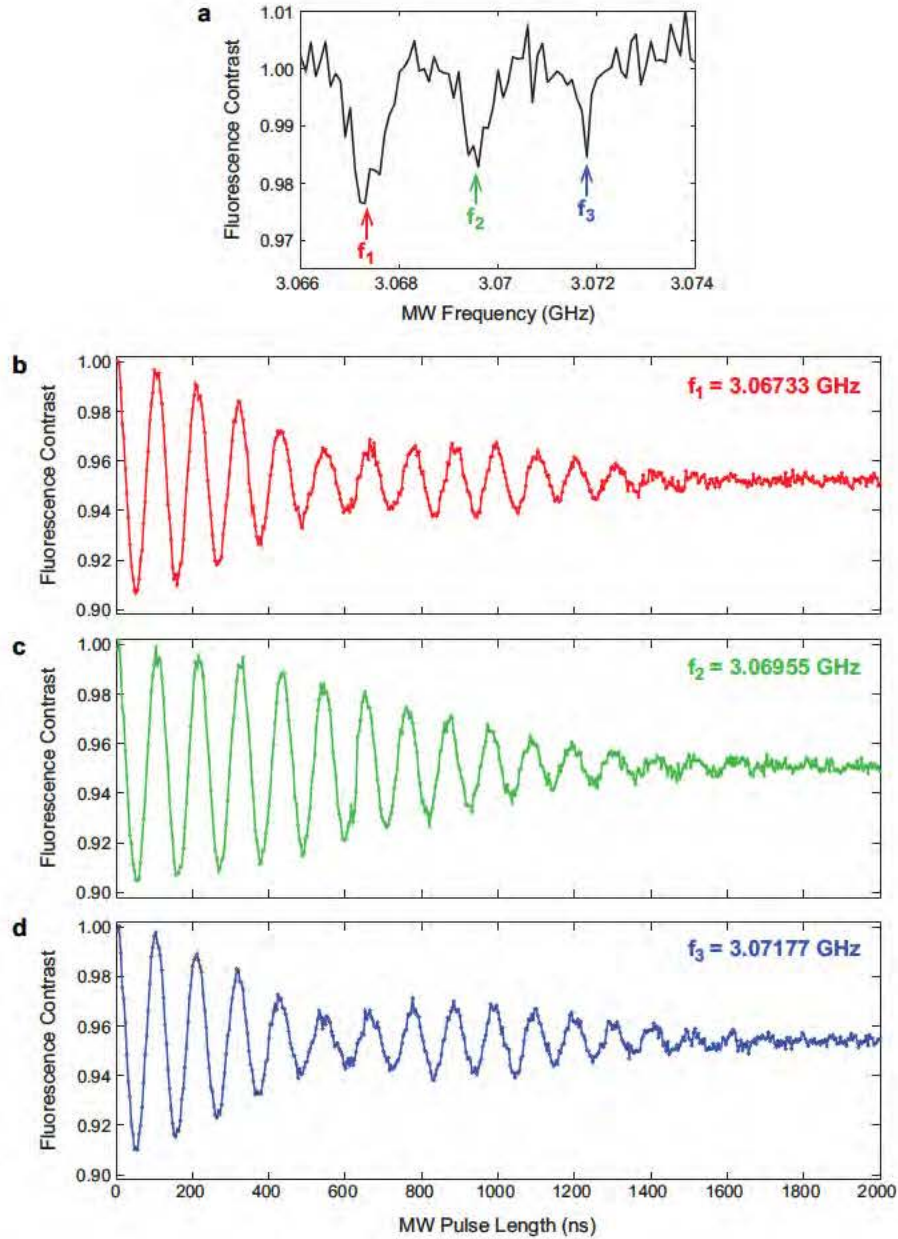
Figure 1.6: Rabi nutation decay at different MW drive frequencies. (a) Hyperfine-resolved ESR spectrum of a $|0\rangle \leftrightarrow |+1\rangle$ transition from an ^{14}N-containing NV ensemble. (b-d) Rabi nutations produced by resonantly driving each hyperfine transition with equal $B_1 \approx 4$ G.

Ω is given by the following equation:

$$\Omega = \gamma B_1 \tag{1.1}$$

where $\gamma = 2.8$ MHz/G is the gyromagnetic ratio of the NV electronic spin and B_1 is the component of the MW excitation perpendicular to the N-V symmetry axis.

1.6 NV spin dephasing, decoherence, and relaxation

Many proposed NV applications (e.g., quantum sensing, metrology, and information processing) rely on the ability to coherently manipulate the NV center's spin state. However, in addition to these applied MW excitation pulses, the NV spin state also experiences perturbations due to interactions with other spin impurities in the environment. The most common impurities encountered are the non-zero nuclear spins of the ^{13}C isotope, which comprise 1.1% of carbon in natural abundance; the electronic spins associated with nitrogen donors not incorporated into NV centers; and, in special cases (involving isotopic engineering and high N-to-NV conversion efficiency), other NV spins. Interactions with these spin impurities can cause dephasing and decoherence of the NV spin, characterized by T_2^* and T_2 respectively.

The NV spin may also interact with lattice phonons, resulting in spin flips and subsequent population decay (i.e., spin-lattice relaxation) on a time scale characterized by T_1. These spin-flip processes are a strong function of temperature and may also have a non-negligible effect on the NV spin decoherence as discussed in Chapter 6. This section briefly describes the major contributions to these characteristic time scales (T_2^*, T_2, and T_1) and how each is measured using the conventional ESR techniques described previously

1.6.1 T_2^* spin dephasing time

In the umbrella field of magnetic resonance, which includes nuclear magnetic resonance (NMR), electron spin resonance (ESR), and magnetic resonance imaging (MRI), the time scale over which dephasing occurs for the central spin or spin ensemble is characterized as the T_2^* time. In general, this dephasing occurs as a result of inhomogeneities in the environment; in the particular case of the NV spin, the dominant inhomogeneities are variations in local spin environment experienced by each NV center as well as temporal fluctuations in each NV center's local magnetic field due to dynamics in the surrounding spin bath.

For a standard sample with a natural 1.1% abundance of ^{13}C, dipolar hyperfine coupling with the non-zero ^{13}C nuclear spin is the dominant source of NV spin dephasing. The nuclei precess in the presence of magnetic fields which are created by
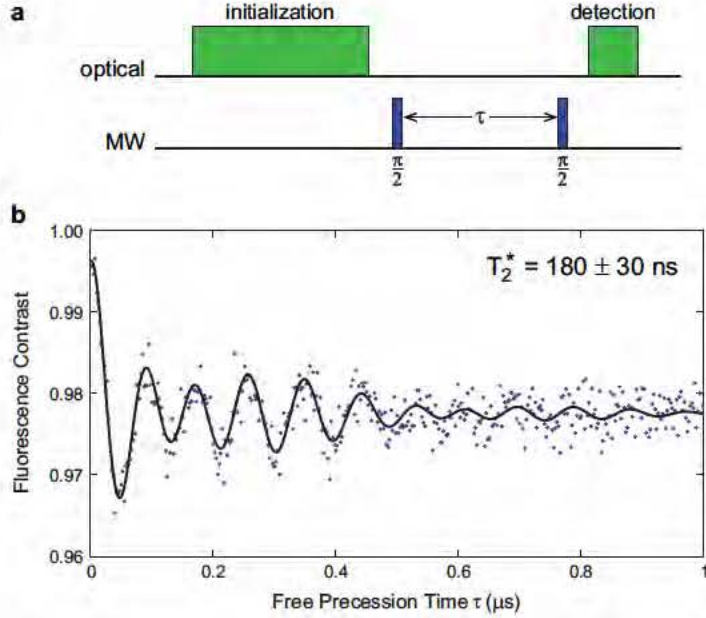
Figure 1.7: T_2^* measurement of a single NV center using a Ramsey pulse sequence. (a) Ramsey pulse sequence. (b) NV free induction decay curve from which $T_2^* \approx 180$ ns can be extracted.

local magnetic impurities or externally applied, producing random-phase time varying fields at each NV spin. Furthermore, each NV spin has a different local environment of spins and subsequently experiences a different local magnetic field. For natural isotopic abundance of ^{13}C (1.1%), the ^{13}C contribution to the NV spin dephasing rate has been measured experimentally both for single NV centers and ensembles to be $\Gamma_{^{13}C} \sim 10^6$ s^{-1}, corresponding to $T_2^* \sim 1\,\mu$s [49, 34, 1, 50, 51].

In samples that have been doped with a sufficient concentration of nitrogen, dipolar interactions with nitrogen-donated electrons can also contribute significantly to NV spin dephasing. This contribution is dependent on the nitrogen concentration n_N by $\Gamma_N \approx (g_s\mu_B)^2 n_N$ [52, 34], where small differences in the g-factors associated with the N and NV electronic spins are ignored. Therefore, a nitrogen concentration of ~ 15 ppm ($\sim 3 \times 10^{18}$ cm^{-3}) would have a contribution to the NV spin dephasing comparable to that of natural abundance ^{13}C. A possibility that has been pursued in recent years for extending T_2^* past a microsecond has been to isotopically engineer high-purity (low nitrogen) diamond with below natural abundance of ^{13}C. In a sample containing 99.7% ^{12}C, a dephasing time of $T_2^* > 10\,\mu$s was measured. [1].

The T_2^* is typically measured experimentally in one of two ways, described in detail below. One method is to apply a Ramsey pulse sequence and extract the characteristic time of the free induction decay (FID) curve. A typical Ramsey pulse
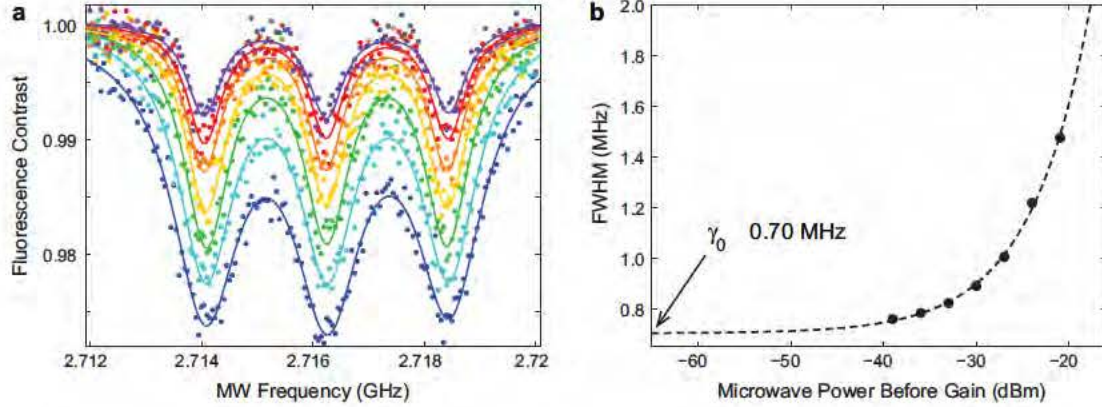
Figure 1.8: T_2^* measurement of an NV ensemble using CW-ESR. (a) ESR spectra taken at different MW powers and non-zero static magnetic field. (b) Linear extrapolation of the value of the FWHM γ at zero MW power gives a dephasing time $T_2^* \approx 500$ ns.

sequence is depicted in Figure 1.7(a); first, an optical excitation pulse initializes the NV spin state to $|0\rangle$. Then, a MW $\pi/2$ pulse (typically detuned from resonance by δ) transfers the NV spin population into a superposition of, e.g., the $|0\rangle$ and $|+1\rangle$ states. After a time τ during which the spin system is allowed to freely precess (and dephase), a second MW $\pi/2$ pulse projects the NV spin back into the $|0\rangle, |+1\rangle$ basis, and the NV spin-state is subsequently detected by measuring the state-dependent fluorescence intensity. Varying the free precession time yields an FID curve, which contains beating from the N hyperfine transitions (three in the case of ^{14}N, two in the case of ^{15}N). The T_2^* is extracted from characteristic time of the decay envelope, as shown in Figure 1.7(b).

For an ensemble of NV centers, inhomogeneities stemming from the different local spin environments experienced by each NV center often broaden the hyperfine transition frequency components of the Ramsey FID to the extent that it becomes difficult to extract T_2^* from the curve. An alternative method for measuring the dephasing time T_2^* is to take ESR spectra at low optical power, extract the full-width at half maximum (FWHM) of the resonances at progressively lower MW powers, and use the values to linearly extrapolate the FWHM at zero MW power. In Figure 1.8, a series of ESR spectra taken at different MW powers are shown, each fit with a linear combination of three Lorentzian functions, from which the FWHM γ was extracted. Extrapolating the value of the FWHM γ at zero MW power gives the dephasing time, which is related to the FWHM by $T_2^* = \frac{1}{\pi\gamma}$ [34].

1.6.2 T_2 spin decoherence time

Whereas T_2^* is the characteristic time for inhomogeneous spin dephasing, the T_2 time is the characteristic time for homogeneous spin dephasing, more commonly referred to as spin decoherence. In particular, while T_2^* is sensitive to external inhomogeneities, such as in applied static and MW fields, T_2 is intrinsic to the NV center and its local spin environment and is often referred to as spin-spin relaxation in conventional NMR nomenclature. As with inhomogeneous spin dephasing, the major contributors to NV spin decoherence are interactions with ^{13}C nuclear spins, nitrogen electron spins, and possibly other NV spins.

The NV spin coherence time T_2 is typically measured using a spin echo (also occasionally known as a Hahn echo) pulse sequence, shown in Figure 1.9(a). It is simply an extension on the Ramsey pulse sequence: after the NV spin is prepared in a coherent superposition of, e.g., $|0\rangle$ and $|+1\rangle$, local magnetic fields cause a phase accumulation during the first free precession interval $\tau/2$. However, when the local magnetic field fluctuations are slow on the time scale of the free precession interval $\tau/2$, the MW π pulse inverts the accumulated phase such that the same amount of phase is accumulated over the second free precession interval τ, thus "refocusing" the net phase and ideally eliminating the net phase shift. The efficacy of the refocusing is dependent on how slow the magnetic field fluctuations are in comparison to the free precession interval; faster fluctuations result in less perfect refocusing. A typical NV spin decoherence curve is shown in Figure 1.9; in this and most other coherence measurements presented in this dissertation, the pulse sequence is applied once with the last $\pi/2$ MW pulse along the x axis (m_1) and again with the last $\pi/2$ MW pulse along the -x axis (m_2). The signals are then subtracted and normalized [$s = (m_1 - m_2)/(m_1 + m_2)$] in order to reject common-mode noise (e.g., optical excitation laser intensity fluctuations). For a more detailed and quantitative description of this pulse sequence, see [53].

We now consider the major contributors to spin decoherence in NV centers. As mentioned in the previous section, the Larmor precession of ^{13}C nuclei is the dominant source of local magnetic field fluctuations in most natural abundance samples (excepting those with high nitrogen concentrations); however, when the free precession time τ is equal to a multiple number of ^{13}C Larmor periods, phase contributions from each individual ^{13}C cancel out, leading to collapses and revivals in the observed decoherence curve [see Figure 1.9(b)]. Thus, the true NV spin decoherence is given by the decay of the envelope of Larmor-resonant peaks in the ^{13}C-induced revivals, which in a ^{13}C-dominated sample arises from dipole-dipole coupling and spin-diffusion between the ^{13}C nuclear spins and has a time scale $T_2 \sim 600\,\mu$s. These spin dynamics will be discussed in greater detail in Chapter 3.

The other typical dominant sources of NV spin decoherence are paramagnetic
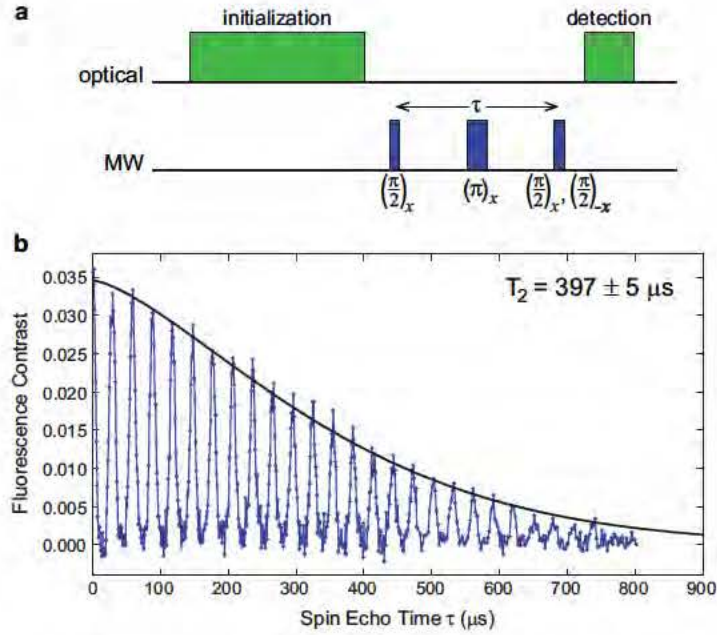
Figure 1.9: T_2 measurement of an NV ensemble using a spin echo pulse sequence. (a) Spin echo pulse sequence. (b) Typical T_2 decoherence curve of an NV ensemble in a commercially available standard grade CVD diamond sample from Element Six, showing the characteristic collapses and revivals in NV spin coherence that result from ^{13}C Larmor precession in the presence of a magnetic field. The NV spin coherence time T_2 is extracted from the decay envelope.

spins, such as electron spins associated with nitrogen donors (or possibly other NV centers and defects in the sample). These electron spins fluctuate on a time scale given by dipole-dipole interactions with the NV spin, described in the previous section by the equation $\Gamma_N \approx (g_s \mu_B)^2 n_N$. It is in this way that the nitrogen concentration has an enormous impact on the NV spin coherence time. Higher nitrogen concentration is required for higher NV concentration but results in lower NV coherence time. (For example, a sample with N $\sim$ 20 ppm has nitrogen-limited $T_2 \sim 5\ \mu$s.) Both high NV concentrations and long NV coherence times are desirable for maximizing the sensitivity of an NV-based magnetometer, as discussed in Chapter 2.

One technique common in conventional NMR for extending coherence is to apply additional MW π pulses to further decouple the central spin from magnetic impurities in its environment. More detailed discussion of these multipulse "dynamic decoupling" techniques will be presented in Chapter 6. However, it is useful to note here that while in conventional NMR the spin coherence time T_2 often refers to the intrinsic limit of how much the coherence can be extended using multipulse sequences, in the NV literature the T_2 time often refers specifically to the characteristic decoherence time
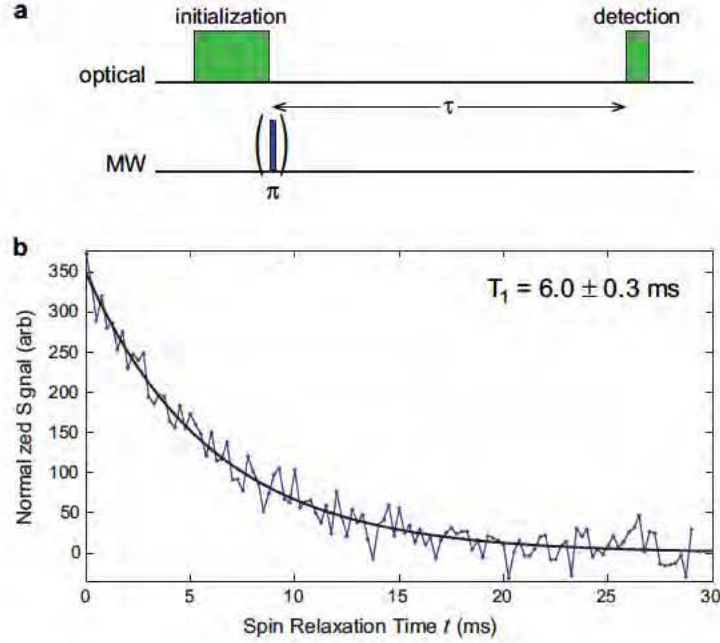
Figure 1.10: T_1 measurement of an NV ensemble. (a) Pulse sequence for measuring T_1. (b) NV spin-relaxation curve.

scale as measured using a single π pulse spin echo (i.e., Hahn echo) pulse sequence. In this dissertation, we adopt the latter convention and indicate the coherence time measured from n-pulse dynamical decoupling sequences as $T_2^{(n)}$.

1.6.3 T_1 spin relaxation time

NV spins also experience relaxation due to spin-flips caused by phononic interactions with the crystal lattice. As a result, the polarization of the NV spin population eventually decays back to the thermally mixed state that exists before optical pumping, with a characteristic time scale T_1. For NV centers in bulk diamond at room temperature, T_1 is typically ~ 6 ms; however, since spin-lattice relaxation is a phononic process, T_1 is quite sensitive to temperature, as discussed in Chapter 6.

The pulse sequence for measuring T_1 in NV spins is shown in Figure 1.10; after an initial optical excitation pulse to polarize the NV spin into the $|0\rangle$ ground state, either a MW π pulse is applied such that the NV spin is transferred to the, e.g., $|+1\rangle$ state (m_1) or no MW pulse is applied and the NV spin is left in the $|0\rangle$ state (m_2). After a time t, an optical detection pulse is applied and the resulting NV fluorescence is collected. The subtraction of the two signals ($s = m_2 - m_1$) rejects common-mode noise and gives the polarization of the NV spin population remaining after time t.

Varying t yields a spin-relaxation curve, from which the characteristic decay time T_1 can be extracted.

Chapter 2

NV Magnetometry

2.1 Introduction

One of the most promising applications for NV centers is as magnetic sensors, both of internal magnetic fields, such as those caused by other spin impurities within the diamond, as well as of magnetic fields produced by external sources, such as biological cells, electronic circuits, advanced materials (e.g., graphene), etc. In the first case, better understanding of the interactions between different spin species (e.g., electron spins associated with substitutional nitrogen and nuclear spins associated with ^{13}C, ^{14}N, and ^{15}N) in the diamond environment may inform engineering decisions for optimizing the NV center for quantum information processing applications and furthermore may be relevant to other solid-state spin systems (e.g., quantum dots, phosphorus donors in silicon, etc.). In the latter case, the ability to image magnetic field patterns with high magnetic sensitivity and spatial resolution could prove a useful characterization tool in a number of fields. In particular, an NV magnetic sensor could be applied to study biomagnetic systems (e.g., neurons, cardiac cells, and magnetic organs used for navigation) [54], geomagnetism, microelectronic circuits, novel materials (e.g, graphene), and nuclear magnetic resonance from organic material at the diamond surface [55, 56].

As mentioned in the previous chapter, the NV center possesses a number of useful properties which make it well-suited for magnetic sensing. First of all, since NV centers are stable point defects embedded in diamond substrates, they can theoretically be localized on a sub-nanometer length scale; as a result, a single-NV magnetic sensor can likewise achieve sub-nanometer scale spatial resolution. It is important to note, however, that the stand-off distance between the NV center and the magnetic field source limits the size of the magnetic features that can be resolved   that is, as the NV center is moved farther from the source, the magnetic features become blurred.

As a result, the spatial resolution of a single-NV magnetic sensor is more practically limited to a few nanometers. Secondly, NV spins can exhibit long coherence times at room temperature and can subsequently perform sensitive magnetometry under ambient conditions. Alternative magnetic sensing technologies with comparable spatial resolution (e.g., superconducting quantum interference devices and magnetic resonance force microscopes) are limited to operation under cryogenic temperatures. In addition to the ability to operate under ambient conditions, diamonds (and to a lesser extent, NV centers) are stable over a wide range of temperatures and pressures, allowing for the possibility of magnetic field measurements under extreme conditions of temperature, pressure, radiation, etc.

An NV-diamond magnetometer may also be implemented using a wide variety of geometries and magnetic field sensing modalities. For example, some possible geometries include incorporating an NV center at the tip of a scanning probe, simultaneously imaging an NV ensemble in a thin layer on a bulk diamond chip over a wide field of view using a charge-coupled device (CCD) array or similar technology, and raster scanning a diffraction-limited optical spot using a confocal microscope. An overview of several popular geometries, including their advantages and disadvantages, is given in Chapter 8. This chapter will cover three major magnetic field sensing schemes for measuring both DC and AC magnetic fields, including discussions of the sensitivity limits of each scheme.

2.2 DC magnetometry: ESR

2.2.1 Description

The simplest method of measuring a magnetic field with NV centers is to take an ESR spectrum and extract the magnetic field information from the NV resonance frequencies. As described previously, in the presence of a magnetic field, the $|\pm 1\rangle$ spin states and subsequently the $|0\rangle \leftrightarrow |\pm 1\rangle$ transition frequencies of an NV center experience Zeeman splitting proportional to the projection of the magnetic field along the NV symmetry axis. A known static field [B_0 in Figure 2.1(a)] can be applied along an arbitrary direction to spectrally distinguish the four possible NV orientation classes from each other in a continuous-wave (CW) ESR spectrum [modeled by the blue curve in Figure 2.1(b)]. Any additional unknown static field δB results in a net static field B_{net} with ESR spectrum resonances that are shifted from those of the known B_0 spectrum [modeled by the red curve in Figure 2.1(b)]. By extracting the resonance shifts which correspond to at least three of the four possible NV orientation classes, one can reconstruct the vector components of the unknown magnetic field. In cases where the fluorescence of NV centers occupying at least three
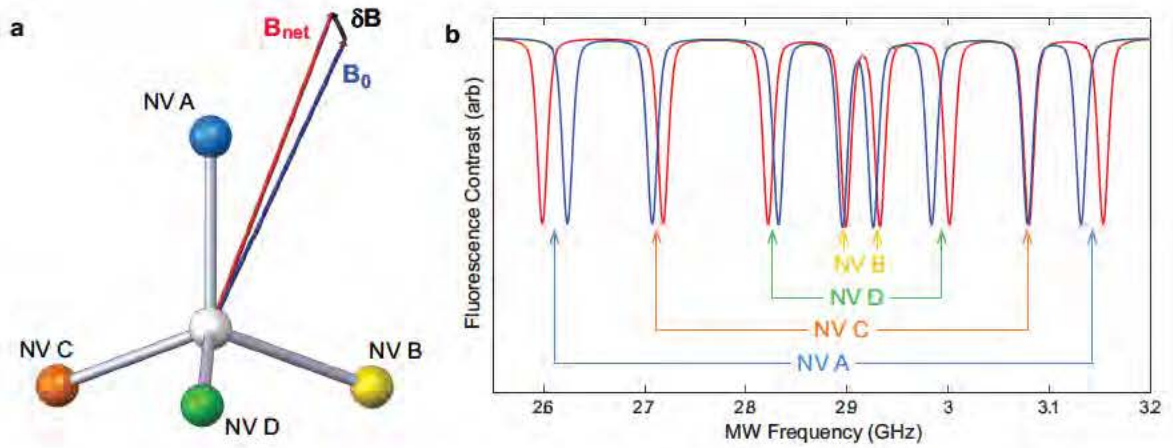
Figure 2.1: Example of an NV ESR based DC magnetic field measurement. (a) Diagram showing the known static field $\mathbf{B_0}$, the measured net magnetic field $\mathbf{B_{net}}$, and the extracted unknown static field δB in relation to the four NV symmetry axes. (b) Modeled ESR spectra of an NV ensemble in the presence of the known magnetic field $\mathbf{B_0}$ (blue) and the net magnetic field $\mathbf{B_{net}}$ (red). By measuring the resonance shifts between these two spectra, the unknown magnetic field δB can be extracted.

of the four possible NV orientation classes can be collected at once (e.g., in a bulk measurement or when there are multiple NV centers per confocal volume, scanning tip, or wide-field magnetic field imager pixel), the vector information of the unknown magnetic field can be extracted from a single ESR spectrum.

In addition to the CW scheme described in Chapter 1, ESR spectroscopy may also be performed using pulses. In a pulsed-ESR measurement, a strong laser excitation pulse first initializes the NV into the $|0\rangle$ spin state. Then, a very low power MW pulse may rotate the NV into, e.g., the $|+1\rangle$ spin state if the MW frequency is resonant with the $|0\rangle \leftrightarrow |+1\rangle$ spin transition. Finally a second short laser excitation pulse is applied and the resulting fluorescence intensity detected to determine the NV spin state. By sweeping the MW frequency, a spectrum similar to what is measured with the CW-ESR scheme is extracted; however, since in the pulsed-ESR scheme, the optical excitation and MW radiation are not applied simultaneously and are therefore not competing, the MW power may be lower than in the CW-ESR scheme, thus reducing MW power broadening. Also, the optical power may be stronger than in the CW-ESR scheme, thus increasing the number of photons collected per measurement (given equivalent measurement times for both schemes). As discussed in the next section, these two factors play an important role in the sensitivity achieved by an ESR based magnetic field measurement.

2.2.2 Sensitivity

The sensitivity η_{esr} of an NV ESR based DC magnetic field measurement is given by the following relation (for derivation, see Appendix A.1):

$$\eta_{\mathrm{esr}} = \mathcal{P}_{\mathcal{F}} \frac{\mathrm{h}}{\mathrm{g}\mu_{\mathrm{B}}} \frac{\Delta\nu\sqrt{t_{\mathrm{m}}}}{\alpha\sqrt{\beta}}, \tag{2.1}$$

where $\mathcal{P}_{\mathcal{F}}$ is a numerical factor determined by the profile of the NV resonance: $\mathcal{P}_{\mathcal{F}} = \sqrt{e/8\ln2} \approx 0.70$ for a Gaussian lineshape, $\mathcal{P}_{\mathcal{F}} = 4/3\sqrt{3} \approx 0.77$ for a Lorentzian lineshape [57]. More importantly, the magnetic field sensitivity is dependent on resonance contrast α, number of photons collected per measurement β, resonance linewidth $\Delta\nu$, and measurement duration t_{m}. These parameters are not independent of each other: the resonance contrast α may be increased by increasing the power of the microwave excitation at the expense of increasing the linewidth $\Delta\nu$ due to power broadening. Likewise, the linewidth $\Delta\nu$ may be decreased (down to a limit defined by the NV spin dephasing time T_2^*) by lowering the laser excitation power to reduce power broadening; however, doing so decreases the number of photons collected per measurement β. Optimizing these parameters to achieve the best DC magnetic field sensitivity using the ESR method yields [57]:

$$\eta_{\mathrm{esr}} \sim \mathcal{P}_{\mathcal{F}} \frac{2\hbar}{\mathrm{g}\mu_{\mathrm{B}}} \frac{1}{\alpha\sqrt{\beta\mathrm{T}_2^*}} \tag{2.2}$$

Note that the optimum magnetic sensitivity given by Equation 2.2 for NV ESR based DC magnetometry can only be achieved using pulsed-ESR techniques; CW-ESR suffers from a trade-off between power-broadening at higher optical powers and fewer photons collected per measurement at lower optical powers [57].

2.2.3 Initial demonstrations

A number of demonstrations of this ESR DC magnetometry scheme have been published to date; however due to the NV center's particular suitability for measuring magnetic fields with high sensitivity and spatial resolution, this section focuses on three initial experimental implementations which also enabled magnetic field imaging.

In the first demonstration, Maertz et al. [58] imaged magnetic field vectors resulting from micron-scale permalloy ($Ni_{0.8}Fe_{0.2}$) structures patterned onto the surface of a type Ib HPHT diamond. The magnetic field pattern at the surface of the diamond was scanned using a confocal microscope geometry, and the NV concentration was sufficiently high that a confocal volume contained all four possible NV orientation classes. Magnetic field images as large as $40\ \mu\mathrm{m} \times 40\ \mu\mathrm{m}$ were shown, with ~ 300

nm spatial resolution and $\sim 20\,\mu$T DC magnetic field resolution (given ~ 10 minutes of averaging per pixel).

Steinert et al. [59] published a paper at almost the same time demonstrating the same ESR based DC magnetic field sensing scheme in a wide-field microscope geometry in which the NV fluorescence is collected from a large field of view simultaneously and imaged onto a CCD camera. Gold microwires were fabricated on the surface of a diamond which had been implanted with nitrogen ions to form a shallow layer (mean depth $\sim 6.7 \pm 2.8$ nm) of NV centers in an otherwise high-purity substrate. The DC magnetic field created by running current through the microwires was measured by imaging the NV fluorescence across a scan of MW excitation frequencies to reconstruct an ESR spectrum for every pixel. In this way, a $\sim 60\,\mu$m $\times$ $60\,\mu$m field of view ESR scan could be acquired in 75 seconds with diffraction-limited spatial resolution ~ 250 nm and magnetic field resolution $\sim 15\,\mu$T. Using Equation 2.1 and experimental parameters presented in the paper ($\alpha \approx 3\%$, $\frac{\beta}{t_\mathrm{m}} \approx 91000$ photons per second, $\Delta\nu \approx 10.5$ MHz, and a Lorentzian lineshape), the expected optimum sensitivity for this demonstration is $\eta_\mathrm{esr} \approx 32\,\mu$T$/\sqrt{\mathrm{Hz}}$.

The spatial resolutions of both the scanning confocal and the wide-field microscope geometries are optical diffraction limited. This limit can be surpassed with a scanning-tip geometry, possible implementations for which include nanodiamonds containing single NV centers affixed to AFM tips and AFM tips fabricated out of high-purity diamond containing single NV centers in the tip. Schoenfeld and Harneit [60] demonstrated a first step toward the former of these possible implementations using a slight modification to the ESR based DC magnetic field sensing scheme. They applied a field-frequency lock in order to measure in real-time the ESR transition frequencies of single NV centers in nanodiamonds with a magnetic field sensitivity of $6\,\mu$T$/\sqrt{\mathrm{Hz}}$. By scanning the position of several nanodiamonds with respect to a steel wire creating a test static magnetic field, $30\,\mu$m $\times$ $30\,\mu$m images of the magnetic field vectors were acquired with magnetic resolution $\sim 30\,\mu$T in 10 minutes.

The ESR NV magnetometry demonstrations we have discussed thus far used a CW measurement scheme; however as mentioned in the previous section, better magnetic field sensitivities $\lesssim 1\,\mu$T$/\sqrt{\mathrm{Hz}}$ are achievable using pulsed-ESR techniques. Dréau et al. [57] demonstrated a pulsed-ESR optimum magnetic field sensitivity $\approx 0.3\,\mu$T$/\sqrt{\mathrm{Hz}}$ using a single NV center in a high-purity bulk diamond, roughly an order of magnitude improvement over the $\approx 2\,\mu$T$/\sqrt{\mathrm{Hz}}$ achieved using the CW-ESR technique.

The ESR spectroscopy based DC magnetometry scheme is a quick, simple, and robust way to extract magnetic field vector information; however the technique is limited by the linewidth of the ESR resonance, which is fundamentally set by the inverse of the NV dephasing time T_2^*. This dephasing time is typically on the order of $\sim 1\,\mu$s in high-purity samples, though T_2^* times on the order of $\sim 100\,\mu$s have been

observed in high-purity isotopically engineered samples [1].

2.3 DC magnetometry: Ramsey sequence

2.3.1 Description

DC magnetic fields can also be measured using a Ramsey pulse sequence. In this measurement scheme, a known static external magnetic field is typically applied to split the $|\pm 1\rangle$ states for technical simplicity. As described previously, after an optical excitation pulse polarizes the NV spin into the $|0\rangle$ state, a MW $\pi/2$ pulse prepares the spin into, e.g., a superposition of the $|0\rangle$ and $|+1\rangle$ states. The NV spin freely precesses for a time τ, during which it accumulates a phase $\phi = 2\pi\gamma B\tau$, where B is the magnitude of the unknown static field to be measured and $\gamma = g\mu_{\rm B}/h \approx 2.8$ MHz/G is the NV electronic spin gyromagnetic ratio. After the free precession interval, a second MW $\pi/2$ pulse projects the spin back into the $|0\rangle, |+1\rangle$ manifold, from which the phase accumulation can be extracted.

Actual measurements can be accomplished in two ways. First, the free precession time τ may be swept, and a Fourier transform may be performed on the resulting Ramsey fringes. Any shift $\delta\nu$ in the resulting resonance frequencies from what is expected given the known applied static field can be attributed to the unknown static field; therefore B can be extracted using the standard Larmor equation $B = \delta\nu/\gamma$.

Alternatively, consider a fixed free precession time τ (Figure 2.2); let's define a as the number of photons collected in one measurement in the absence of the unknown static field, b as the number of photons collected in one measurement when there is a phase accumulation of $\phi = \pi$ during the free precession time τ, and an average number of photons collected in one measurement $\beta = (a+b)/2$. In the presence of the unknown static field B, the number of photons collected in a measurement $\mathcal{S}$ oscillates between a and b as a function of the phase accumulation during the free precession time [as shown in Figure 2.2(b)]:

$$\mathcal{S} = \frac{(a+b)}{2} + \frac{(a-b)}{2}\cos{(\phi)} = \frac{(a+b)}{2} + \frac{(a-b)}{2}\cos{(\gamma B\tau)} \qquad (2.3)$$

Using Equation 2.3, the magnitude B of the unknown static field can be extracted from the number of photons measured $\mathcal{S}$. The main caveat when using this technique is of course that magnetic fields with magnitudes $B + \frac{2\pi m}{\gamma\tau}$, where m is an integer, all yield the same number of photons $\mathcal{S}$. However, these types of measurements are still quite useful for measuring relative magnetic fields or field fluctuations.
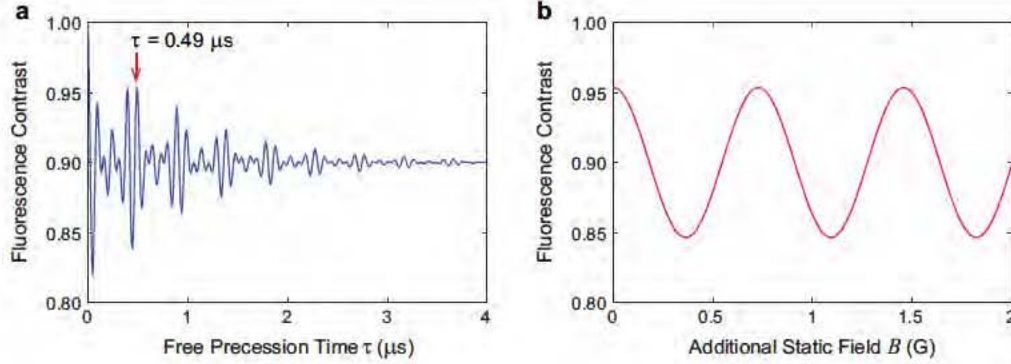
Figure 2.2: Example of a Ramsey based DC magnetic field measurement. (a) Modeled Ramsey FID curve in the presence of known magnetic field B_0. (b) Example magnetometry curve showing the sinusoidal response of the NV fluorescence signal to an additional static field B. The Ramsey pulse sequence free precession time is fixed at $\tau = 0.49\,\mu$s, indicated by the red arrow in (a).

2.3.2 Sensitivity

The sensitivity η_{ramsey} of an NV magnetometer which uses the Ramsey pulse sequence to measure DC magnetic fields is given by (see Appendix A.2 for derivation):

$$\eta_{\text{ramsey}} \approx \frac{\hbar}{g\mu_B} \frac{1}{\sqrt{\tau}} \frac{1}{\alpha\sqrt{\beta}} \qquad (2.4)$$

As in the DC magnetometry scheme utilizing ESR spectroscopy, the magnetic field sensitivity is dependent on resonance contrast α, number of photons collected per measurement β, and measurement duration τ. Also as before, these parameters are not independent. The measurement contrast decays as a result of NV spin dephasing, with characteristic time scale T_2^*. Thus, increasing the measurement duration τ degrades the contrast α. The optimum magnetic field sensitivity is achieved when $\tau \sim T_2^*$:

$$\eta_{\text{ramsey}} \sim \frac{\hbar}{g\mu_B} \frac{1}{\alpha\sqrt{\beta T_2^*}} \qquad (2.5)$$

2.3.3 Initial demonstrations

This Ramsey DC magnetometry scheme has been demonstrated qualitatively by Balasubramanian et al. [1], and its magnetic field sensitivity has been theoretically analyzed in depth [52, 61, 57]; however, a thorough experimental demonstration of NV magnetometry using the Ramsey pulse sequence has yet to be published. As with the ESR spectroscopy based magnetometry technique, however, the magnetic

field sensitivity of this technique is fundamentally limited by the dephasing time T_2^*, which in NV centers is typically of the order of several microseconds, though T_2^* may reach several hundred microseconds in ultra-pure samples [62].

2.4 AC magnetometry

2.4.1 Description

Recall that employing a spin echo sequence — that is, inserting an additional MW π pulse in the center of a Ramsey sequence — can extend the characteristic time scale of the NV signal decay from T_2^* dephasing to T_2 decoherence. Since the optimum magnetic field sensitivity of the Ramsey based technique is limited by T_2^*, a corresponding improvement in sensitivity may be expected by employing a spin echo pulse sequence for magnetometry. However, in the spin echo sequence, any phase accumulation due to an unknown static magnetic field during the first free precession time will be echoed out by the MW π pulse along with all other static magnetic inhomogeneities. As a result, the spin echo pulse sequence is insensitive to static magnetic fields and not useful for DC magnetometry.

Consider instead an oscillating (AC) magnetic field. If the spin echo pulse sequence is applied such that the MW pulses coincide with field nodes [Figure 2.3(a)], the net phase accumulated in each half of the pulse sequence is additive rather than subtractive. As a result, the spin echo pulse sequence is useful for measuring AC magnetic fields, where the choice of the full pulse sequence duration determines the AC frequency to which the magnetometry measurement is sensitive.

Actual measurements of AC magnetic fields using this technique are accomplished in a manner similar to the latter technique described in the Ramsey DC magnetometry section. Consider an echo pulse sequence of duration τ, which is sensitive to AC magnetic fields of frequency $f_{\mathrm{ac}} = 1/\tau$. In the absence of an AC magnetic field, the NV spins do not accumulate net phase during the free precession intervals and are thus projected back into the $|0\rangle$ state at the end of the pulse sequence: i.e., there is no fluorescence signal change. In the presence of an AC magnetic field of amplitude B and frequency f_{ac}, with the pulse sequence optimally timed such that the MW pulses coincide with nodes in the field, the NV spins accumulate net phase $\phi = 4\gamma B\tau$ during the free precession intervals (see Appendix A.3 for derivation). This phase accumulation, when projected into the measurement basis at the end of the pulse sequence, results in a fluorescence signal change.

As in the latter Ramsey DC magnetometry technique, the number of photons collected in a measurement $\mathcal{S}$ oscillates as a function of the phase accumulation ϕ during
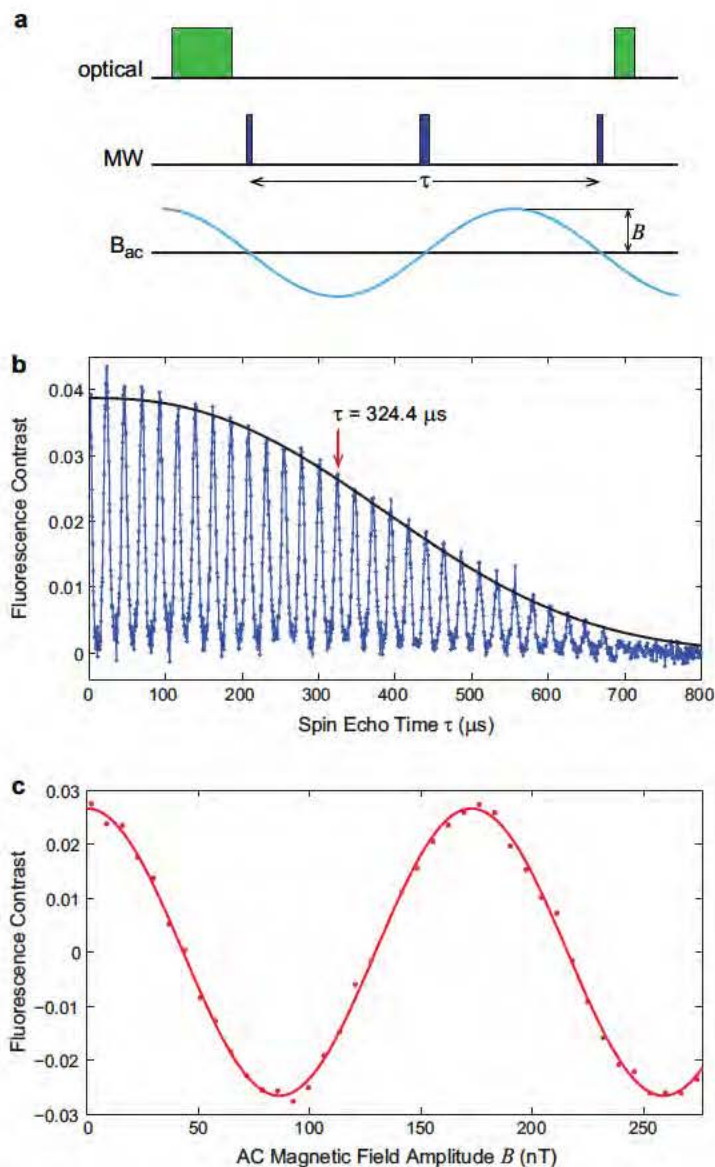
Figure 2.3: Example of a spin echo based AC magnetic field measurement. (a) Spin echo pulse sequence showing the optimum timing of the MW pulses with respect to the AC magnetic field to be measured. (b) Measured spin echo decoherence curve of an NV ensemble. The collapses and revivals are characteristic of ^{13}C Larmor precession (discussed in Chapter 3). (c) Measured magnetometry curve showing the sinusoidal response of the NV fluorescence signal to AC magnetic field amplitude B. The spin echo time corresponding to the magnetic field frequency $f_{ac} = 3.0825$ kHz is indicated by the red arrow in (b).

the free precession time τ between a (corresponding to $\phi = 0$) and b (corresponding to $\phi = \pi$) [as shown in Figure 2.3(c)]:

$$\mathcal{S} = \frac{(a+b)}{2} + \frac{(a-b)}{2}\cos(\phi) = \frac{(a+b)}{2} + \frac{(a-b)}{2}\cos(4\gamma B\tau) \qquad (2.6)$$

Using Equation 2.6, the amplitude B of the AC magnetic field can be extracted from the number of photons measured $\mathcal{S}$. Recall, a caveat when using this technique is that magnetic fields with amplitudes $B + \frac{\pi m}{2\gamma\tau}$, where m is an integer, all yield the same number of photons $\mathcal{S}$. However, these types of measurements are still quite useful for measuring relative magnetic fields or field fluctuations. Additionally, in natural carbon isotopic abundance samples, which exhibit collapses and revivals in the NV spin coherence due to ^{13}C Larmor precession, the frequency of the AC magnetic field to be measured must coincide with a revival [see Figure 2.3(b)]:

$$f_{\text{ac}} = \frac{1}{\tau} = \frac{\gamma_{^{13}\text{C}} B_0}{2\ell}, \qquad (2.7)$$

where the ^{13}C nuclear gyromagnetic ratio $\gamma_{^{13}\text{C}} \approx 1.071$ kHz/G, B_0 is the magnitude of the static magnetic field applied to split the NV ground state spin transitions, and ℓ is an integer. This condition is easily met by adjusting the magnitude B_0 of the applied static field as necessary. Also note that in sub-optimal situations of randomly fluctuating magnetic fields or where the MW pulses do not coincide with magnetic field nodes, the spin echo technique is still able to sense AC magnetic fields with reduced sensitivity, as long as the MW pulses do not coincide with anti-nodes [63, 64].

2.4.2 Sensitivity

The sensitivity η_{se} of an NV magnetometer employing a spin echo pulse sequence to measure an AC magnetic field along the NV axis, where the MW pulses are synchronized with nodes in the magnetic field for optimal sensitivity, is given by (see Appendix A.3 for derivation):

$$\eta_{\text{se}} \approx \frac{\pi\hbar}{2\text{g}\mu_{\text{B}}} \frac{1}{\sqrt{\tau}} \frac{1}{\alpha\sqrt{\beta}} \qquad (2.8)$$

Here the time of a measurement is approximated by the full free precession time τ.

Similar to the other NV magnetometry schemes discussed thus far, the magnetic field sensitivity is dependent on resonance contrast α, number of photons collected per measurement β, and measurement duration τ. Again, these parameters are not independent; the measurement contrast decays as a result of NV spin decoherence, with characteristic time scale T_2. Thus, increasing the measurement duration τ degrades

the contrast α. The optimum magnetic field sensitivity for an spin echo measurement is achieved when $\tau \sim T_2$ [52]:

$$\eta_{\text{se}} \sim \frac{\pi\hbar}{2g\mu_{\text{B}}} \frac{1}{\alpha\sqrt{\beta T_2}} \tag{2.9}$$

As expected, the magnetic field sensitivity of a spin echo based AC measurement is limited by T_2 rather than T_2^* as in the Ramsey based DC measurement. Typical spin echo coherence times in high-purity samples are on the order of $\sim 500\,\mu$s, though T_2 times on the order of ~ 2 ms have been observed in high-purity isotopically engineered samples [1].

2.4.3 Initial demonstration

The first experimental demonstration of the spin echo based NV magnetometry scheme was performed by Maze et al. [65]: using a confocal microscope to probe a single NV center in a high-purity bulk diamond sample, they measured AC magnetic fields of kilohertz frequencies with sensitivity $30\,\text{nT}/\sqrt{\text{Hz}}$. They were also able to achieve an AC magnetic field sensitivity of $0.5\,\mu\text{T}/\sqrt{\text{Hz}}$ using a single NV center in a diamond nanocrystal of diameter ~ 30 nm.

Since this first demonstration, NV magnetometers for measuring AC fields have been implemented in a number of other geometries, and much work has been done to improve the magnetic field sensitivity of this technique by, e.g., improving measurement contrast [66], improving photon collection [67, 68, 69, 70], and extending coherence times either by using specially engineered materials [1] or by employing more complicated pulse sequences [64, 71, 3]. In particular, the first demonstration of AC magnetic field imaging using NV ensembles as well as several techniques for improving the sensitivity of AC magnetic field measurements using NV centers will be covered in detail in Chapters 4, 6, and 5 of this dissertation.

Though the spin echo based AC magnetometry scheme is greater than an order of magnitude more sensitive than the T_2^*-limited DC magnetometry schemes, there are some limitations to the technique. First, due to the sinusoidal response of the NV fluorescence signal to AC magnetic field amplitude, the absolute magnetic field value cannot be extracted without a priori knowledge of the system. For many applications, however, relative field measurements are sufficient. It is also important to note that the bandwidth of AC frequencies that can be measured is limited by NV spin decoherence to $\gtrsim 1/T_2$.

2.5   Summary

The magnetic field sensitivities of the three NV magnetic sensing schemes discussed in this chapter can be simplified to the following relation:

$$\eta \propto \frac{1}{\alpha\sqrt{\beta T}} \tag{2.10}$$

where the measurement time T is limited to the dephasing time T_2^* for DC field measurements and the coherence time T_2 for AC field measurements. Equation 2.10 illustrates how the sensitivity of an NV based magnetic field sensor can be improved by increasing the measurement contrast α, the number of photons collected per measurement β, and the measurement time T (i.e., the coherence time).

The remainder of this dissertation will present and discuss a number of efforts to demonstrate and improve AC magnetometry using NV centers in diamond, with particular emphasis on magnetic field imaging with NV ensembles in a wide-field CCD based geometry; however many of the techniques for improving magnetic sensitivity are applicable to single centers and alternative geometries as well. Chapter 3 discusses the dependence of the spin echo T_2 on the misalignment angle between the NV symmetry axis and the static field B_0. Chapter 4 presents the first demonstration of a wide-field CCD based NV magnetic field imager. Chapter 5 explores improving sensitivity by improving measurement contrast via preferential NV orientation. Chapter 6 explores improving sensitivity by improving the coherence time with multipulse sequences. These multipulse sequences can also be employed to study different regimes of spin environments, as discussed in Chapter 7. Finally, an overview of the various magnetic sensing geometries and modalities that have been proposed for applying NV magnetometry to various applications will be discussed in Chapter 8.

Chapter 3

NV Spin Coherence Dependence on Magnetic Field Misalignment

3.1 Introduction

As discussed in the previous chapter, there are three major factors which affect NV magnetic field sensitivity: the measurement contrast, the number of photons collected per measurement, and the measurement time (limited by spin decoherence). One approach for improving the number of photons collected per measurement is to simply probe more NV centers by performing ensemble measurements. Ideally in this case, the magnetic field sensitivity increases as the square root of the number of NV centers in the ensemble. However, practically, ensemble measurements are typically performed on one NV orientation class with the other three classes contributing background fluorescence, thereby degrading the measurement contrast as compared to that achieved by probing a single NV center. This issue is addressed in more detail in Chapter 5. In addition, increasing the density of NV centers, is typically accompanied by an increase in the density of residual nitrogen paramagnetic impurities, which can become the dominant source of NV spin decoherence, reducing T_2 below the limit set by ^{13}C nuclear spins alone [72, 73, 48]. Furthermore, the random distribution of ^{13}C nuclear spins near each NV center results in a large variation in individual NV spin coherence times, which also can affect ensemble coherence. It is worthwhile to note that large spin ensembles with good coherence times are also important in implementing collective quantum memories [74, 75, 76]. Therefore, a detailed understanding of the decoherence mechanisms affecting NV centers   both single centers and ensembles   accompanied by the development of control techniques to mitigate decoherence is of great importance for both precision magnetometry and quantum information applications.

Recall that the spin decoherence of an NV center is governed by interactions with the surrounding bath of nuclear and paramagnetic spins. In high-purity diamond, decoherence is dominated by ^{13}C nuclear spins ($I = 1/2$) [77], which are dispersed through the crystal with a natural abundance of 1.1%. NV spin coherence times $T_2 > 600\,\mu$s have been observed at room temperature for individual NV centers in this type of sample [65, 51]. T_2 can be further increased by isotopically engineering the diamond [51]; for example, single NV $T_2 > 1.8$ ms has been observed at room temperature in ultrapure diamond with 99.7% ^{12}C [1]. At the time of this work, only limited studies of spin decoherence in ensembles of NV centers had been previously reported: at room temperature, an NV ensemble $T_2 \approx 58\,\mu$s was measured in CVD diamond [78], whereas at low temperature (< 2 K) and high magnetic field (> 8 T), an NV ensemble $T_2 \approx 250\,\mu$s was measured in type 1b HPHT diamond, which degraded to $T_2 < 10\,\mu$s for temperatures > 20 K [79].

In this chapter, we present an experimental and theoretical study of the coherence properties of NV spin ensembles in room temperature diamond samples of different paramagnetic nitrogen (and consequently NV) concentrations. For Sample A, containing very low nitrogen density and a natural abundance of ^{13}C, we find NV ensemble T_2 in excess of 600 μs, comparable to the best results for single NV center measurements in natural isotopic abundance diamond and an order of magnitude greater than previous room temperature ensemble measurements. For Sample B, containing a slightly higher nitrogen density and a natural abundance of ^{13}C, we find NV ensemble $T_2 \approx 300\,\mu$s. Furthermore, for both samples we find a sharp decrease in the NV ensemble T_2 with misalignment of the static magnetic field relative to the symmetry axis of the NV orientation class being measured. This behavior is consistent with our theoretical modeling of an ensemble of NV spins interacting with a ^{13}C spin bath [77].

3.2 NV–^{13}C hyperfine interactions

In high-purity diamond, the decoherence of each individual NV spin is dominated by hyperfine interactions with nearby ^{13}C nuclear spins. The contact term of this interaction decreases exponentially with separation; after a few lattice sites it is not larger than a few megahertz [80]. Meanwhile, the dipolar term of this interaction decreases as r^{-3} and is responsible for the collapses and revivals observed in NV spin echo measurements [41]. When the externally applied static magnetic field is aligned with the NV symmetry axis, the dipolar field contributions of all ^{13}C nuclei cancel after each 2π Larmor precession period of the ^{13}C nuclear spins, as can be measured by the spin echo sequence [41, 81, 49]. Over longer time scales ($> 600\,\mu$s for natural abundance ^{13}C), weak dipole-dipole interactions between ^{13}C nuclei and between ^{13}C

and paramagnetic impurities induce fluctuations ("flip-flops") in the NV ^{13}C hyperfine interaction, leading to NV spin decoherence. The predicted form of this decoherence in the spin echo signal of an individual NV is $\exp\left[-\beta\tau^p\right]$, where the power p in the exponent is between 3 and 4 and the constant β depends on details of the relative location of nearby ^{13}C nuclei [77]. However, when the magnetic field makes a small angle θ with the NV axis, the Larmor precession frequency Ω_i of individual ^{13}C nuclei is modified by the hyperfine interaction with the NV center, dependent on θ and the relative NV ^{13}C position $\boldsymbol{r_i}$:

$$\Omega_i = \Omega_0 + \delta\Omega\left(\theta, \boldsymbol{r_i}\right) \tag{3.1}$$

As a consequence, ^{13}C nuclei particularly those proximal to the NV center do not all precess with the same frequency and thus their modulations of the NV spin coherence do not rephase at the same time in the spin echo sequence, inducing NV spin decoherence of the form $\exp\left[-\alpha\left(\theta\right)b\tau^2\right]$ [77]. Here $\alpha\left(\theta\right)$ describes the misalignment angle dependence of the imperfect spin echo rephasing, and b is proportional to the square of the hyperfine interaction between the NV electronic spin and the nearest ^{13}C nuclear spin. For small θ, $\alpha\left(\theta\right) \simeq \theta^2$.

In diamond samples where the N and NV concentrations are low enough that NV centers do not interact significantly with each other or with nitrogen paramagnetic impurities, the ensemble spin echo signal can be considered as the average of many independent signals from individual NV centers. In this case, the ensemble spin echo signal envelope, $E(\tau)$, can be significantly different from measurements of single NV centers [82, 83] because an ensemble contains a broad distribution of spin coherence lifetimes due to variations in the positions of ^{13}C nuclei with respect to individual NV centers in the ensemble:

$$E(\tau) = \int db \exp\left(-\alpha\left(\theta\right)b\tau^2\right)f\left(b\right). \tag{3.2}$$

Here, $f\left(b\right)$ is the probability distribution for the magnitude of the NV proximal ^{13}C hyperfine-interaction-squared in an ensemble. Depending on details of this distribution, the ensemble spin echo signal envelope may exhibit Gaussian ($p=2$) or even single exponential ($p=1$) decay at large times τ [82, 83].

3.3 Results

We used a custom-built, wide-field fluorescence microscope (see Appendix B.1 for details) to measure the coherence properties of large ensembles of NV centers. A uniform static magnetic field was applied using a permanent magnet trimmed by a three-axis set of Helmholtz coils. We extracted the magnitude B_0 of the applied

magnetic field from the timing of the revivals in each spin echo coherence curve. As stated previously, these revivals occur when there is an integer number of ^{13}C Larmor precession periods during each half of the spin echo sequence, where the ^{13}C Larmor frequency is given by $\omega_{\rm L} = \gamma_{^{13}{\rm C}} B_0$ ($\gamma_{^{13}{\rm C}} \approx 1.071$ kHz/G). The misalignment angle θ of the applied magnetic field relative to the symmetry axis of a given NV orientation class was calculated using the extracted field magnitude B_0 and the projection of the field along the NV symmetry axis determined from the measured Zeeman splitting of the NV ground-state electronic spin resonances, which is typically different for each of the four possible NV orientation classes.

We employed two CVD diamond samples in our NV ensemble measurements. Sample A is a diamond (3 mm × 3 mm × 0.2 mm) with NV density $\sim 5 \times 10^{12}$ cm^{-3} (~ 0.03 ppb) uniformly across the sample, as determined by fluorescence measurements normalized to single NV fluorescence made on each sample using a custom-built confocal microscope (see Appendix B.2 for details). Sample B consists of a pure diamond substrate (3 mm × 3 mm × 0.2 mm) with < 1 ppm of ambient nitrogen impurity and $< 10^{12}$ cm^{-3} ($< .006$ ppb) NV density, which was overgrown with a N-doped layer $\sim 3\,\mu$m thick. The density of NV centers in the thin layer region is $\sim 1 \times 10^{14}$ cm^{-3} (~ 0.6 ppb). The density of nitrogen impurities in each of the samples is $\gtrsim 200$ times larger than the NV density, estimated from typical N-to-NV conversion efficiency in CVD grown diamonds. The NV ensemble spin coherence times were measured by detecting from regions with cross-sectional area $\approx 30\,\mu$m^2 (corresponding to $\sim 10^3$ NV spins) in each sample. Over macroscopic distances (~ 1 mm), each diamond sample was found to have uniform spin coherence properties.

With the magnetic field well aligned with the NV spin axis, we measured in each sample NV ensemble coherence times comparable to previous measurements for single centers: $T_2 > 600\,\mu$s for Sample A and $T_2 \approx 300\,\mu$s for Sample B. Our measurements also confirm the predicted [77] sharp decrease of NV T_2 with small misalignment of the magnetic field from the NV axis. Example spin echo measurements at three representative misalignment angles θ for each sample are shown in Figure 3.1.

Figure 3.2 summarizes the results of a larger set of systematic measurements of ensemble NV T_2 as a function of θ. In each of these measurements, the spin echo signal envelope was fit to $\exp\left[-\left(\tau/T_2\right)^p\right]$ to determine the coherence lifetime T_2 [Figure 3.2(a)] and decay exponent p [Figure 3.2(b)]. Good agreement is found between our experimentally determined values for T_2 as a function of θ and theoretical predictions [see solid curve in Figure 3.2(a)], which include the decoherence contributions from proximal ^{13}C nuclear spins via the form $\exp\left[-\alpha\left(\theta\right) b\tau^2\right]$ [77].Decoherence due to ^{13}C "flip-flops" was included phenomenologically by multiplying the simulated NV echo signal by $\exp\left[-\left(\tau/T_2\left(\theta = 0\right)\right)^4\right]$. The low values for the decay exponent p in ensemble experiments is explained by the large dispersion of the dominant NV ^{13}C dipole-dipole interaction (see Equation 3.2). The distribution of this interaction

Chapter 3: NV Spin Coherence Dependence on Magnetic Field Misalignment
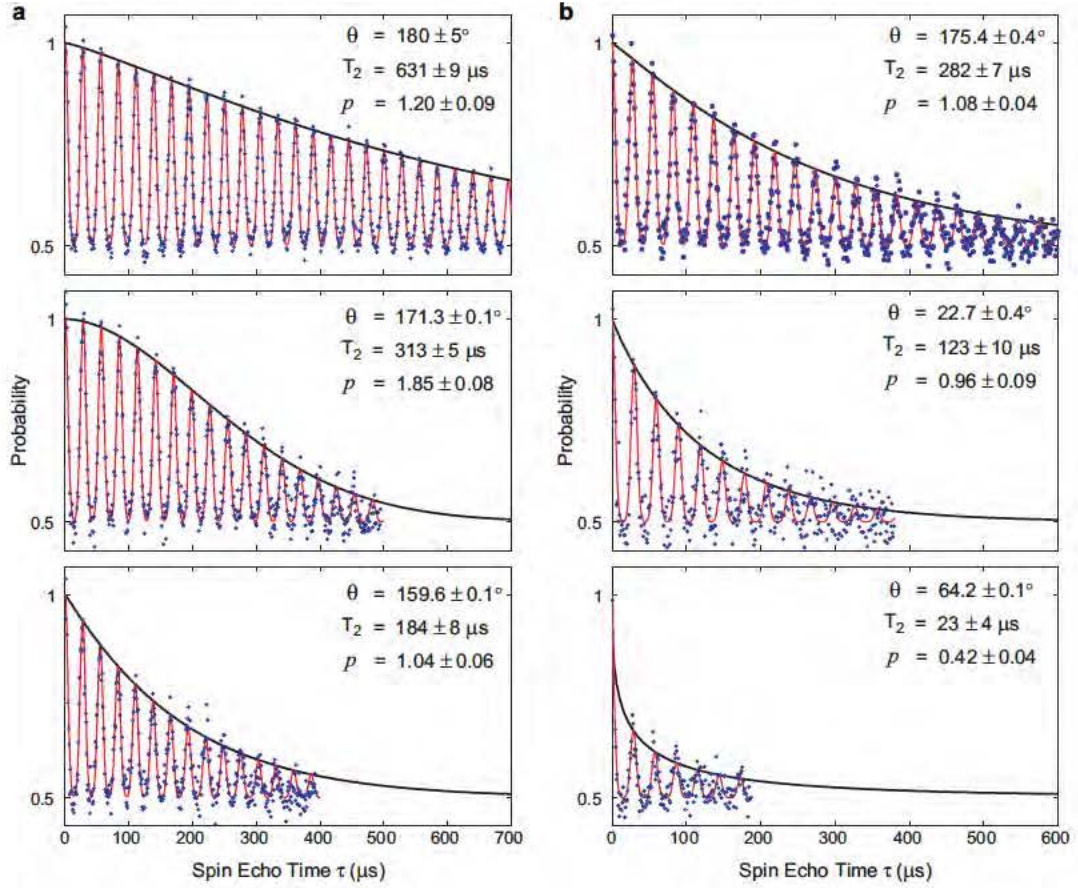
Figure 3.1: Example spin echo measurements of NV ensemble spin decoherence. (a) Sample A with NV density $\sim 5 \times 10^{12}$ cm^{-3} (~ 0.03 ppb) and N density $\gtrsim 1 \times 10^{15}$ cm^{-3} ($\gtrsim 5$ ppb); and (b) Sample B with NV density $\sim 1 \times 10^{14}$ cm^{-3} (~ 0.6 ppb) and N density $\gtrsim 2 \times 10^{16}$ cm^{-3} ($\gtrsim 100$ ppb). Clearly seen in this data is a sharp decrease in the ensemble NV coherence lifetime T_2 as the B_0 field is misaligned from the NV spin axis, and as the paramagnetic impurity level increases. For each data plot, the left vertical axis indicates the measured probability for NVs in the ensemble to be in the $|0\rangle$ state at the end of a spin echo experiment, as a function of the echo time τ; the black line is a fit of $\exp\left[-\left(\tau/T_2\right)^p\right]$ to the overall spin echo signal envelope, where the exponent p is a fit parameter and the long term baseline is taken to be 0.5 (the mixed spin state); and the errors in θ, T_2, and p are given by one-standard-deviation confidence intervals of the fit. The red line is a fit to the observed echo signal modulations, which are collapses and revivals of NV spin coherence induced by precession of the natural abundance ^{13}C nuclear spin bath in applied, hyperfine, and dipolar magnetic fields.

Chapter 3: NV Spin Coherence Dependence on Magnetic Field Misalignment
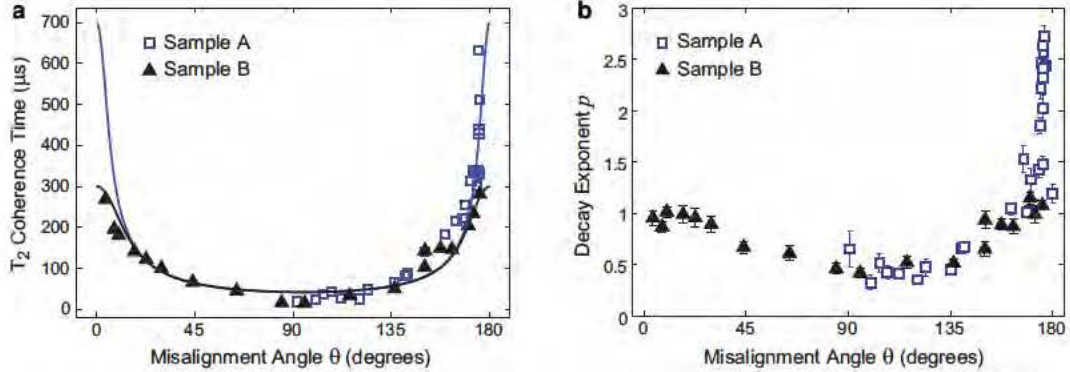
Figure 3.2: Summary of spin echo measurements as a function of misalignment angle θ between the static magnetic field and the NV electronic axis: (a) coherence lifetime T_2 and (b) decay exponent p, determined from fits of the signal envelope to $\exp\left[-\left(\tau/T_2\right)^p\right]$. Sample A (lower NV and nitrogen concentration) was measured for θ ranging from 90 to 180 degrees; Sample B (higher NV and nitrogen concentration) was measured for θ from 0 to 180 degrees. The solid curve in (a) is the prediction of the NV ensemble decoherence model, as described in the main text.

squared, $f(b)$, was determined by calculating the effect of ^{13}C nuclei placed randomly in the diamond lattice at natural isotopic abundance. For the dominant NV ^{13}C dipole-dipole interaction, we find that this distribution scales as $f(b) \sim b^{-3/2}$ for ^{13}C nuclei within about 10 nm of an NV center. Thus, $f(b)$ more closely resembles a Lorentzian than a Gaussian distribution, resulting in spin echo signal envelopes that decay more like a single exponential than a Gaussian at large times (see Figure 3.1). Note that for Sample B, the experimentally determined decay exponent is $p \simeq 1$ even for $\theta \simeq 0$ [Figure 3.2(b)], which likely results from interactions between NV spins and the higher density of paramagnetic nitrogen impurities in this sample.

Spin echo measurements were also performed on a third sample (Sample C) with NV density $\sim 1 \times 10^{14}$ cm^{-2} (~ 0.6 ppb) and N density $\sim 2 \times 10^{17}$ cm^{-2} (~ 1 ppm), which was isotopically engineered to contain 99.99% ^{12}C. In contrast to the two natural isotopic abundance samples, the Sample C spin coherence curves do not exhibit the collapses and revivals induced by the Larmor precession of ^{13}C nuclear spins in the presence of magnetic fields. Furthermore, long NV ensemble $T_2 \sim 250\mu$s was observed even at large misalignment angles between the magnetic field and the NV axis, as illustrated by the comparable NV ensemble spin coherence curves measured at misalignment angles $\theta \approx 0°$ and $\theta \approx 28°$ shown in Figure 3.3. Note that in the absence of ^{13}C revivals, the applied magnetic field orientation and magnitude can also be estimated from the spin transition frequencies of the four NV orientation classes.

Chapter 3: NV Spin Coherence Dependence on Magnetic Field Misalignment
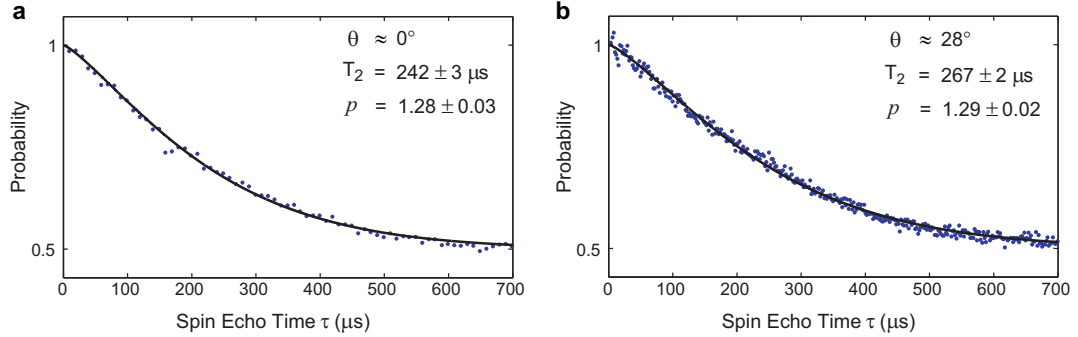
Figure 3.3: Example spin echo measurements of NV ensemble spin decoherence in isotopically engineered Sample C for a magnetic field that is (a) well aligned to the NV axis and (b) misaligned from the NV axis. The solid black line is a fit of $\exp\left[-(\tau/\mathrm{T}_2)^p\right]$ to the spin echo signal, where the exponent p is a fit parameter and the long term baseline is taken to be 0.5 (the mixed spin state).

3.4 Summary

In summary, we demonstrated experimentally that large ensembles of NV centers in high-purity diamond with a natural abundance of ^{13}C can have spin coherence lifetimes at room temperature that are comparable to the best measured for single NV centers ($\mathrm{T}_2 > 600\,\mu$s). We also found a sharp decrease in NV spin coherence time as the applied magnetic field is misaligned from the NV axis in samples with a natural abundance of ^{13}C. This behavior is consistent with the predictions of our model for an ensemble of NV spins coupled via position-dependent hyperfine interactions to a ^{13}C nuclear spin bath, leading to imperfect ^{13}C spin echo revivals and hence, NV decoherence. In contrast, in a sample isotopically engineered with 99.99% ^{12}C, comparable NV ensemble spin coherence times were observed even for large magnetic field misalignment angles. Our results demonstrate the potential of NV ensembles for applications in precision magnetometry, combining long spin coherence times at room temperature with the enhanced photon collection provided by probing many NV centers in the detection volume [52].

Chapter 4

NV Magnetic Field Imaging

4.1   Introduction

In recent years, NV ensembles have been employed to sense DC magnetic fields, demonstrating both vector magnetometry and 2-dimensional magnetic field imaging [58, 59, 84, 60]. However, as discussed in Chapter 2, the sensitivity of such DC magnetometry schemes is limited by typical μs-scale NV T_2^* dephasing times: the best sensitivity experimentally achieved by recent NV ensemble DC magnetometers is $\approx 32\,\mu\mathrm{T}/\sqrt{\mathrm{Hz}}$ [59]. A natural extension of these efforts, then, is to apply the spin echo based AC magnetometry technique to ensembles of NV centers. The resulting combination of longer measurement time (limited by T_2 rather than T_2^*) and higher photon collection (from probing multiple NV centers rather than a single one) provide dual improvements to the magnetic sensitivity. Furthermore, as demonstrated in Chapter 3, NV ensemble coherence times are not significantly degraded from coherence times measured from single NV centers, which has important implications in the ability to maximize the sensitivity of an NV ensemble based AC magnetometer.

In this chapter, we discuss a method for 2D imaging of magnetic fields using an ensemble of NV centers in a thin layer at the surface of a diamond chip. By exciting NV centers confined to a thin surface layer over a large area in bulk diamond and imaging the resulting fluorescence onto a CCD camera, we demonstrate optical detection of 2D AC magnetic field patterns over large fields of view ($> 100\,\mu$m) with sub-micron spatial resolution and magnetic sensitivity $\sim 100\,\mathrm{nT}/\sqrt{\mathrm{Hz}}$ per pixel.

4.2   Experimental setup

To demonstrate the imaging capabilities of NV ensembles in diamond, we custom built a wide-field fluorescence microscope (see Appendix B.1 for details). Such a

wide-field microscope geometry has the key advantages of being relatively simpler to construct and having a shorter intrinsic image acquisition time over a large field of view than a scanning confocal microscope.

Vector magnetometry is accomplished by resonantly coupling the microwaves to one of the four possible NV orientation classes and sequentially measuring the magnetic field projection onto the different NV vectors. However, there is an important caveat to consider when addressing several NV orientation classes: recall from Chapter 3 that in diamond samples with low nitrogen content and a natural abundance of ^{13}C isotopes, NV spin coherence is limited by the ^{13}C bath and is subsequently strongly dependent on small misalignments between the static magnetic field and the NV axis. Thus, taking measurements with different NV orientation classes often practically requires switching between different static magnetic fields, each aligned along a particular NV symmetry axis. It is also important to note that while diamonds with a higher concentration of NV centers in general also contain a higher concentration of nitrogen paramagnetic impurities, which further limit the T_2 coherence time, these samples also produce a larger fluorescence signal and are less sensitive to small misalignments in the static field. In the development of a practical NV ensemble based magnetic field imager, design parameters such as the required magnetic sensitivity, alignment of the static field with the NV axis, and range of AC field frequencies that can be measured will dictate the desired level of impurity concentration.

4.3 Micron-scale magnetic field variations

Resolving magnetic field patterns that vary over sub-micron length scales places additional constraints on the diamond material properties beyond optimizing NV density and coherence time. Small field variations become irresolvable at distances greater than their feature size; therefore, in order to image magnetic fields on a sub-micron length scale, the NV sensors must be confined to a thin layer on the diamond surface and placed within a sub-micron distance of the magnetic field source. This thin-layer geometry can be achieved either by shallow implantation of nitrogen ions [31, 16] or by altering the growth conditions of CVD-synthesized diamonds such that there is a thin N-doped NV-rich layer at one surface of a high-purity substrate.

As discussed in Chapter 1, at the current state of diamond processing technology, shallow implantation offers finer control over the thickness and impurity concentration of the N-doped layer than CVD growth does. Hence, to demonstrate the ability of the NV ensemble magnetic field imager to resolve field variations on the micron scale, we used a high-purity HPHT diamond (Sample D) that had been implanted with N_2^+ molecular ions at 15 keV, creating a shallow NV layer with ~ 4 nm vertical straggle, ~ 11 nm below the surface (as estimated from Monte-Carlo simulations
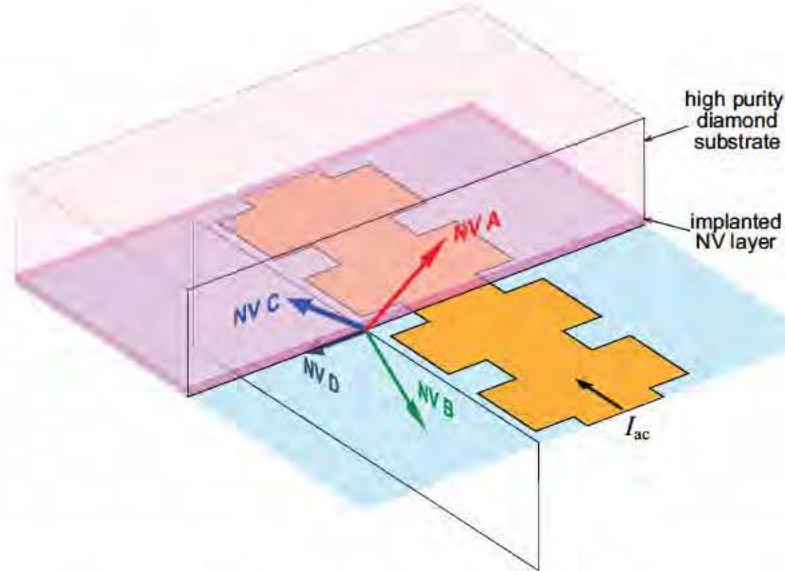
Figure 4.1: Diagram of the notched wire structure with respect to the four NV symmetry axes. The magnetic field measurements were performed on the NV A orientation class.

using SRIM [21]). From the implant dose and the approximate N-to-NV conversion efficiency, we estimate that the 2D NV layer has an NV surface density of $\sim 8 \times 10^{10}\,\mathrm{cm^{-2}}$ and an N density of $\sim 1 \times 10^{12}\,\mathrm{cm^{-2}}$, resulting in a paramagnetic nitrogen-limited $T_2 \sim 30\,\mu s$.

The magnetic field pattern to be imaged was produced by a copper microwire containing segments of alternating width such that the current density through the wire is increased in the constricted sections, resulting in micron-scale magnetic field 'hotspots'. This notched wire pattern was fabricated on a glass coverslip using photolithography and secured flat against the shallow implant NV layer of the diamond sample with a separation distance of $\approx 1\,\mu m$ (Figure 4.1). The proximity of the copper microwire to the NV sensors introduces a complication, however: when the microwave pulses are applied to coherently manipulate the NV spin states, the presence of the metal wire pattern modifies the microwave field profile, resulting in B_1 field inhomogeneity over the plane of NV sensors. This microwave pickup is not expected to be an issue in the proposed bio-applications for the NV ensemble magnetic field imager, where the sources of the magnetic field are, for example, firing neurons rather than metal.

We used a permanent magnet to apply a static field along one of the NV axes perpendicular to the direction of current flow (Figure 4.1) and ran 109.5 kHz AC current through the notched wire pattern. The fluorescence as a function of AC magnetic field amplitude was calibrated on a pixel-by-pixel basis by sweeping the AC
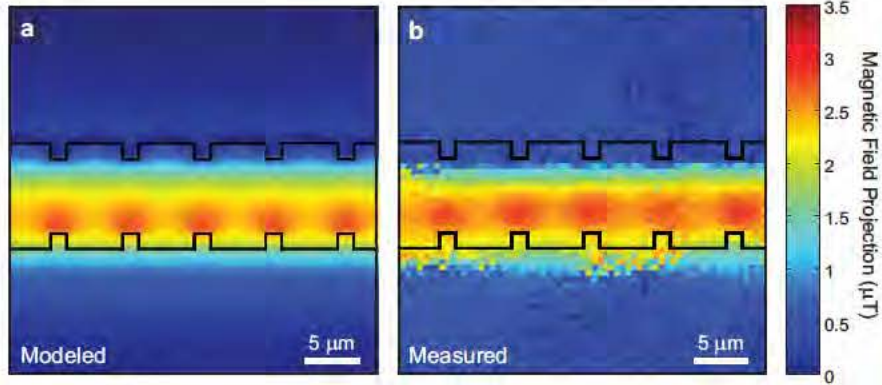
Figure 4.2: (a) Modeled and (b) measured map of the magnetic field projection along the NV axis produced by running an AC current of frequency 109.5 kHz and amplitude 50 μA through the notched wire pattern at a stand-off distance ≈ 1 μm.

current in order to account for spatial variations in the laser intensity and number of NV centers probed. In principle, such a calibration can also be accomplished using a homogeneous external AC field before measuring the field source of interest.

Applying microwave pulses resonant with only one NV orientation class, we extracted from the NV fluorescence intensity an image of the AC magnetic field projection along the chosen NV axis. Furthermore, the measured magnetic field map agrees very closely with our modeled field map (Figure 4.2). Discrepancies can be attributed to the position and orientation of the wire pattern with respect to the crystallographic structure of the diamond sample being slightly different from the estimated values used in the model. We suspect that a small drift of the sample mount position over the course of the measurement is responsible for the slight excess blurring in the measured magnetic field image.

The magnetic sensitivity can be measured experimentally as $\eta \equiv \delta B \sqrt{T} = \delta \mathcal{S} \sqrt{T} / \frac{\partial \mathcal{S}}{\partial B}$, where $\delta \mathcal{S}$ is the standard error in a set of fluorescence signal measurements, and $\frac{\partial \mathcal{S}}{\partial B}$ is the slope of the fluorescence signal $\mathcal{S}$ as a function of the AC magnetic field amplitude B [65]. To determine the sensitivity of the NV magnetic field imager under the measurement conditions given above, we applied a uniform 109.5 kHz AC field across the region of interest and measured the standard error $\delta \mathcal{S}$ of the fluorescence signal at each pixel. The measurements were conducted at an applied AC field amplitude corresponding to a point of maximum slope $\frac{\partial \mathcal{S}}{\partial B}$ in order to optimize the sensitivity, and the average-best sensitivity was calculated as the mean single-pixel sensitivity in a 25 μm $\times$ 25 μm area at the center of the gaussian laser excitation profile. Taking into account the time T required to make a magnetic field measurement, the resulting average-best sensitivity per 614 nm $\times$ 614 nm pixel was
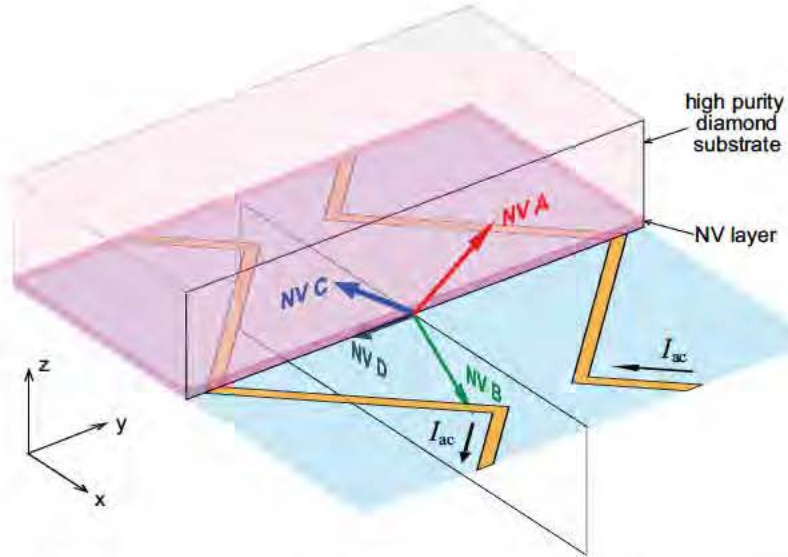
Figure 4.3: Diagram of zigzag wire pattern orientation with respect to the four NV axes.

$\approx 9~\mu\mathrm{T}/\sqrt{\mathrm{Hz}}$. Substituting experimental parameters such as measurement contrast, average number of photons collected per measurement, and measurement time, we calculated the expected shot-noise limited sensitivity per pixel to be $\approx 6~\mu\mathrm{T}/\sqrt{\mathrm{Hz}}$. The measured sensitivity is therefore in reasonable agreement with the shot-noise limited expected value [52]. We attribute the discrepancy to technical noise from the laser, which can be actively stabilized for future work.

4.4   Wide-field magnetic field patterns

The NV magnetic field imager is also capable of measuring magnetic field variations over a wide field of view simultaneously. For this demonstration, the magnetic field pattern was generated by counter-propagating AC currents through a pair of copper wires in a zigzag pattern with $\sim 100~\mu\mathrm{m}$ features. The field was measured by an ensemble of NV sensors occupying a thin layer near the surface of a diamond sample held flat against the copper strips (Figure 4.3).

Since the magnetic field pattern in this demonstration does not exhibit large variations in field at a sub-micron level, it was not necessary to use the nitrogen ion-implanted diamond sample as above. Instead, we employed a CVD-grown sample (Sample B) in which the bulk of the chip was grown in a low-nitrogen environment to produce a high-purity substrate. Additional nitrogen impurities were introduced near the end of the growth process, producing a $\sim 3~\mu\mathrm{m}$ thick layer of N-doped,
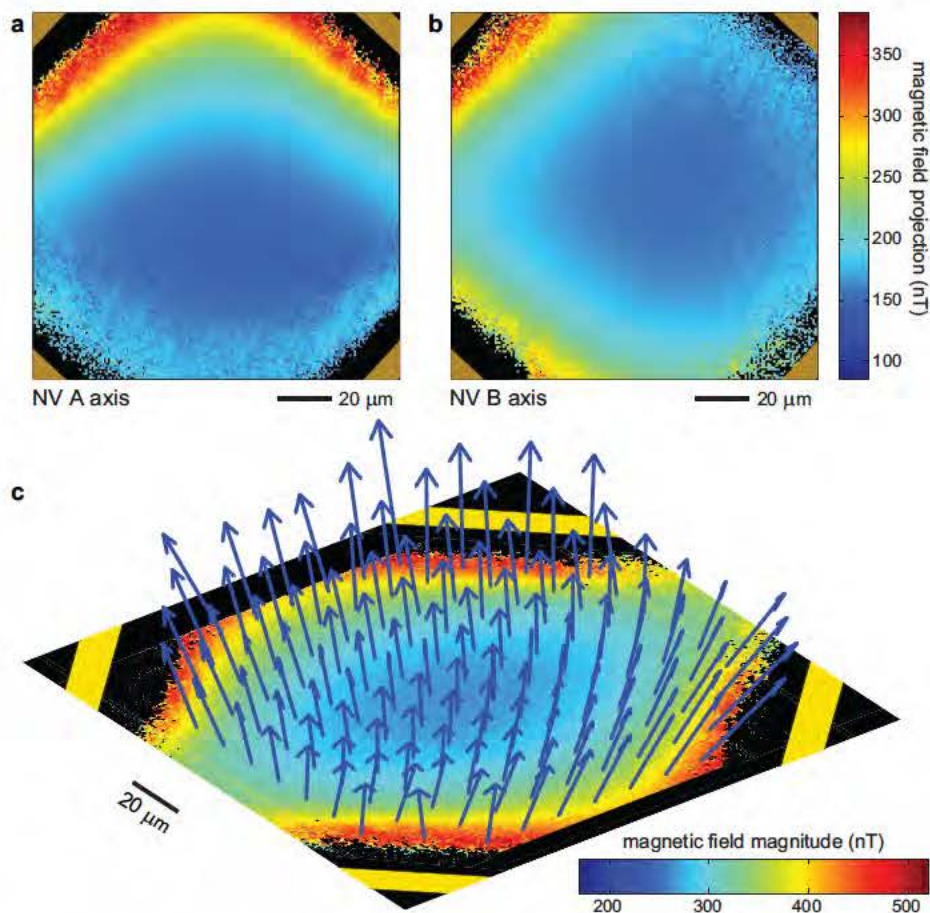
Figure 4.4: Map of the field projection along (b) NV A and (c) NV B axes measured when an AC current of frequency 4.75 kHz and amplitude 50 μA is run through the zigzag wire pattern. (d) A vector field map of the magnetic field reconstructed from field projections measured along two NV axes.

NV-rich diamond at the surface of the otherwise pure substrate. This layered sample geometry was confirmed by measuring the NV fluorescence as a function of depth using a scanning confocal microscope (see Appendix B.2 for details). Recall from Chapter 3 that the N-doped layer of Sample B has an estimated NV density of $\sim 1 \times 10^{14}$ cm^{-3} (~ 0.6 ppb) and an N density of $\gtrsim 2 \times 10^{16}$ cm^{-3} ($\gtrsim 100$ ppb), resulting in a paramagnetic nitrogen limited $T_2 \approx 280$ μs. The order of magnitude improvement in coherence time allows for more sensitive magnetometry; hence, such a CVD-grown sample is preferable in situations where the magnetic field varies on the scale of several microns.

The wire pattern was positioned with respect to the diamond chip such that its plane of symmetry coincided with the plane containing the NV axes 'NV B' and 'NV

D' (Figure 4.3). We first used a permanent magnet to apply a static field along the 'NV A' axis, resonantly coupled the microwave driving field to that NV population, and ran 4.75 kHz AC current through the wire pattern. Following the same measurement procedure described in the previous section, we extracted a 2D map of the resultant AC magnetic field projection along that axis, as sensed by the ensemble of NV centers near the surface of the diamond [Figure 4.4(a)]. Next, applying a static field of equal magnitude along the 'NV B' axis produced a 2D map of the magnetic field projection along a second axis [Figure 4.4(b)]. Taking advantage of the two-fold rotational symmetry of the diamond-wire configuration, we were able to use the two maps to reconstruct the magnetic field vector in the plane occupied by the NV ensemble [Figure 4.4(c)].

To determine the sensitivity of the NV magnetic field imager under the above imaging conditions, we applied a uniform 4.75 kHz AC field across the region of interest and measured the standard deviation $\delta\mathcal{S}$ of the fluorescence signal at each pixel. Again, the measurements were conducted at an applied field amplitude B that corresponded to a point of maximum slope $\frac{\partial\mathcal{S}}{\partial B}$ in order to optimize the sensitivity. The resulting average-best sensitivity per 614 nm × 614 nm pixel was ≈ 136 nT/$\sqrt{\text{Hz}}$. Substituting experimental parameters such as measurement contrast, average number of photons collected per measurement, and measurement time, we calculated an expected shot-noise limited sensitivity per pixel ≈ 86 nT/$\sqrt{\text{Hz}}$. The measured sensitivity is once again in reasonable agreement with the shot-noise limited expected value with the discrepancy attributable to technical noise from the laser.

4.5 Summary

In this work, we demonstrated an NV ensemble magnetic field imager capable of simultaneously measuring spatially varying AC magnetic field patterns over large fields of view ($\sim 100\,\mu$m) with sub-micron spatial resolution and achieving spin echo based magnetic field sensitivity $\sim 100\,\text{nT}\,\mu\text{m}^{3/2}/\sqrt{\text{Hz}}$.[1] The preliminary results presented here are an important first step toward potential biological and materials science applications of the NV ensemble magnetic field imager. However, we anticipate that a number of technical advances will be required for this device to reach its full potential. In the next several chapters, we will demonstrate some of these improvements.

---

[1]Note that the magnetic field sensitivity of the CCD-based NV ensemble magnetic field imager described in [59] was not measured experimentally and a spin echo technique was not employed (S. Steinert, private communication); hence the magnetic field sensitivity was limited by NV $T_2^* \sim 100$ ns.

Chapter 5

Preferential NV Orientation

5.1   Introduction

In this chapter, we explore the enhancement of NV magnetic field sensitivity through increased measurement contrast. Specifically, we demonstrate preferential orientation of NV centers along two of four possible crystallographic axes in diamonds grown by CVD on the {100} face. This preferential orientation provides increased NV ensemble measurement contrast and enhances AC magnetic field sensitivity, representing an important step towards NV ensemble based precision magnetometry and high-fidelity multispin-qubit quantum information processing.

As discussed in Chapter 1, due to the diamond crystal structure an NV center can be classified by the orientation of its symmetry axis along one of four possible crystallographic axes: $[111], [1\bar{1}\bar{1}], [\bar{1}1\bar{1}]$, and $[\bar{1}\bar{1}1]$ (Figure 5.1). In most diamond samples, NV centers occupy these four orientations equally. To spectrally distinguish a single NV orientation class, a static magnetic field is applied along the relevant crystallographic axis, which maximally splits the degeneracy between $|\pm 1\rangle$ sublevels for the desired NV orientation class [85, 86]. This typically limits coherent NV spin manipulation via a resonant MW field to only one quarter of the NV population, with the rest of the NV centers contributing background fluorescence and thereby degrading measurement contrast. Thus, preferential orientation of NV centers along a subset of the four crystallographic axes would benefit NV ensemble applications both by employing a greater fraction of the NV center population as well as by reducing background fluorescence.

It was recently shown that for synthetic diamond grown via CVD on {110}-oriented substrates, NV centers can be incorporated into the lattice as a unit and thereby found in only two orientations [8]. Here we show for the first time that preferential NV orientation can also be realized for CVD diamond samples grown on
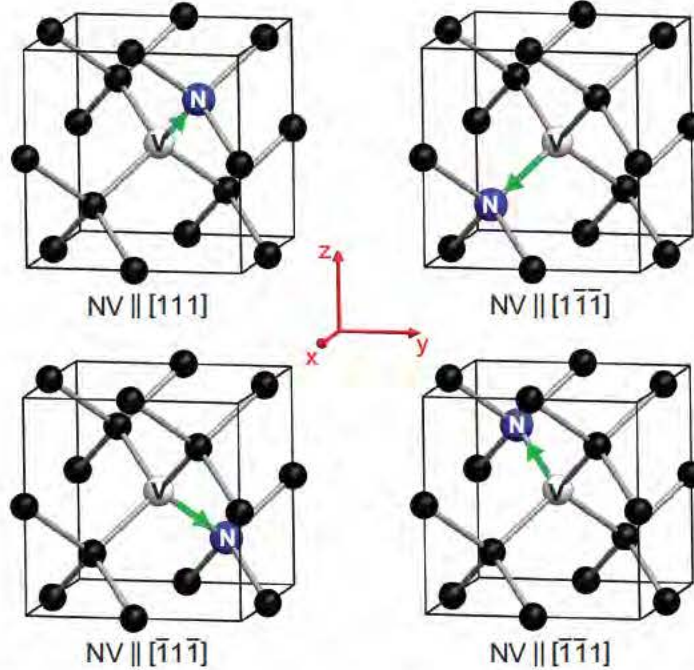
Figure 5.1: Four orientations of the NV center in diamond. Carbon atoms are depicted in black, nitrogen (N) atoms in blue, and vacancies (V) in white. The NV electronic spin is indicated by green arrows. Four additional orientations are possible by flipping the nitrogen atoms and vacancies in each configuration above; however, orientations with equivalent symmetry axes are spectrally indistinguishable and may therefore be considered in the same NV orientation class.

{100}-oriented substrates, which are more commonly available and more compatible with increased area bulk production [87], making them more suitable for applications such as bulk magnetometry. We describe the growth regime and likely mechanism leading to preferential NV orientation. We then present experimental demonstrations that diamond with preferential NV orientation exhibits higher measurement contrast and as a result provides improved AC magnetic field sensitivity.

5.2 Preferential NV orientation in {100} samples

5.2.1 Results

We employed a wide-field fluorescence microscope (see Appendix B.1 for details) to perform ESR measurements on ensembles of NV centers in two {100}-oriented
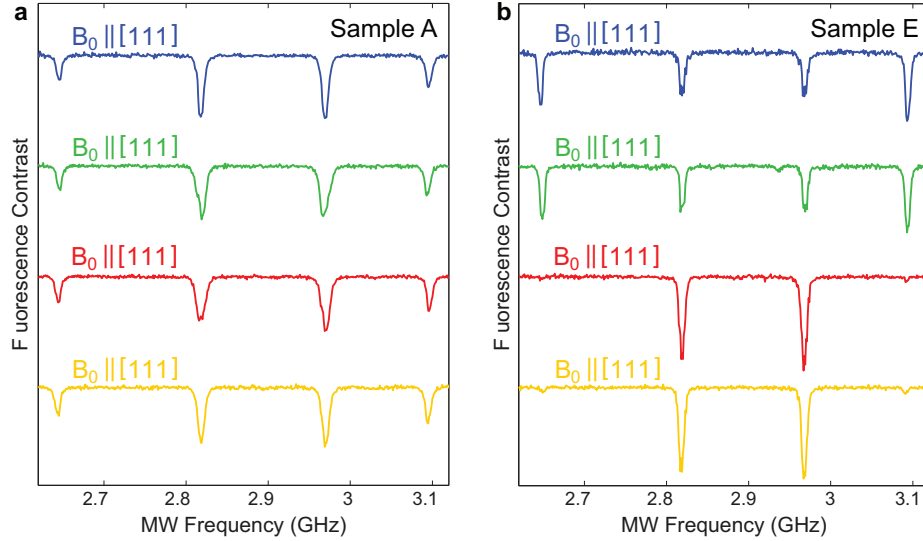
Figure 5.2: ESR spectra with static magnetic field ($B_0 = 80$ G) along each of four diamond crystallographic axes for (a) Sample A, which exhibits no preferential NV orientation, and (b) Sample E, which exhibits a high level ($\sim 94\%$) of preferential NV orientation.

CVD-grown bulk diamond samples: one with NV centers populating the four orientation classes equally (Sample A) and one with preferential NV orientation along two crystallographic axes (Sample E). The two samples have similar densities of NV centers [NV $\sim 5 \times 10^{12}$ cm^{-3} (~ 0.03 ppb) for Sample A, NV $\sim 3 \times 10^{12}$ cm^{-3} (~ 0.02 ppb) for Sample E] and spin coherence lifetimes (T$_2 \approx 480\,\mu$s for Sample A, T$_2 \approx 530\,\mu$s for Sample E). Sample A contains a natural isotopic abundance of ^{13}C (1.1%) whereas Sample E is isotopically pure (0.01% ^{13}C). Note that though longer NV spin coherence times have been measured in high-purity diamonds with similar isotopic concentrations of ^{13}C [1], paramagnetic impurities due to substitutional nitrogen limit the coherence of Sample E to a lifetime that is comparable to that of Sample A. For each sample, NV centers within a $10\,\mu$m-diameter cross-sectional area were optically excited and subsequent NV fluorescence was collected from a $6\,\mu$m $\times$ $6\,\mu$m $\times$ $50\,\mu$m detection volume; the NV spins were driven at Rabi frequency $\gtrsim 10$ MHz.

To determine the relative population of the four NV orientation classes in the two samples, we applied a static field ($B_0 = 80$ G) along each of the four diamond crystallographic axes (i.e., NV axes) and measured the resulting ESR spectra. For such magnetic field configurations, four NV ESR resonances are observed: one pair of resonances corresponds to the $|0\rangle \leftrightarrow |\pm 1\rangle$ transitions for the class of on-axis NV centers that are oriented parallel to B_0 (at 2.64 GHz and 3.10 GHz for $B_0 = 80$ G); another pair of NV ESR resonances corresponds to the three classes of off-axis NV centers that are not aligned with B_0 (at 2.82 GHz and 2.97 GHz for $B_0 = 80$ G). In
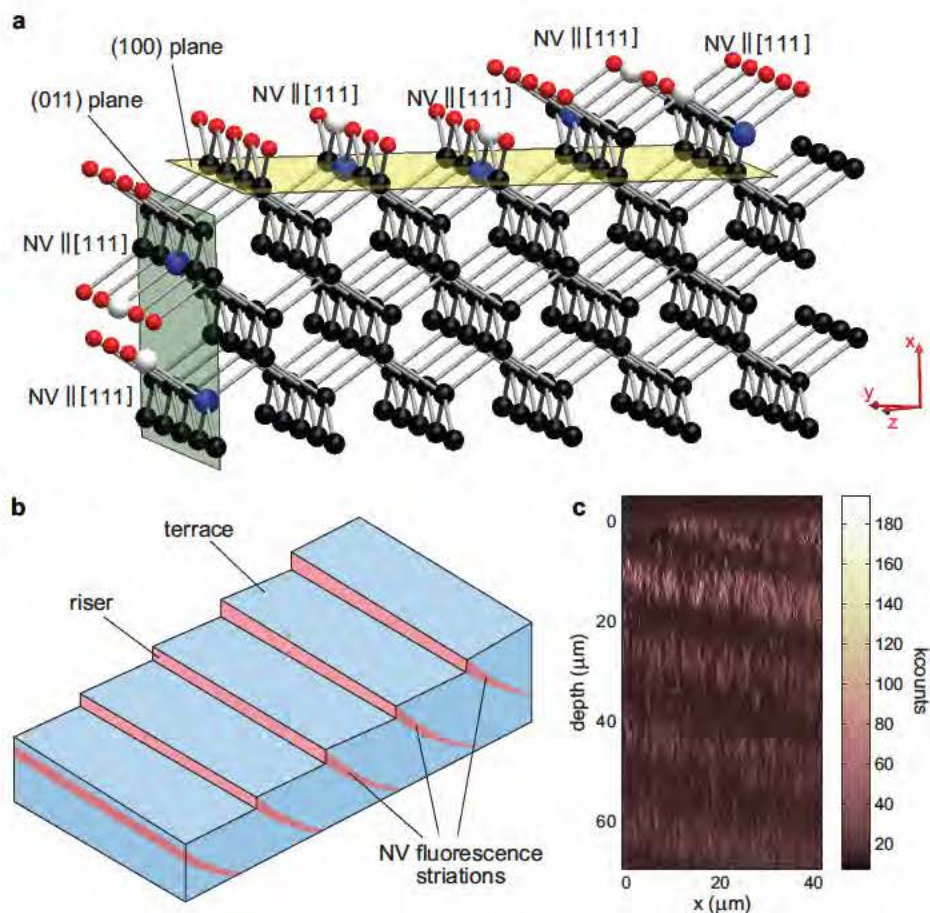
Figure 5.3: (a) Atomic-level model of NV incorporation in (100) step-flow growth, indicating mechanism for preferential NV occupation of only two orientations. (b) Diagram of {100} step-flow growth surface and fluorescence striations. (c) Confocal cross-section of a sample which exhibits fluorescence striations characteristic of {100} step-flow growth.

Sample A, the observed amplitudes of the NV resonances in the ESR spectra were very similar for each of the four static magnetic field configurations, indicating equal population of NV centers in the four orientation classes [Figure 5.2(a)]. In Sample E, however, the pair of on-axis NV ESR resonances were found to be very weak (i.e., small amplitude) for the static magnetic field configurations $B_0 \parallel [\bar{1}1\bar{1}]$ and $B_0 \parallel [\bar{1}\bar{1}1]$, indicating a high fraction of NV centers with preferential orientation [Figure 5.2(b)]. From the measured relative amplitudes of the two pairs of NV ESR resonances, we estimate that $\sim 94\%$ of the NV centers in the Sample E detection volume are oriented along either the $[111]$ or $[1\bar{1}\bar{1}]$ directions. Similar ESR spectra measured across Sample E indicate a comparable fraction of preferential NV orientation (within several percent) over the whole sample surface.
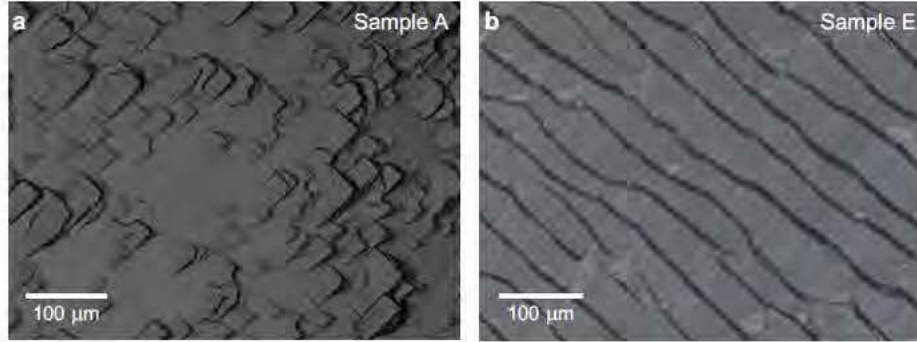
Figure 5.4: Microscope images of the surface morphologies of (a) Sample A (scanning confocal) and (b) Sample E (differential interference contrast).

5.2.2 Discussion

In the idealized picture of CVD growth on the (100) surface (or any of the symmetrically equivalent $\{100\}$ faces), a substitutional nitrogen atom can be incorporated at a lattice site in two configurations: (i) the two remaining bonds above the nitrogen allow a vacancy to form an NV center with a $[\bar{1}\bar{1}1]$ or $[\bar{1}1\bar{1}]$ orientation with equal probability or (ii) the two remaining bonds above the nitrogen allow a vacancy to form an NV center with a $[\bar{1}11]$ or $[1\bar{1}\bar{1}]$ orientation with equal probability. Thus in the idealized picture of CVD growth on a $\{100\}$ surface, the four possible NV orientation classes form with equal probability [Figure 5.3(a)]. However, for certain conditions of substrate temperature and flow of nitrogen gas through the CVD chamber, growth on a $\{100\}$ surface may occur via a step-flow mode [12]. In this growth mode, the surface morphology is stepped (comprising low angle risers and horizontal terraces), as shown in Figure 5.3(b), which potentially allows the formation of higher angle facets, such as the $\{110\}$, to form. Furthermore, in the step-flow growth regime NV centers are incorporated more readily into the risers rather than the terraces [88], which results in visible striations in the fluorescence image of the diamond, as shown in Figure 5.3(c). We hypothesize that the preferential incorporation of NV centers in $\{110\}$ facets on the risers can allow for preferential NV orientation to be realized in $\{100\}$-oriented CVD diamond via the same mechanism that allows preferential NV orientation in $\{110\}$-oriented CVD diamond [8].

As seen in Figure 5.4(a), the surface morphology of Sample A is not stepped, indicating that it was not grown under step-flow conditions, which is consistent with the observed lack of preferential NV orientation in this sample. In contrast, the surface morphology of Sample E is stepped [Figure 5.4(b)], indicating that it was grown under step-flow conditions, which is consistent with the observed preferential NV orientation of this sample. We have also observed varying levels of preferential NV orientation in several additional $\{100\}$-oriented CVD samples exhibiting stepped
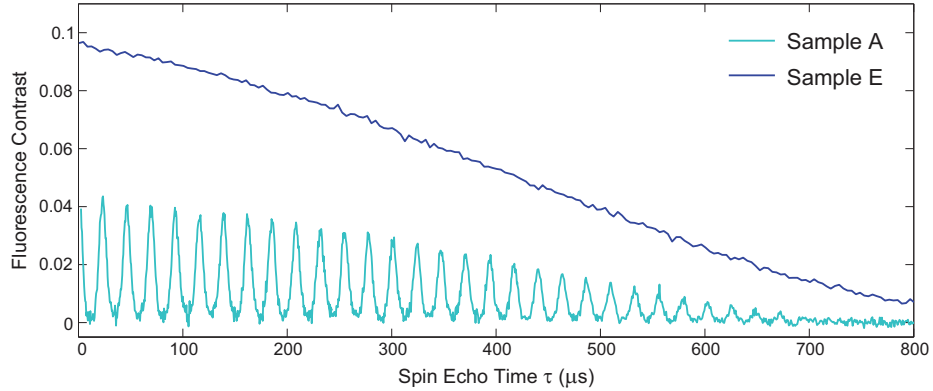
Figure 5.5: Comparison of the measurement contrast of the NV spin coherence decay curves measured for the non-oriented Sample A and preferentially-oriented Sample E.

surface morphology and fluorescence striations characteristic of step-flow growth. Detailed characterization of the growth factors determining the presence and level of preferential NV orientation will be the focus of future work.

5.3 Enhanced AC magnetometry

5.3.1 Results

In Figure 5.5 we present NV spin coherence decay curves that demonstrate the expected factor of $\gtrsim 2$ improvement in NV ensemble measurement contrast for Sample E (preferential NV orientation along two axes) relative to Sample A (equal populations of all NV orientations). Note that Sample A exhibits collapses and revivals in the measured NV spin coherence, which result from the Larmor precession of ^{13}C impurities in this sample [41]. This effect does not alter the decoherence envelope, which is similar for both samples.

As discussed in Chapter 2, the improvement in measurement contrast for samples with preferential NV orientation improves NV magnetic sensitivity. Recall, in the standard AC magnetometry measurement utilizing a spin echo pulse sequence, the optimum AC magnetic field sensitivity is given approximately by [52]:

$$\eta_{se} \approx \frac{\pi\hbar}{2g\mu_{B}} \frac{1}{\alpha(T)\sqrt{\beta}\tau_{ac}}, \tag{5.1}$$

where α is the measurement contrast, β is the number of photons collected per measurement, and the measurement time is approximated by the period of the AC mag-
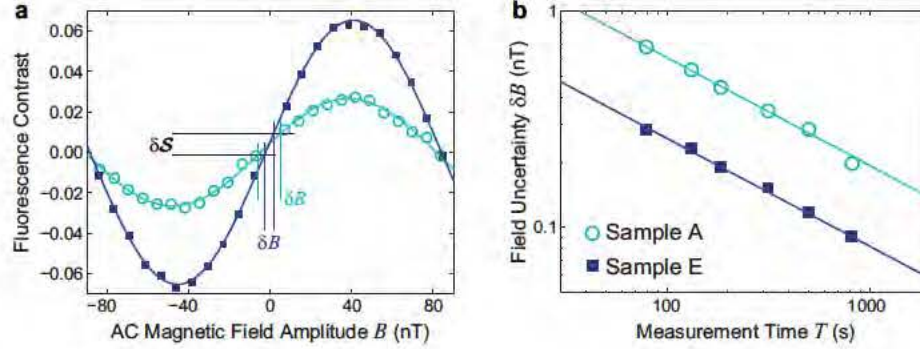
Figure 5.6: Comparison of NV magnetic sensitivity for Samples A and E. (a) NV magnetometry signal (i.e., fluorescence contrast) due to an AC magnetic field of frequency $f_{ac} = 3.08$ kHz as a function of the magnetic field amplitude B, acquired using same method as described in Chapter 4. (b) Uncertainty δB in the measured AC magnetic field amplitude as a function of measurement time T. As discussed previously, the magnetic sensitivity $\eta_{se} \equiv \delta B \sqrt{T}$. Note that the measurement contrast of Sample E is $\gtrsim 2$ times larger than of Sample A, leading to similarly improved magnetic field sensitivity.

netic field τ_{ac}. Note that the measurement contrast is modified by NV spin decoherence over the measurement time $T \approx \tau_{ac}$.

In Figure 5.6(a), we plot the measured NV magnetometry signal (i.e., fluorescence contrast) as a function of applied AC magnetic field amplitude for both the preferentially oriented Sample E and the standard (non-oriented) Sample A, using the spin echo sequence with an AC magnetic field of frequency $f_{ac} = 3.08$ kHz. The enhanced measurement contrast from the preferentially oriented sample improves the magnetic field sensitivity by a factor $\gtrsim 2$. As shown in Figure 5.6(b), we find that the AC magnetic field sensitivity in the detection volume ($6 \, \mu m \times 6 \mu m \times 50 \, \mu m$) for the preferentially oriented Sample E is $2.6 \pm 0.1 \, nT/\sqrt{Hz}$, whereas the sensitivity for the standard Sample A is $6.1 \pm 0.2 \, nT/\sqrt{Hz}$.

5.3.2 Discussion

Other contributions to AC magnetic field sensitivity

Samples A and E were chosen for this work because they are similar in most aspects excepting the presence or absence of preferential NV orientation. However, the two samples are not identical; they differ slightly in isotopic composition, NV density, and spin coherence time. Therefore, in order to properly compare the effect of preferential NV orientation on AC magnetic field sensitivity, we must perform a detailed analysis of the contributions from these other differences.

Chapter 5: Preferential NV Orientation

The AC magnetic field sensitivity given by Equation 5.1 can be re-written as:

$$\eta_{\text{se}} \approx \frac{\pi\hbar}{2g\mu_{\text{B}}} \frac{1}{\alpha_0 \exp\left[-(\tau_{\text{ac}}/\text{T}_2)^p\right]} \frac{1}{\sqrt{\beta_0 n_{\text{NV}} \tau_{\text{ac}}}} \tag{5.2}$$

The Equation 5.1 parameter $\alpha(T)$ is here recast in terms of the initial measurement contrast α_0 and the reduction in measurement contrast at measurement time $T \approx \tau_{\text{ac}}$ due to decoherence characterized by T_2 and exponential power p. The number of NV fluorescence photons collected per measurement β depends on the number of NV spins n_{NV} contributing to the measurement and the number of photons collected from a single NV in one measurement β_0, which in turn is dependent on collection efficiency, and factors such as excitation laser power and optical detection pulse duration. We now consider the contributions of differences in sample isotopic composition, NV density, and spin coherence time separately.

Isotopic composition   Sample A has a natural abundance (1.1%) of ^{13}C, whereas Sample E was isotopically engineered to contain 0.01% ^{13}C. As mentioned previously, the higher concentration of ^{13}C in Sample A results in periodic collapses and revivals characteristic of ^{13}C Larmor precession in the coherence curve (Figure 5.5). By performing measurements on an AC magnetic field with a frequency corresponding to the center of a revival (or alternatively, by applying a static magnetic field such that the center of a revival corresponds to the frequency of the AC magnetic field one desires to measure), the collapses and revivals may be ignored, and only the effect of ^{13}C on the decoherence envelope need be considered. We also note that although the diamond lattice parameters are quantitatively different for samples with different isotopic concentrations of carbon, the growth morphology for these particular samples is dominated by the growth conditions and especially the amount of nitrogen incorporated. As such, there is no distinguishable effect due to the ^{12}C diamond lattice parameter on the growth morphology of these samples.

Coherence time   In Figure 5.7, the NV spin decoherence curves are replotted in terms of coherence rather than contrast. From the fits to the decoherence envelope (Sample A) and curve (Sample E), we extract fit parameters $\text{T}_2 = 479 \pm 2\ \mu\text{s}$ and $p = 2.46 \pm 0.04$ for Sample A, and $\text{T}_2 = 527 \pm 1\ \mu\text{s}$ and $p = 2.01 \pm 0.02$ for Sample E. Even though there are small differences in the decoherence behavior of the samples, the actual coherence levels at the time $\tau_{\text{ac}} = 324.416\mu\text{s}$ corresponding to the frequency of the applied AC magnetic field are quite similar: 0.682 for Sample A and 0.697 for Sample E, as calculated from the fits. Thus we expect that the difference in NV spin coherence time between the two samples will contribute to a factor 1.022 improvement in the sensitivity of Sample E compared to that of Sample A.

Chapter 5: Preferential NV Orientation
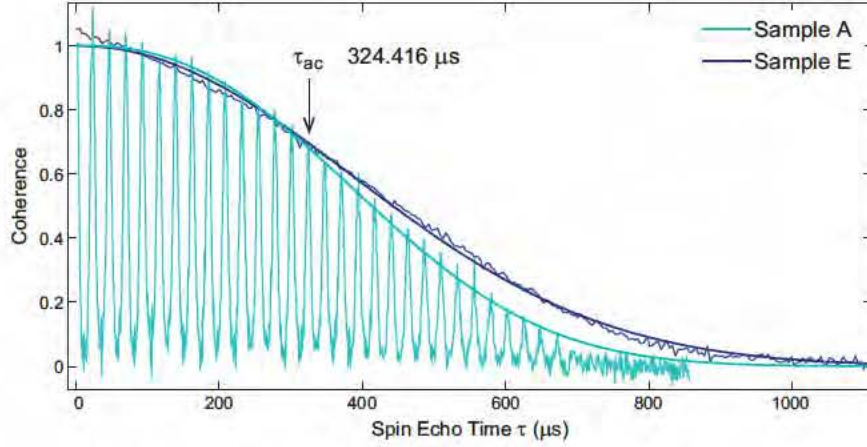
Figure 5.7: Coherence-normalized NV spin coherence decay of Samples A and E, where the thicker lines denote fits to decoherence envelopes of the form $\exp\left[-(\tau/T_2)^p\right]$. The AC magnetic field period τ_{ac} is indicated with an arrow.

NV density   The NV densities of Samples A and E were determined from the NV fluorescence measured using a scanning confocal microscope (see Appendix B.2 for details). The NV densities were found to be NV $\sim 5 \times 10^{12}$ cm^{-3} (~ 0.03 ppb) for Sample A, and NV $\sim 3 \times 10^{12}$cm^{-3} (~ 0.02 ppb) for Sample E. However, the sensitivity is dependent on the number of NV spins contributing to the measurement n_{NV}; thus only one quarter of the NV centers in Sample A contribute ($n_{NV} \sim 1.25 \times 10^{12}$ cm^{-3}) whereas roughly one half of the NV centers in Sample E contribute ($n_{NV} \sim 1.5 \times 10^{12}$ cm^{-3}). As a result, we expect that the difference in NV density between the two samples will contribute to a factor 1.095 improvement in the sensitivity of Sample E compared to that of Sample A.

Combined effect   We measured AC magnetic field sensitivity (in a $6\,\mu$m $\times\, 6\,\mu$m $\times\, 50\,\mu$m detection volume) to be 6.1 ± 0.2 nT$/\sqrt{\text{Hz}}$ for Sample A and 2.6 ± 0.1 nT$/\sqrt{\text{Hz}}$ for Sample E, corresponding to a factor 2.3 ± 0.1 difference in measured sensitivity. The combined effect of the small differences in spin coherence time and NV density between the two samples gives a factor 1.07 improvement in the sensitivity of Sample E compared to that of Sample A. Removing these contributions from the measured sensitivity still yields a factor > 2 improvement in the sensitivity of the preferentially oriented Sample E compared to the standard Sample A.

Limitations of preferential NV orientation

Though samples with preferential NV orientation provide a simple way to improve NV ensemble magnetometry sensitivity by a factor of $\gtrsim 2$, there are some caveats to keep in mind. First, since magnetic field projections in three directions are necessary for a full vector reconstruction, samples in which NV centers are preferentially oriented along only two crystallographic axes are less compatible with vector magnetometry. Second, it should be noted that the step-flow growth mode and corresponding fluorescence striations indicate inhomogeneity in NV distribution over $\sim 10\mu$m. However, this effect is less important for measurements using bulk diamond and may be removed through careful calibration in samples with thinner NV layers. Finally, preferential orientation of NV centers has thus far only been observed in CVD-grown samples, as a byproduct of the growth process. Unfortunately, typical N-to-NV conversion achieved in as-grown CVD diamonds is typically $< 0.5\%$, and standard processing techniques to increase the NV concentration (e.g., nitrogen ion implantation, irradiation, and annealing) also destroy the preferential NV orientation. This limitation may possibly be overcome by introducing external strain to the crystal during annealing to cause the NV centers to re-orient along a preferred direction. Such a technique has been demonstrated with neutral carbon $<100>$-split interstitial defects in diamond [89]; however, the same has yet to be attempted on NV centers.

5.4   Summary

In summary, we demonstrated that CVD diamond grown on the {100} crystallographic face can yield NV centers that are preferentially oriented along two of the four possible crystallographic axes. We attribute this effect to the creation of terraces and risers in the step-flow growth morphology such that NV centers are incorporated mainly into the risers, which can contain higher angle facets such as {110} and thus accommodate only two NV orientations. We showed that this preferential orientation increases the NV ensemble measurement contrast by about a factor of two and enables a similar enhancement in AC magnetometry sensitivity. The discovery of preferential orientation in diamond grown on the {100} surface, which is the most widely available and frequently used type of CVD diamond, could inform future research in material science and allow the design and growth of optimized diamond samples with tailored NV orientations to benefit a wide variety of applications in precision magnetometry and quantum science.

Chapter 6

Dynamical Decoupling

Pursuing more sensitive NV magnetometery by probing a large number of NV centers to increase fluorescence signal is one of the major focuses of this dissertation. However as discussed in previous chapters, this NV ensemble magnetometry approach has trade-offs; for example, in ensemble measurements fluorescence from non-resonant NV orientation classes can contribute to the background signal, reducing measurement contrast and subsequently magnetic field sensitivity. In Chapter 5, we discussed the use of samples with preferentially oriented NV centers in order to recoup this loss in measurement contrast.

Another issue comes from the higher NV concentrations typically desired for ensemble measurements compared to those performed on single NV centers. In order to achieve higher NV concentrations, higher concentrations of nitrogen must be incorporated into the diamond sample. The corresponding higher concentration of paramagnetic impurities reduces the NV spin coherence time and subsequently NV magnetic field sensitivity. Even in samples with low nitrogen concentration, the ^{13}C nuclear spins in natural abundance samples limit the NV coherence time to $\sim 600\,\mu$s [65, 51, 86]. Recently, however, dynamical decoupling techniques have been employed to reduce the effective interaction of single NV spins with other spin impurities in the environment, specifically in impurity environments dominated either entirely by nitrogen electronic spins (~ 100 ppm) [90, 64] or entirely by ^{13}C nuclear spins [91, 71], thereby enabling significant improvements in the NV single spin coherence lifetime [90, 91, 71] and AC magnetic field sensitivity [64, 71].

In this chapter, we demonstrate the equally successful application of dynamical decoupling to large numbers of NV spins ($> 10^3$), despite the greater inhomogeneities in local impurity environment and subsequently less optimal average control pulse fidelity as compared to addressing single NV spins. Employing multipulse Carr-Purcell-Meiboom-Gill (CPMG) control sequences [92, 93], we realize an order of magnitude extension of the NV ensemble spin coherence time at room temperature in three di-

amond samples with widely differing NV densities and spin impurity concentrations, including two impurity environment regimes for which NV dynamical decoupling has not previously been demonstrated. We also show that the scaling of the NV spin coherence time with the number of pulses in the control sequence depends non-trivially on the concentration of N and ^{13}C impurities and can differ from the scaling obtained in previous single NV measurements [90, 91, 71]. For some samples, the NV ensemble spin coherence time is increased to > 2 ms, where it begins to be limited by NV spin-lattice relaxation ($T_1 \approx 6$ ms at room temperature).

We then apply these dynamical decoupling techniques to a fourth diamond sample over a range of temperatures ($77\,\text{K} - 300\,\text{K}$) in order to suppress both decoherence [3] and phononic spin relaxation [94]. We demonstrate an extension of the NV spin coherence time to ~ 0.6 s at 77 K, which corresponds to an additional improvement of more than two orders of magnitude compared to previous NV measurements [1, 3] and is on par with the longest coherence times achieved for electronic spins in any solid-state system [95]. Over a wide range of temperatures we also find that the NV spin coherence time is limited to approximately half of the longitudinal spin relaxation time, a finding that could be relevant to other solid-state spin defects (e.g., P donors in Si). Finally, we demonstrate a ten-fold enhancement in NV ensemble sensing of AC magnetic fields at room temperature, with greater NV magnetic sensitivity enhancement expected at lower temperatures.

6.1   Background

As discussed previously, the NV spin environment (i.e., spin bath) is typically dominated by ^{13}C and N impurities, randomly distributed in the diamond crystal. These spin impurities create time-varying local magnetic fields at each NV spin, which can be approximated as an average field that fluctuates on a time scale set by the mean interaction between spins in the bath, thereby inducing rapid dephasing of freely precessing NV spins on a time scale $T_2^* \sim 1\,\mu$s for typical spin impurity concentrations. By applying a single resonant MW π pulse to refocus the dephasing, the spin echo sequence [Figure 6.1(a)] decouples NV spins from bath field fluctuations that are slow compared to the free precession time. Application of additional control pulses, such as n-pulse CPMG and XY sequences, have recently been shown to decouple single NV spins from higher frequency bath fluctuations [90, 91, 71].

CPMG.   The CPMG pulse sequence, widely used in the field of NMR [92, 93], is a simple extension of the spin echo sequence in which the single refocusing π pulse is replaced with n periodically spaced refocusing π pulses. Furthermore, by modulating the phase of the MW carrier signal, the spin rotation axis of the π pulse
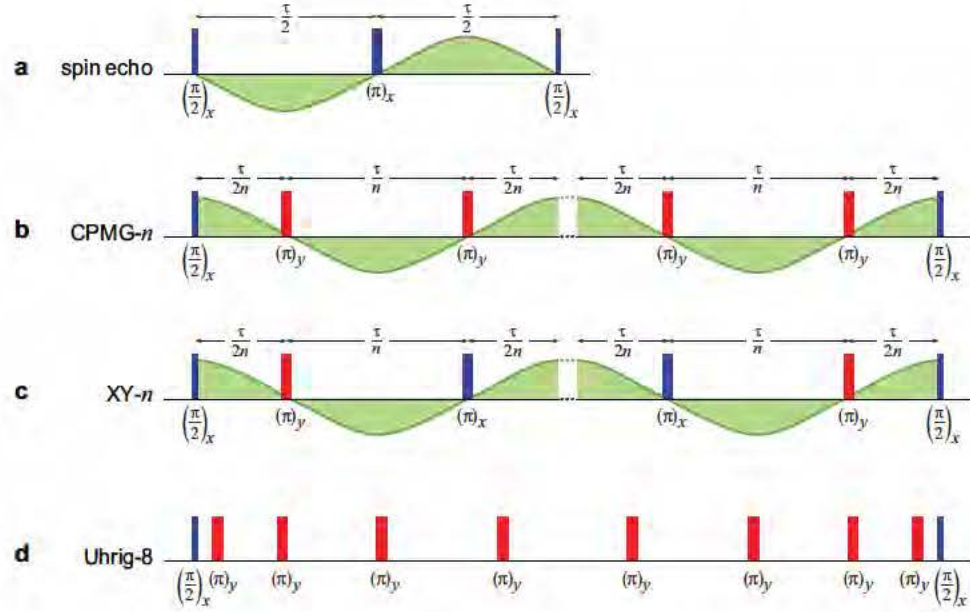
Figure 6.1: Pulse diagrams of several dynamical decoupling sequences: (a) spin echo, (b) n-pulse CPMG, (c) n-pulse XY, and (d) example Uhrig with $n = 8$ pulses. For the dynamical decoupling schemes with periodic pulse spacing, the optimal timing of the control pulses with respect to an AC magnetic field of frequency $f_{ac} = n/(2\tau)$ (green) is shown.

train is chosen to be perpendicular to that of the first and last $\pi/2$ pulses for the preparation and detection, respectively, of the NV spin superposition state. For example, Figure 6.1(b) shows a CPMG control sequence in which the $\pi/2$ pulses are rotated about the x axis and the π pulses are rotated about the y axis. Rotating the NV spin about two different axes in this manner allows CPMG pulse sequences containing an even number of pulses to compensate for pulse errors along one spin rotation axis [the y axis in the Figure 6.1(b) example]. As a result, the CPMG pulse sequence is one of the most robust, given a known initial spin state. However, in many proposed NV applications including precision magnetometry and quantum information processing the initial spin state is unknown and two-dimensional pulse error correction is necessary.

XY. As shown in Figure 6.1(c), the XY family of pulse sequences extends upon the CPMG sequence by alternating the spin rotation axes of the refocusing π pulses in order to compensate for pulse errors along both the x and y axes, thereby achieving pulse error correction along all directions [96]. As a result, the XY family of pulse sequences is ideal for NV applications such as precision magnetometry and quantum information processing, where the initial spin state is unknown. However, in practical

measurements, the CPMG sequence still performs marginally better in situations where the initial spin state is known.

Uhrig. It is also worthwhile to mention Uhrig dynamical decoupling sequences [97], which have attracted a fair amount of attention recently [90, 91, 63] as a nonperiodic alternative to the CPMG and XY pulse sequences [Figure 6.1(d)]. However, the Uhrig sequences are most effective at decoupling from noise with a sharp high-frequency cut-off [98], making them less suitable for NV centers, which experience a smoother spin bath spectrum. Furthermore, the sequence does not compensate for pulse errors, and the nonperiodic pulse spacing is incompatible with refocusing NV spin dephasing due to ^{13}C Larmor precession. As a result, this chapter addresses only the periodic CPMG and XY pulse sequences.

6.2 Dynamical decoupling at room temperature

For measurements at room temperature, we used a custom-built wide-field fluorescence microscope (see Appendix B.1 for details) to perform dynamical decoupling on NV ensembles in three diamond samples with different NV densities and spin impurity environments. Applying a static field along one of the diamond crystallographic axes selected approximately one quarter of the NV centers in the 10 μm-diameter detection cross-section to be resonant with the MW pulses. Each diamond sample consisted of an NV-rich layer CVD-grown on a non-fluorescing diamond substrate, such that all collected fluorescence is attributed to the NV-rich layer.

6.2.1 Results

The NV-rich layer of Sample F was 16 μm thick and contained NV concentration $\sim 1 \times 10^{16}$ cm^{-3} (~ 60 ppb) [extracted from NV fluorescence measurements performed with a confocal microscope (see Appendix B.2 for details)], N concentration $\sim 2 \times 10^{19}$ cm^{-3} (~ 100 ppm) [measured using secondary ion mass spectroscopy (SIMS)], and 1.1% natural abundance ^{13}C concentration. The high N concentration dominated NV decoherence in this sample, limiting the measured spin echo ensemble coherence time to $T_2 \approx 2\,\mu$s. We applied CPMG-n sequences and measured the NV ensemble spin coherence as a function of the full spin evolution time τ; several representative NV ensemble spin coherence decay curves are shown in Figure 6.2. As usual, we extracted $T_2^{(n)}$ from each decoherence curve by fitting the data to a stretched exponential function $\exp\left[-(\tau/T_2^{(n)})^p\right]$ and observed an extension in $T_2^{(n)}$ by a factor > 10 for $n = 128$. Furthermore, we found that $T_2^{(n)}$ exhibited a power-law dependence

Figure 6.2: Example NV ensemble coherence decay curves measured using CPMG-n pulse sequences in Sample F. The solid lines denote fits to the decoherence envelope of the form $\exp\left[-\left(\tau/T_2^{(n)}\right)^p\right]$.

on n: $T_2^{(n)} \propto n^s$, with $s = 0.65 \pm 0.02$, which is consistent with the value $s \approx 0.67$ found recently for single NV centers in similarly nitrogen-rich diamond samples [90]. These results demonstrate that inhomogeneities in the spin bath and MW field do not limit the effectiveness of dynamical decoupling for extending NV ensemble coherence times by at least an order of magnitude.

The NV-rich layers of Samples B and C had much lower NV and N concentrations than found in Sample F: NV $\sim 1 \times 10^{14}$ cm^{-3} (~ 0.6 ppb), N $\gtrsim 2 \times 10^{16}$ cm^{-3} ($\gtrsim 100$ ppb) for Sample B and NV $\sim 1 \times 10^{14}$ cm^{-2} (~ 0.6 ppb), N $\sim 2 \times 10^{17}$ cm^{-2} (~ 1 ppm) for Sample C. Sample B contained 1.1% natural abundance ^{13}C such that both N and ^{13}C contributed to NV decoherence, resulting in periodic collapses and revivals in the NV spin coherence associated with ^{13}C Larmor precession [41]. In contrast, Sample C was isotopically engineered with 0.01% ^{13}C such that N impurities dominated NV decoherence. Despite these differences in spin impurity environments, we measured similar spin echo NV ensemble spin coherence times ($T_2 \sim 300$ μs) for the two samples. By applying n-pulse CPMG dynamical decoupling sequences, we extended the NV ensemble spin coherence time [Figures 6.3 and 6.4], achieving $T_2^{(n)} \sim 2$ ms for both samples, comparable to the longest coherence time reported for dynamical decoupling applied to single NV centers [71].
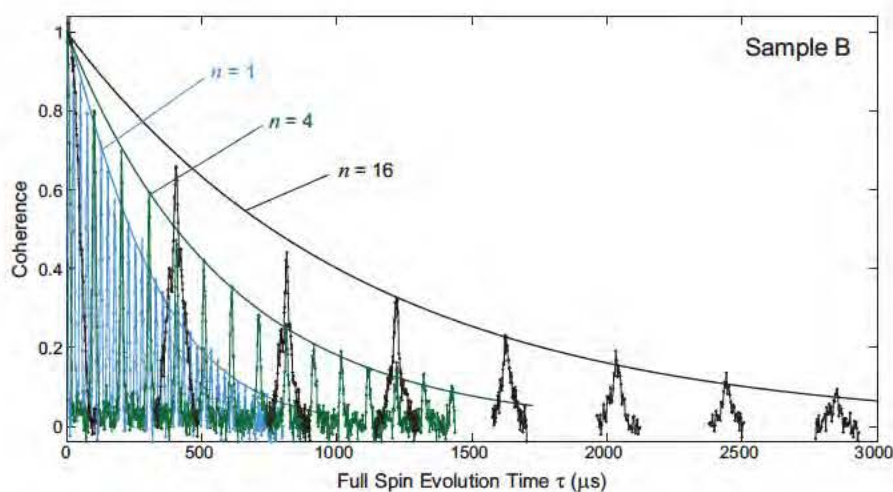
Figure 6.3: Example NV ensemble coherence decay curves measured using CPMG-n pulse sequences in Sample B. Note that the time axis is plotted with a linear scale due to the periodic collapses and revivals in the NV spin coherence associated with ^{13}C Larmor precession. These collapses and revivals occur in samples where the ^{13}C abundance is high enough to contribute significantly to NV decoherence. The solid lines denote fits to the decoherence envelope of the form $\exp\left[-\left(\tau/T_2^{(n)}\right)^p\right]$.
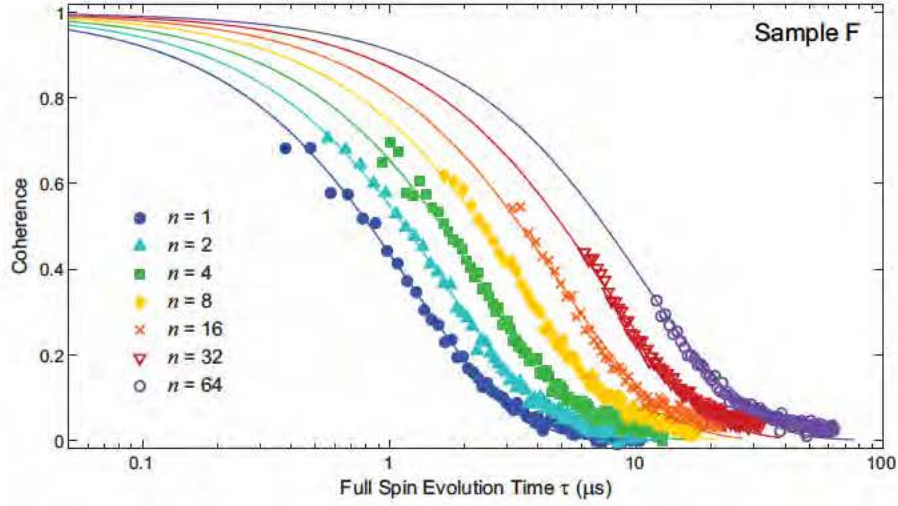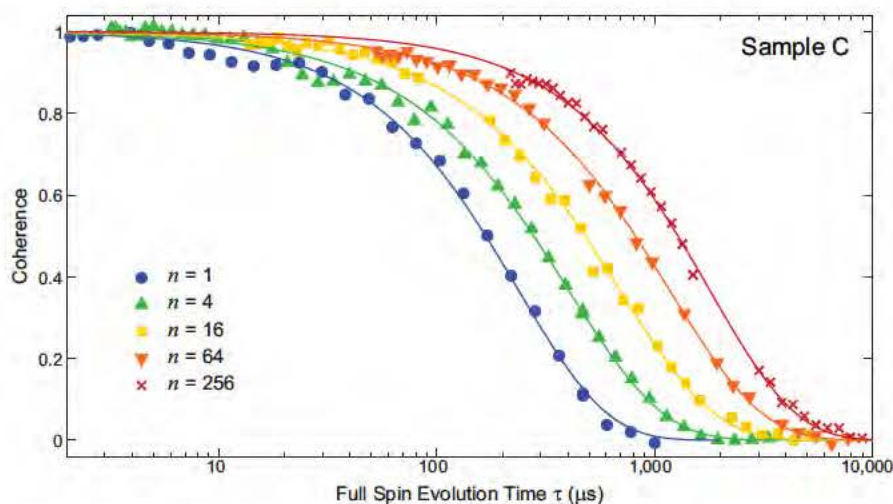

Figure 6.4: Example NV ensemble coherence decay curves measured using CPMG-n pulse sequences in Sample C. The solid lines denote fits to the decoherence envelope of the form $\exp\left[-\left(\tau/T_2^{(n)}\right)^p\right]$.
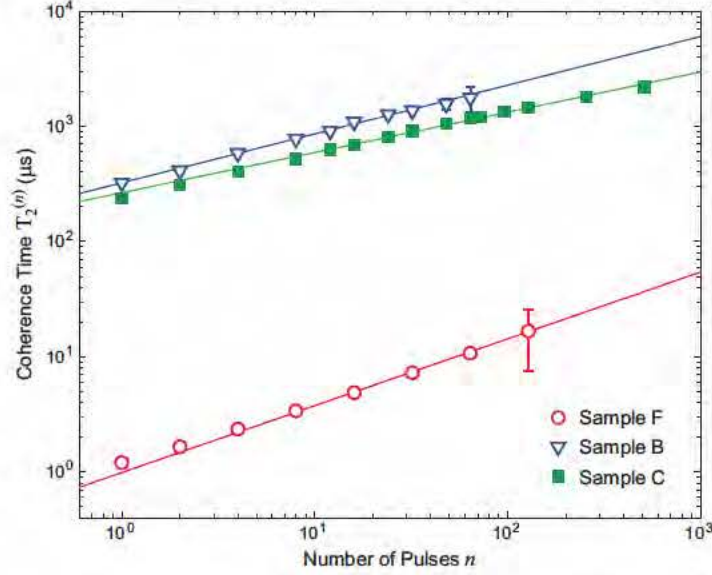
Figure 6.5: Scaling of measured NV ensemble coherence time $T_2^{(n)}$ with number of CPMG pulses n. The solid lines are fit functions from which the scaling power were extracted: $T_2^{(n)} \propto n^s$, where $s = 0.65 \pm 0.02$ for Sample F, $s = 0.42 \pm 0.02$ for Sample B, and $s = 0.35 \pm 0.01$ for Sample C.

Discussion

Note that the spin impurity environments of Samples B and C differ significantly from any diamond samples previously studied with NV dynamical decoupling. For these samples, we observed a power-law dependence of $T_2^{(n)} \propto n^s$ (Figure 6.5), with lower scaling powers than for the nitrogen-rich Sample F: $s = 0.42 \pm 0.02$ for Sample B and $s = 0.35 \pm 0.01$ for Sample C. These sample-dependent scaling powers and the demonstration of similar behavior for NV single-spin and NV ensemble spin decoherence in samples with comparable impurity environments suggest that multipulse dynamical decoupling control sequences can serve as spectral decomposition probes of spin bath dynamics (e.g., the interactions between the ^{13}C and N spin baths [2]). In particular, such studies can provide substantial insight into the effects of environmental inhomogeneity for samples with high NV densities and correspondingly high concentrations of N spin impurities. Such information cannot be extracted from single NV measurements, which require low NV densities to resolve individual NV centers optically. More detail on this spectral decomposition technique as well as some preliminary analysis are presented in Chapter 7.

6.3   Dynamical decoupling at low temperature

At the long ~ 2 ms coherence times achieved using dynamical decoupling techniques at room temperature, the contribution of T_1 processes to decoherence begins to be measurable (see also similar effects in single NV measurements in [91, 71]). In order to extend $T_2^{(n)}$ further and also to explore the relationship between T_1 and $T_2^{(n)}$, we apply the same dynamical decoupling techniques to NV ensembles over a range of temperatures below 300 K.

For these low temperature measurements, we used a fourth sample, Sample E, which is an isotopically pure (0.01% ^{13}C) diamond sample with N density $\sim 1 \times 10^{15}$ cm^{-3} (~ 6 ppb) and NV density $\sim 3 \times 10^{12}$ cm^{-3} (~ 0.02 ppb). The sample was mounted in a cryostat with no magnetic shielding (see Appendix B.3 for details) and NV measurements were performed on a detection volume $\sim 30 \ \mu$m^3 (~ 100 NV centers).

6.3.1   Results

Figure 6.6 shows several example NV ensemble spin coherence decay curves measured from Sample E using CPMG pulse sequences with different numbers of pulses n, at room temperature (300 K) and low temperature (160 K). We extracted $T_2^{(n)}$ from each decoherence curve and found that for both temperatures, $T_2^{(n)}$ increases with the number of pulses in the CPMG sequence, limited to approximately half of T_1: at 300 K, $T_2^{\text{max}} = 3.3 \pm 0.4$ ms and $T_1 = 6.0 \pm 0.4$ ms; and at 160 K, $T_2^{\text{max}} = 40 \pm 8$ ms and $T_1 = 77 \pm 5$ ms.

Figure 6.7 summarizes the dependence of $T_2^{(n)}$ on the number of CPMG pulses n for several temperatures ranging from liquid nitrogen temperature (77 K) to room temperature (300 K). Notably, at liquid nitrogen temperature, an 8192-pulse CPMG sequence achieved a coherence time of $T_2^{(n)} \approx 580$ ms, which is more than two orders of magnitude longer than previous NV coherence time measurements [1, 3]. It also is worthwhile to note that at 160 K, a temperature that can be reached using thermoelectric cooling rather than cryogenic fluids, we found $T_2^{\text{max}} = 40 \pm 8$ ms, which is still an order of magnitude longer than any previous measurement of NV spin coherence time. Thus, combined dynamical decoupling and thermoelectric cooling provides a practical way to significantly increase the NV spin coherence time, which could benefit many applications of NV ensembles where there is some flexibility in the operating temperature, e.g. precision magnetometry [3] and rotation sensing [99, 100].

The T_1 relaxation time measured for each temperature is also indicated in Figure 6.7 (except for 77 K, which had $T_1 > 10$ s). In the figure inset we plot the maximum $T_2^{(n)}$ achieved, T_2^{max}, versus T_1 at each temperature in the interval of $160 - 300$
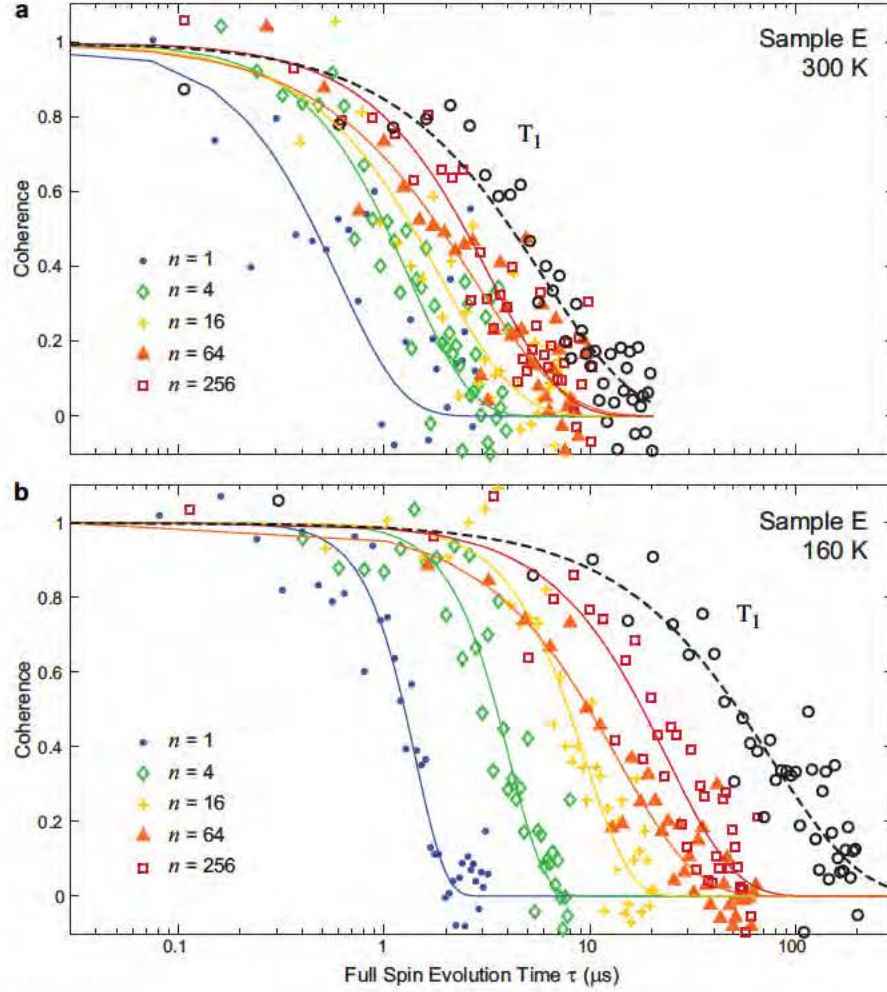
Figure 6.6: Sample E CPMG-n NV spin coherence decay curves (colored data points and solid line fits to data) and longitudinal spin relaxation curves (black data points and dashed line fits to data) at (a) 300 K and (b) 160 K.

K and find $T_2^{max} = (0.53 \pm 0.02)T_1$, which differs starkly from the previously expected $T_2^{(n)}$ limit of $2T_1$ [71]. Under the assumption that spin-phonon coupling only causes spin-lattice relaxation (T_1), one cannot recover the measured $T_2^{max} \approx 0.5T_1$ limit, even taking into account the possibility of unequal relaxation rates between the three ground-state NV spin sublevels. This can be seen by assuming that only state-changing relaxation processes exist and therefore the decoherence rate between two states $|a\rangle$ and $|b\rangle$, γ_2^{ab}, is given by [101]:

$$\gamma_2^{ab} = \frac{1}{2}\left(\sum_{k \neq a} \gamma_1^{a \to k} + \sum_{k \neq b} \gamma_1^{b \to k}\right), \tag{6.1}$$
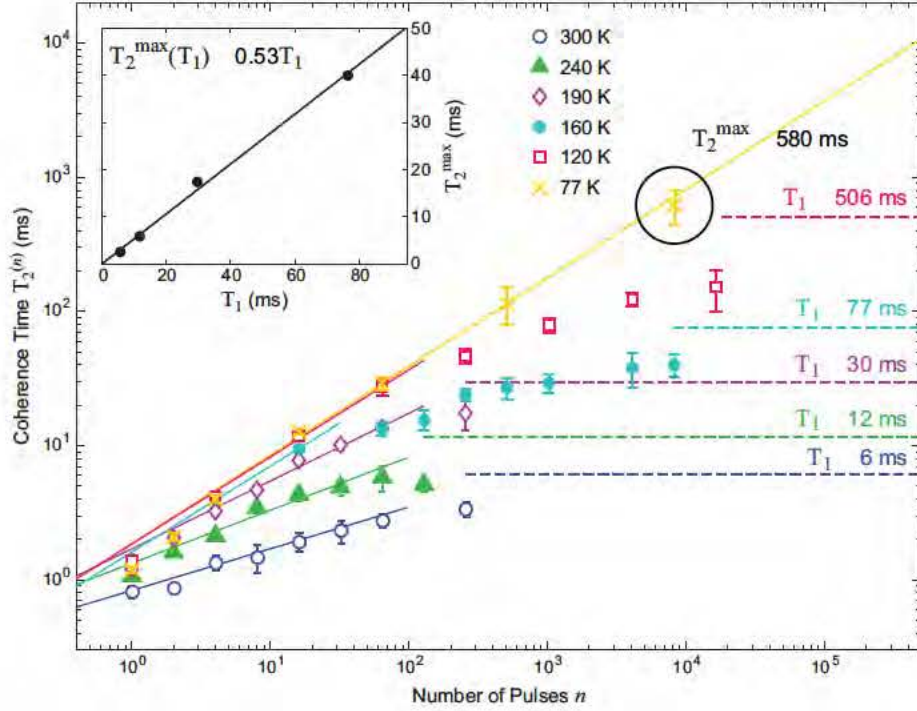
Figure 6.7: NV ensemble spin coherence time as a function of number of CPMG pulses measured from Sample E over a range of temperatures from $77-300$ K. For temperatures above 77 K, the corresponding measured longitudinal relaxation time T_1 is plotted as a dashed line. The black circle indicates the longest $T_2^{(n)} = 580 \pm 210$ ms measured for $n = 8192$ at 77 K. Inset: scaling of the maximum coherence time T_2^{max} as a function of T_1.

where $\gamma_1^{j \to k}$ is the transition rate from state $|j\rangle$ to state $|k\rangle$. Solving rate equations allows one to calculate the measured relaxation rate ($\gamma_1 = 1/T_1$) as a function of these transition rates, and thus compare it to the decoherence rate ($\gamma_2 = 1/T_2$) given by Equation 6.1. (Note that in this discussion, T_2 refers to the general decoherence time rather than the decoherence time associated with a spin echo measurement as is the convention elsewhere in this dissertation.) Through this approach one can show that for a two-level system, at temperatures ranging from zero to infinite temperature, the relation is always $T_2 = 2T_1$. For three or more levels the coefficient changes, but the general statement $T_2 > T_1$ holds (see Appendix C for further details). Therefore we conclude that in our case, since we measure $T_2^{\text{max}} < T_1$, spin-phonon coupling contributes directly and significantly to NV spin decoherence [102]. Such phonon-induced decoherence is generally relevant to any quantum system in which transitions between two levels can be driven by a two-phonon (Raman) process [94], and could play a role in the coherence properties of many other solid-state defects. At lower temperatures, to be studied in future work, spin-spin interactions should dominate
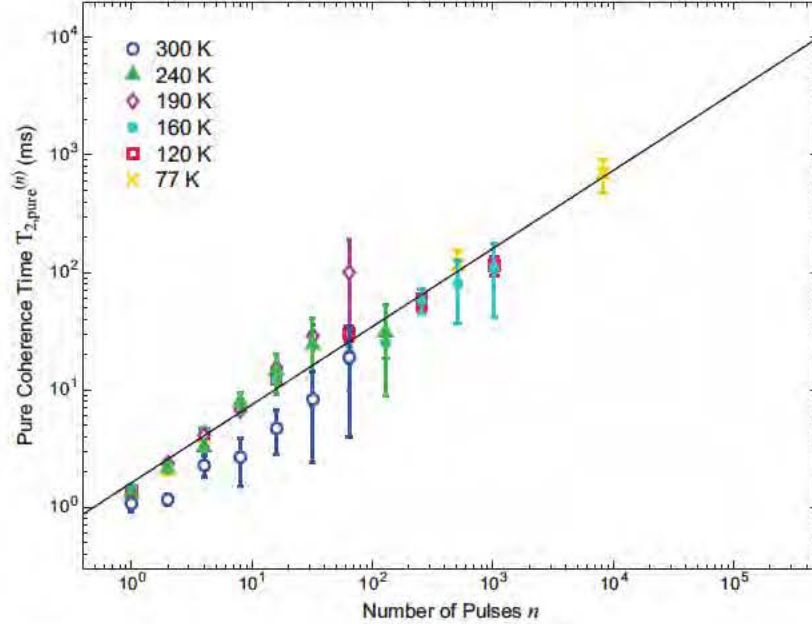
Figure 6.8: "Pure" spin environment induced NV decoherence time as a function of the number of pulses in the CPMG pulse sequence. The data are fit to a power-law function (black line) from which a scaling behavior of $T_{2,\text{pure}}^{(n)} \propto n^{(0.67\pm0.03)}$ is extracted.

both T_1 and $T_2^{(n)}$, and thus we expect T_2^{max} will deviate from the $\approx 0.5 T_1$ limit demonstrated here.

6.3.2 Discussion

$T_2^{(n)}$ vs n scaling

It is evident from Figure 6.7 that the scaling of the coherence time with the number of CPMG pulses varies with temperature. In order to study the scaling behavior of the "pure" spin environment induced decoherence, we subtracted from the measured decoherence rate the temperature dependent phononic rate $1/(0.53 T_1)$ (see inset of Figure 6.7). The corrected coherence time $T_{2,\text{pure}}^{(n)}$ is plotted against the number of CPMG pulses n in Figure 6.8, exhibiting striking universal behavior for all temperatures. We fit the corrected data to a power law scaling, and find $T_{2,\text{pure}}^{(n)} \propto n^{(0.67\pm0.03)}$. This value is consistent with the expected scaling power of $2/3$ for a Lorentzian noise spectrum of an electronic spin bath [2, 103]. It is worthwhile to note that the same analysis may be performed on the previous room temperature CPMG measurements of Samples B and C, which were likely limited by T_1. Extracting the

"pure" coherence time $T_{2,\text{pure}}^{(n)}$ yields corrected scaling powers of $s = 0.59 \pm 0.02$ for Sample B and $s = 0.53 \pm 0.02$ for Sample C, both of which are still less than the $s = 2/3$ limit for a Lorentzian noise spectrum. This behavior is addressed in more detail in Chapter 7.

Measurements on other samples

Even though our measurements were performed on an isotopically pure sample (0.01% ^{13}C), we expect that similar results can be obtained for natural abundance diamond (1.1% ^{13}C), since the dynamical decoupling sequences we employ are also effective in suppressing dephasing caused by the nuclear spin bath [91, 3]. However, as discussed in Chapter 3, special care must be taken in aligning the applied static magnetic field along the NV axis for natural abundance diamond to avoid additional NV spin decoherence caused by variations in the effective Larmor frequency of nearby ^{13}C nuclear spins due to magnetic field misalignment [86, 77].

At present we have performed measurements on one additional sample, the isotopically pure (0.01% ^{13}C) Sample C. Due to the higher N density of the sample, the coherence times achieved were consistently lower. At 77 K with $n = 4096$ pulses, we obtained a coherence time of $T_2^{(n)} = 50 \pm 9$ ms, with a scaling of the coherence time with the number of pulses of $T_2^{(n)} \propto n^{(0.54\pm0.01)}$, which is consistent with the $s = 0.53 \pm 0.02$ corrected scaling power determined by removing T_1 relaxation effects from the room temperature CPMG NV coherence measurements. From this reproducibility and the ensemble nature of our experiments, we conclude that the data presents the behavior of typical NV centers, averaged over inhomogeneous broadening effects such as strain.

Pulse errors

The CPMG pulse sequence is quite robust against noise (e.g. external magnetic field fluctuations) and pulse errors, allowing us to apply thousands of pulses. However, we noticed a modest reduction in signal contrast and increased noise for pulse sequences of $\sim 10,000$ pulses or more (Figure 6.9). The resulting reduction in signal-to-noise, together with the long integration times needed, currently prevents us from increasing the coherence time to beyond ~ 0.6 s. In future work we will address these issues using various approaches, including more robust composite pulses [104] that could be better suited to manipulate an inhomogeneously broadened ensemble.
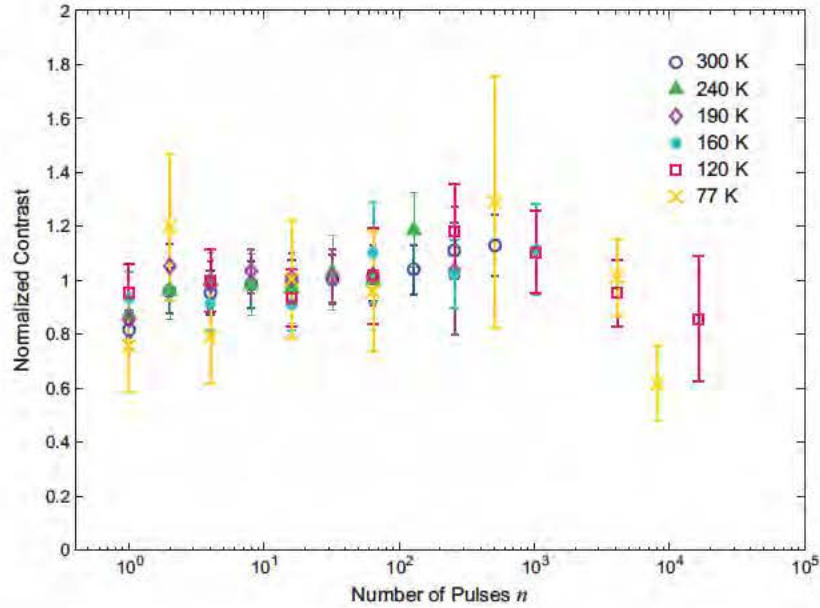
Figure 6.9: Measured normalized signal contrast as a function of the number of CPMG pulses n for different temperatures.

Outlook

Achieving long NV spin coherence times in diamond samples with high impurity concentration (~ 1 ppm) is a crucial step toward creating nonclassical states of NV ensembles. Such non-classical states could form the basis for high-sensitivity quantum metrology, potentially allowing significantly improved sensitivity and bandwidth [105, 106], and could also serve as a resource for quantum information protocols. To observe significant entanglement between neighboring NV centers, their decoherence rate must be small compared to the frequency associated with their interaction. For a realistic diamond sample with N ~ 1 ppm and NV ~ 10 ppb, coherence times larger than ~ 50 ms are needed for significant entanglement, which is within reach given the results presented here. For example, collective spin squeezing using L_z^2 one-axis squeezing techniques [107] could be created through application of pulse sequences that average out the x, y components of the spin-spin dipolar coupling [108]. Such pulse sequences can be straightforwardly applied in conjunction with the CPMG pulse sequences used here for extending the NV spin coherence time.

6.4 Multipulse magnetometry

Now we take advantage of the extension in NV ensemble spin coherence time achieved by multipulse dynamical decoupling sequences to demonstrate up to an or-

der of magnitude enhancement in AC magnetic field sensitivity. These preliminary measurements were performed at room temperature and were subsequently limited by the millisecond time scale of NV spin relaxation; however, the multipulse magnetometry technique can be easily performed at lower temperatures to further improve magnetic sensitivity.

6.4.1   Sensitivity analysis

Recall, in a standard AC magnetometry measurement utilizing a spin echo sequence, an oscillating magnetic field, $b(t) = B \sin\left[(2\pi/\tau_{\mathrm{ac}})\, t + \varphi_0\right]$, induces a net phase accumulation of the NV spin coherence, which is maximized when the full time of the spin echo sequence is equivalent to the period of the AC magnetic field (τ_{ac}) and the phase offset φ_0 is such that the control pulses coincide with nodes in the magnetic field [Figure 6.1(a)]. Under these conditions, the field amplitude B can be extracted from the measurement of accumulated NV spin phase with optimum sensitivity normalized per unit time, given approximately by [52]:

$$\eta_{\mathrm{se}} \approx \frac{\pi\hbar}{2\mathrm{g}\mu_{\mathrm{B}}} \frac{1}{\alpha_0\sqrt{\beta\tau_{\mathrm{ac}}}} \exp\left[\left(\frac{\tau_{\mathrm{ac}}}{\mathrm{T}_2}\right)^p\right]. \tag{6.2}$$

As before, the number of photons collected per measurement β is dependent on the optical collection efficiency and number of NV spins contributing to the measurement. The initial contrast α_0 is modified by NV decoherence T_2 over the course of the spin echo measurement, described phenomenologically by an exponential factor with power p. The value of p is found to be sample dependent, in the range of 1 to 3, and is related to the dynamics of the spin environment and to ensemble inhomogeneous broadening [2] (see Chapter 7).

In AC magnetometry measurements which employ n-pulse dynamical decoupling sequences, the sensitivity is given approximately by Equation 6.2 with two modifications: the measurement time is increased ($\tau_{\mathrm{ac}} \to \frac{n}{2}\tau_{\mathrm{ac}}$) and the NV ensemble spin coherence time is extended ($\mathrm{T}_2 \to \mathrm{T}_2^{(n)} = \mathrm{T}_2 n^s$). The resulting sensitivity is given by:

$$\eta_{(n)} \approx \frac{\pi\hbar}{2\mathrm{g}\mu_{\mathrm{B}}} \frac{1}{\alpha_0\sqrt{\beta\frac{n}{2}\tau_{\mathrm{ac}}}} \exp\left[\left(\frac{n^{(1-s)}\tau_{\mathrm{ac}}}{2\mathrm{T}_2}\right)^p\right]. \tag{6.3}$$

Because the measurement time increases linearly with the number of control pulses n, whereas the coherence time increases sub-linearly, there is an optimum number of pulses n_{opt} that yields the most sensitive measurement of an AC magnetic field of period τ_{ac} given a set of sample-determined parameters:

$$n_{\mathrm{opt}} = \left[\frac{1}{2p(1-s)}\left(\frac{2\mathrm{T}_2}{\tau_{\mathrm{ac}}}\right)^p\right]^{\frac{1}{p(1-s)}}. \tag{6.4}$$

For a given sample, all the parameters except τ_{ac} are fixed and we can simplify Equation 6.4 to $n_{opt} \propto (1/\tau_{ac})^{\frac{1}{(1-s)}}$. From this relationship, we see that at higher AC frequencies, more pulses are needed to reach the optimum sensitivity, which can be understood intuitively by realizing that the high frequency regime corresponds to short time intervals between control pulses during which time there is very little contrast lost due to decoherence ($\tau_{ac} \ll T_2$). More pulses increase the sensitivity by allowing for a longer measurement time and subsequently more phase accumulation per measurement. This intuition also illustrates why multipulse sequences are more effective at enhancing magnetometry sensitivity in the high frequency regime, where the spin echo scheme provides relatively poor magnetic field sensitivity (Figure 6.12). As discussed in the previous section, extension of the NV ensemble spin coherence time via multipulse dynamical decoupling (and thus enhancement of magnetic field sensitivity) is eventually limited by NV spin-lattice relaxation (T_1), beyond which increasing the number of control pulses is ineffective. In applications where it is compatible, however, a modest amount of cooling can be applied to further improve magnetic field sensitivity.

6.4.2 Results

We used Sample C mounted in the wide-field fluorescence microscope setup to perform NV ensemble magnetometry measurements comparing spin echo and multipulse dynamical decoupling schemes. The detection volume was approximately $30\,\mu\mathrm{m}^3$, corresponding to $\sim 10^3$ sensing NV centers aligned along the static magnetic field. We employed n-pulse XY sequences to provide more isotropic compensation for pulse errors [96]. Note that though Sample C is an isotopically engineered sample with 0.01% ^{13}C, such pulse sequences are equally applicable for samples with a natural abundance of ^{13}C with the additional complication that the period of the AC field to be measured must correspond to a ^{13}C revival in the NV spin decoherence curve.

Figure 6.10 shows magnetometry curves of the measured NV fluorescence as a function of applied AC magnetic field amplitude for spin echo, 28-pulse, and 54-pulse sequences in order to illustrate how the magnetic field sensitivity improves with multipulse sequences compared to a spin echo sequence. In essence, the larger NV spin phase accumulation achieved per measurement in the multipulse scheme increases the maximum slope $\frac{\partial \mathcal{S}}{\partial B}$ of the magnetometry curve such that the same fluctuation in signal $\delta\mathcal{S}$ corresponds to a smaller uncertainty in the magnetic field δB. The AC magnetic field sensitivity improved with the number of pulses n, in good agreement with predicted values up to $n \approx 150$ pulses, at which point pulse errors began to degrade the measured sensitivity (Figure 6.11). While for the present measurements the AC magnetic field consisted of a locked, single frequency component, the procedure can be extended to finite-bandwidth fields [64].
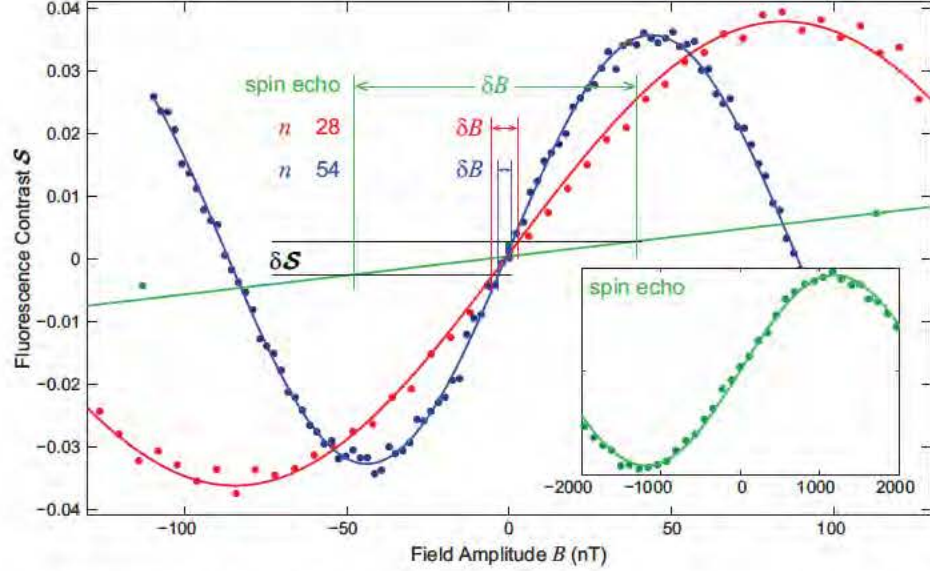
Figure 6.10: Examples of measured normalized fluorescence signals as functions of AC field magnitude B using a spin echo sequence (green) (wider amplitude range shown in the inset) and multipulse XY sequences with 28 (red) and 54 (blue) control pulses, illustrating how the uncertainty in the measured signal (δS) limits the uncertainty in the extracted magnetic field magnitude (δB). The sine behavior of the signal with respect to b_{ac} is achieved by shifting the phase of the last microwave pulse by $90°$ from what is shown in Figure 6.1(c).

Over a wide range of AC magnetic field frequencies our NV ensemble magnetometry measurements confirmed that multipulse dynamical decoupling outperformed the spin echo scheme, in agreement with theoretical expectations (Figure 6.12). The enhancement in magnetic field sensitivity provided by multipulse dynamical decoupling was especially pronounced at frequencies higher than the spin echo $1/T_2$ coherence. For example, at a frequency of 220 kHz, we measured a factor of 10 improvement in magnetic field sensitivity: from $\eta_{se} = 67.7 \pm 3.5\,\mathrm{nT}/\sqrt{\mathrm{Hz}}$ using a spin echo sequence, to $\eta_{(n)} = 6.8 \pm 0.4\,\mathrm{nT}/\sqrt{\mathrm{Hz}}$ using a 240-pulse XY sequence.

6.5 Summary

In summary, we experimentally demonstrated that multipulse dynamical decoupling control sequences can significantly improve NV ensemble spin coherence times and enhance NV magnetic sensitivity to AC fields. At room temperature, we observed order of magnitude coherence time extension in samples with widely differing
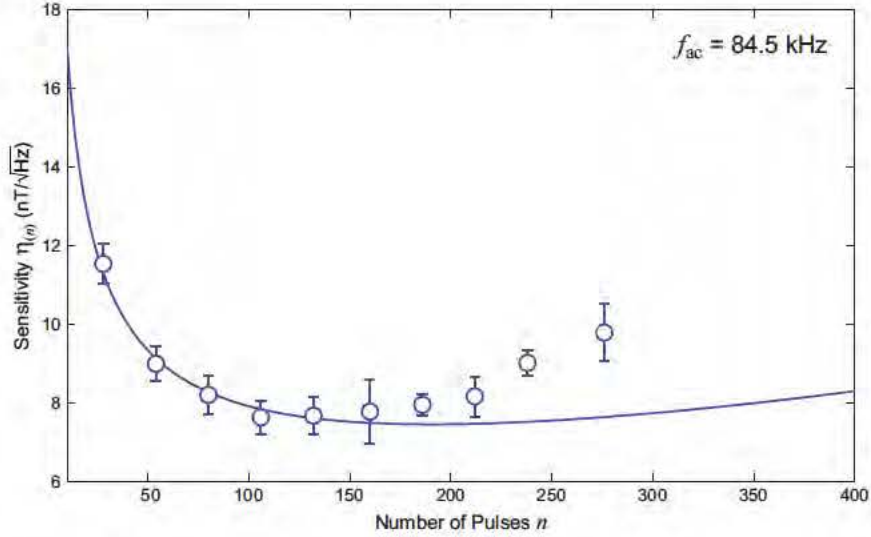
Figure 6.11: Measured multipulse magnetic field sensitivity as a function of number of pulses for an 84.5 kHz AC field (circles). The solid line is calculated using Equation 6.3 with experimental parameters $\alpha_0 = 0.055$, $\beta = 3.4$ photons per measurement, $T_2 = 250 \, \mu s$, $p = 1$, and $s = 0.37$.

NV densities and spin impurity environments. For these spin environments that differ from those studied previously, we found significantly different scaling of the NV ensemble spin coherence time with the number of pulses in the control sequence. These results provide insight into spin bath dynamics and could guide future applications in multi-spin quantum information processing and metrology.

By measuring at lower temperatures, we demonstrated more than two orders of magnitude further improvement in the NV coherence time: up to $T_2 \sim 0.6$ s by combining dynamical decoupling control sequences with cryogenic cooling to 77 K; and $T_2 \sim 40$ ms for temperatures achievable via thermoelectric cooling (> 160 K). By studying the dependence of coherence time $T_2^{(n)}$ and spin relaxation time T_1 on temperature, we identified an effective limit of $T_2^{max} \approx 0.5 T_1$, which we attribute to phonon-induced decoherence. Given this limit, we expect that for low NV densities T_2 on the order of a few seconds should be achievable at liquid nitrogen temperatures.

We also showed that multipulse dynamical decoupling improves NV ensemble AC magnetic field sensitivity relative to the spin echo scheme, with a ten-fold enhancement for higher frequency fields at room temperatures, with greater enhancement expected at lower temperatures. Using samples with higher NV densities could further improve this sensitivity; however, at high NV concentrations ($\gtrsim 1$ ppb), the coherence time may be limited by NV NV interactions, since CPMG pulse sequences affect both the NV spin and its NV spin bath at the same time, which cancels the decoupling effect. Other techniques, such as WAHUHA and MREV pulse sequences [109, 110],
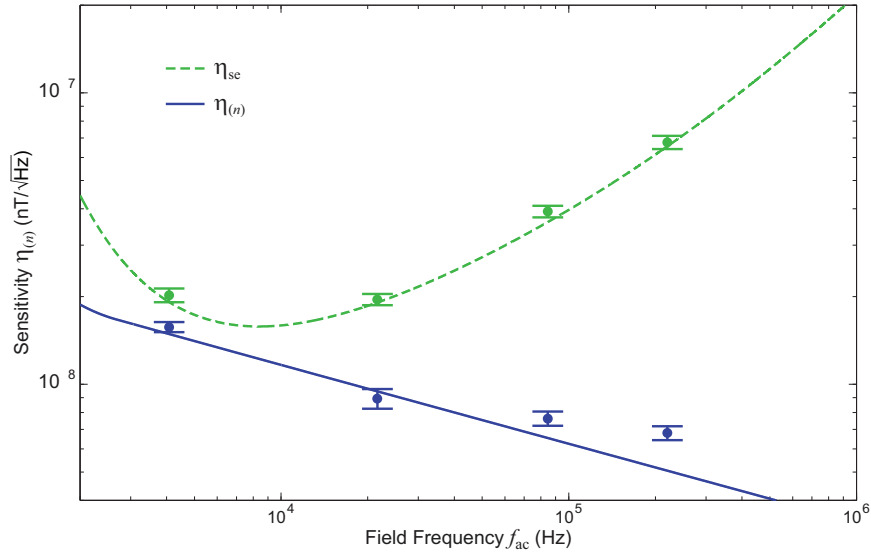
Figure 6.12: Comparison of calculated (lines) and measured (points) magnetic field sensitivity at several AC field frequencies, for spin echo and multipulse XY sequences (using the measured optimum number of pulses for each frequency).

may be applied to address this issue.

The greatly extended NV spin coherence time presented in this work, which does not require an optimally chosen NV center, could also form the building block for wide-ranging applications in quantum information, sensing, and metrology in the solid-state [111, 65]. In particular, the fact that such long coherence times can be achieved with high-density NV ensembles suggests that spin squeezing and highly entangled states can be created, since $T_2 > NV$ NV dipolar interaction time. Finally, this work could provide a key step toward realizing interaction-dominated topological quantum phases in the solid-state, as well as a large family of driven many-body quantum Hamiltonians [112].

Chapter 7

Spectral Decomposition

In the previous chapter, we applied dynamical decoupling techniques to NV ensembles in several diamond samples with different spin impurity environments. In each sample, the multipulse control sequences were able to significantly extend the NV ensemble spin coherence time; however, we noted that the scaling of the coherence time as a function of the number of pulses varied from sample to sample. These observed variations suggest that the application of these pulse sequences to extract information about the spectral function of the bath may reveal sample-dependent spin bath dynamics.

In this chapter, we employ these pulse sequences as a general spectral decomposition technique [113], which has previously been demonstrated in other spin systems [114, 115], to characterize the dynamics of the composite spin bath which makes up the NV spin environment, consisting of both electronic spin (N) and nuclear spin (^{13}C) impurities. We study three diamond samples with a range of NV densities and impurity spin concentrations (measuring both NV ensembles and single NV centers) and find unexpectedly slow dynamics for the electronic spin baths in two diamond samples with natural abundance (1.1%) of ^{13}C nuclear spin impurities. We identify a possible new mechanism in diamond involving an interaction between the electronic and nuclear spin baths that can explain the observed suppression of electronic spin bath dynamics. Gaining a better understanding of the sources of NV spin decoherence and their interplay by using techniques such as spectral decomposition will inform the optimization of future samples for magnetic sensing.

7.1 Background

7.1.1 Spectral decomposition technique

Due to coupling of spins (here, NV electronic spins) to their magnetic environment, coherence is lost over time with the general form $C(t) = e^{-\chi(t)}$, where the functional $\chi(t)$ describes the time dependence of the decoherence process. In the presence of a modulation acting on the NV spins (e.g., a resonant MW pulse sequence), described by a filter function in the frequency domain $F_t(\omega)$, the decoherence functional is given by [116, 117]:

$$\chi(t) = \frac{1}{\pi} \int_0^\infty d\omega S(\omega) \frac{F_t(\omega)}{\omega^2}, \tag{7.1}$$

where $S(\omega)$ is the spectral function describing the coupling of the system to the environment. Equation 7.1 holds in the approximation of weak coupling of the NV spins to the environment, which is appropriate for systems with (dominantly) electronic spin baths [118]. Thus, we restrict our measurements in this work to samples that meet this criterion of nitrogen-dominated spin baths.

$S(\omega)$ can be determined from straightforward decoherence measurements of the NV spin using a spectral decomposition technique [115, 114, 113]. As seen from Equation 7.1, if an appropriate modulation is applied to the NV spins such that

$$\frac{F_t(\omega)}{\omega^2 t} = \delta(\omega - \omega_0) \tag{7.2}$$

then

$$\chi(t) = \frac{1}{\pi} t S(\omega_0). \tag{7.3}$$

Therefore, by measuring the time dependence of the spin coherence $C(t)$ when subjected to such a spectral δ-function modulation, we can extract the spin bath's spectral component at frequency ω_0:

$$S(\omega_0) = -\pi \ln(C(t))/t. \tag{7.4}$$

This procedure can then be repeated for different values of ω_0 to provide complete spectral decomposition of the spin environment.

A close approximation to the ideal spectral filter function $F_t(\omega)$ described above can be provided by the CPMG pulse sequence for dynamical decoupling of a spin from its environment [93]. Recall, the CPMG pulse sequence is an extension of the spin echo sequence [119], with n equally spaced π pulses applied to the system after initially rotating it into the x axis with a $\pi/2$-pulse. We apply a deconvolution procedure to correct for deviations of this filter function from the ideal Dirac δ-function.
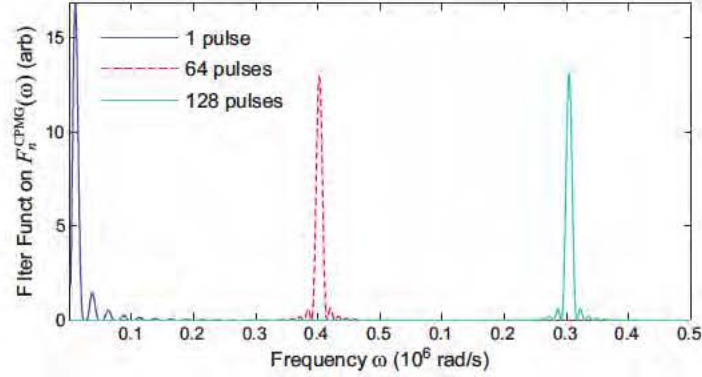
Figure 7.1: CPMG filter functions. Calculated filter function $F_n^{\mathrm{CPMG}}(\omega)$ for three examples of CPMG-n pulse sequences (for $n = 1, 64, 128$).

7.1.2 Spectral decomposition deconvolution procedure

The coherence of a two-level quantum system can be related to the magnitude of the off-diagonal elements of the system's density matrix. Specifically, we deal here with NV electronic spins in a finite external magnetic field, which can be treated as effective two-level spin systems with quantization (z) axis aligned with the NV axis. When the NV spins are placed into a coherent superposition of spin eigenstates (e.g., aligned with the x axis of the Bloch sphere) the measurable spin coherence is given by $C(t) = \mathrm{Tr}[\rho(t)S_x]$.

The filter function for the n-pulse CPMG control sequence $F_n^{\mathrm{CPMG}}(\omega)$ covers a narrow frequency region (with a width given by π/t, where t is total length of the sequence) which is centered at $\omega_0 = \pi n/t$, and is given by [120]:

$$F_n^{\mathrm{CPMG}}(\omega t) = 8\sin^2\left(\frac{\omega t}{2}\right)\frac{\sin^4\left(\frac{\omega t}{4n}\right)}{\cos^2\left(\frac{\omega t}{2n}\right)}. \tag{7.5}$$

We note that the narrow-band feature of the CPMG filter essentially defines the effectiveness of this sequence for dynamical decoupling.

The filter function $F_n^{\mathrm{CPMG}}(\omega t)$ associated with the CPMG-n pulse sequence deviates from a δ-function by the finite width of the main spectral peak and by the presence of higher harmonics (see Figure 7.1). In addition, the central frequency of the filter function changes with the duration of the experiment and with the number of pulses. Therefore, reconstructing the spin bath spectral function $S(\omega)$ from the decoherence data requires a solution of a Fredholm type equation to extract $S(\omega)$ (Equation 7.1):

$$\chi(t) = \frac{1}{\pi}\int_0^\infty d\omega S(\omega)\frac{F_t(\omega)}{\omega^2}. \tag{7.6}$$

This extraction is accomplished by assuming that the spectral function decays to zero at high frequency and by noting that the filter function includes high harmonics but negligible low frequency artifacts. Thus, the procedure starts at the high frequency values of $\chi(\omega)$, and works back to lower frequencies by subtracting the effect of higher harmonics using the reconstructed high frequency values of $S(\omega)$ and the analytical form of the filter function.

Due to the high frequency components of the filter function and the monotonically decreasing nature of the spectral function, a naive reconstruction of the spectral function assuming a δ-function form of the filter function produces results that are biased to lower values by $\sim 15\%$. This bias is removed using the reconstruction algorithm presented above.

7.1.3 Spectral function of a spin bath

The composite spin environment in diamond is dominated by a bath of fluctuating N electronic spin impurities, which causes decoherence of the probed NV electronic spins through magnetic dipolar interactions. In the regime of low external magnetic fields and temperatures well above the Zeeman energy of the N electronic spins (relevant to the present experiments), the N bath spins are randomly oriented, and their flip-flops (spin state exchanges) can be considered as random uncorrelated events [118]. Therefore, the resulting spectrum of the N bath's coupling to the NV spins can be assumed to be Lorentzian [116]:

$$S(\omega) = \frac{\Delta^2 \tau_c}{\pi} \frac{1}{1 + (\omega \tau_c)^2}. \qquad (7.7)$$

This spin bath spectrum is characterized by two parameters: Δ is the average coupling strength of the N bath to the probed NV spins, and τ_c is the correlation time of the N bath spins with each other, which is related to their characteristic flip-flop time. In general, the coupling strength Δ is given by the average dipolar interaction energy between the bath spins and the NV spins, and the correlation time τ_c is given by the inverse of the dipolar interaction energy between neighboring bath-spins. Since such spin-spin interactions scale as $1/r^3$, where r is the distance between spins, it is expected that the coupling strength scales as the N bath spin density n_N (i.e., $\Delta \propto n_N$), and the correlation time scales as the inverse of this density (i.e., $\tau_c \propto 1/n_N$).

Also recall from Chapter 6 that the multipulse CPMG sequence used in the spectral decomposition technique extends the NV spin coherence lifetime by suppressing the time-averaged coupling to the fluctuating spin environment. In general, the coherence lifetime $T_2^{(n)}$ increases with the number of pulses n employed in the CPMG sequence. For a Lorentzian bath, in the limit of very short correlation times

$(\tau_c \ll T_2)$, the sequence is inefficient and $T_2^{(n)} \propto n^0$ (no improvement with number of pulses). In the opposite limit of very long correlation times $(\tau_c \gg T_2)$, the scaling is $T_2^{(n)} \propto n^{2/3}$ [53, 103, 64] (see also recent work on quantum dots [121]). In the following we apply spectral decomposition to study the spin bath dynamics and resulting scaling of $T_2^{(n)}$ with n for NV centers in diamond.

7.2 Results

We applied the spectral decomposition technique to extract the spin bath parameters Δ and τ_c for three diamond samples with differing concentrations of electronic and nuclear spin impurities. We first study Sample C, which has a very low concentration of ^{13}C nuclear spin impurities (0.01%), a moderate concentration of N electronic spin impurities (~ 1 ppm), and a moderate NV density (~ 0.6 ppb) with spin echo coherence time $T_2 \approx 250 \,\mu$s. Recall from Chapter 6 that even for few numbers of pulses, phononic relaxation likely contributes strongly to the NV spin decoherence of this sample at room temperature. As a result, we perform measurements on Sample C at liquid nitrogen temperature in a cryostat setup (see Appendix B.3 for details).

We then employed a wide-field CCD setup (see Appendix B.1 for details) to measure Sample F, a CVD diamond sample with a $\sim 10 \,\mu$m thick N-doped layer containing natural ^{13}C concentration (1.1%), high N concentration (~ 100 ppm), and large NV density (~ 0.1 ppm). Finally, we study Sample G, a type 1b HPHT diamond containing natural ^{13}C concentration, high N concentration (~ 50 ppm), and low NV density (~ 0.01 ppb). Due to its low NV density, we studied Sample G using a confocal microscope able to measure single NV centers (see Appendix B.2 for details). Note that measurements on Samples F and G were performed at room temperature because both samples had short NV spin coherence times which were not limited by longitudinal spin relaxation even with large numbers of pulses.

We use two methods of analysis to characterize the underlying spin bath spectrum $S(\omega)$ in terms of the coupling strength Δ of the bath spins to the probed NV spins and the correlation time τ_c of the bath spins with each other: in the first we separately fit each spectral function $S_n(\omega)$ to a Lorentzian, which provides individual-fit values for Δ and τ_c for each of the CPMG-n pulse sequences, and in the second we average all the $S_n(\omega)$ values for each ω and then fit the resulting mean spectral function $\langle S_n(\omega) \rangle_n$ to a Lorentzian, which provides single, average-fit values for Δ and τ_c.

7.2.1 Sample C

We first discuss the results for ^{12}C isotopically enriched sample. Figure 7.2 plots examples of the measured NV ensemble spin coherence decay $C_n(t)$ as a function
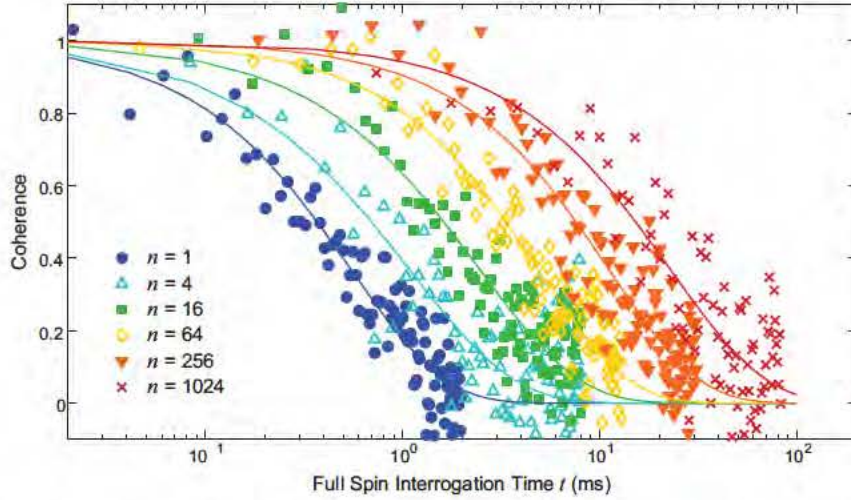
Figure 7.2: Examples of NV ensemble spin coherence as a function of time $C_n(t)$ measured at 77 K for CPMG pulse sequences with different numbers of pulses n.

of pulse sequence duration t for CPMG pulse sequences with different numbers of π pulses n. The measured $C_n(t)$ are well described by a stretched exponential $e^{-(t/\mathrm{T_2}^{(n)})^p}$, where the value of p varies between 1 and 3 related to dynamics of the spin environment and ensemble inhomogeneous broadening. This behavior is consistent with a Lorentzian spin bath spectrum and indicates that N spin impurities are the dominant source of NV spin decoherence. Note that the second most important electronic spin impurities are NVH defects, which are an order of magnitude less abundant than N impurities [8]. The contribution of instantaneous spin diffusion due to interactions between neighboring NV spins and MW-induced spin flips [122] is also negligible, as the NV Rabi frequency for typical MW power (~ 10 MHz) is large compared to the NV electronic spin transition linewidth (~ 3 MHz), and the NV dipolar coupling time scale (proportional to the inverse of the dipolar coupling energy) is at least an order of magnitude longer than the longest measured NV spin coherence time.

Using the measured $C_n(t)$ data we derive values for the spin bath spectral function $S_n(\omega)$ for each CPMG pulse sequence by deconvolving $\chi_n(\omega)$ with the filter function $F_n^{\mathrm{CPMG}}(\omega t)$. The resulting values for the spectral functions $S_n(\omega)$ for all CPMG pulse sequences (i.e., all values of n) are plotted together in Figure 7.3. Note that the average data (red crosses) in Figure 7.3 are calculated by binning the full data set for $S_n(\omega)$ into 100 frequency values between 0 and 1 MHz.

We then extracted the best-fit Lorentzian spin bath spectrum (fit to the average of all data points), yielding a coupling strength of $\Delta = 12 \pm 1$ kHz and correlation time $\tau_\mathrm{c} = 52 \pm 11$ μs, which agrees reasonably with the range of values we find for the
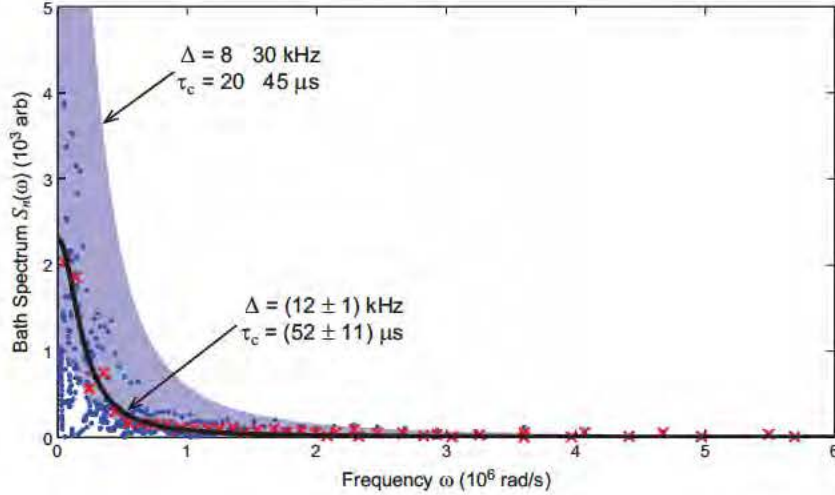
Figure 7.3: Application of the spectral decomposition technique to Sample F. Derived values for the spin bath spectral functions $S_n(\omega)$ for all CPMG pulse sequences (blue dots) and binned average values (red crosses). Each blue dot represents a pulse sequence with a specific duration t and number of pulses n, such that the probed frequency is $\omega = \pi n/t$. Also shown is the best fit Lorentzian for the mean spectral function $\langle S_n(\omega) \rangle_n$ (solid black line), and a range of best-fit Lorentzians for the individual spectral functions $S_n(\omega)$ for each CPMG pulse sequence (light blue band).

Lorentzian spin bath spectra $S_n(\omega)$ fit to each CPMG pulse sequence individually, $\Delta \simeq 8 - 30$ kHz and $\tau_c \simeq 20 - 45$ μs. These values are in reasonable agreement with the expected "N dominated bath" values for Δ and τ_c for this sample's estimated concentrations of ^{13}C and N spins (see Table 7.1), indicating that N electronic spin impurities are the dominant source of NV decoherence. In Figure 7.4 we plot the NV ensemble spin coherence lifetime $T_2^{(n)}$ as a function of the number n of CPMG π pulses. We found that the scaling behavior extracted from measurements of the coherence decay $C_n(t)$ and synthesized from the average-fit Lorentzian spin bath spectrum with $\Delta = 12$ kHz, $\tau_c = 52$ μs are in reasonable agreement.

7.2.2 Samples F and G

We repeated the spectral decomposition analysis for the two other diamond samples, with the results for all three samples summarized in Figure 7.5 and Table 7.1. We find reasonable agreement between the measured and expected values for the NV spin bath coupling strength Δ in all three diamond samples, with Δ scaling approximately linearly with the N concentration. As mentioned before, the measured and expected values for the spin bath correlation time τ_c agree reasonably well (within
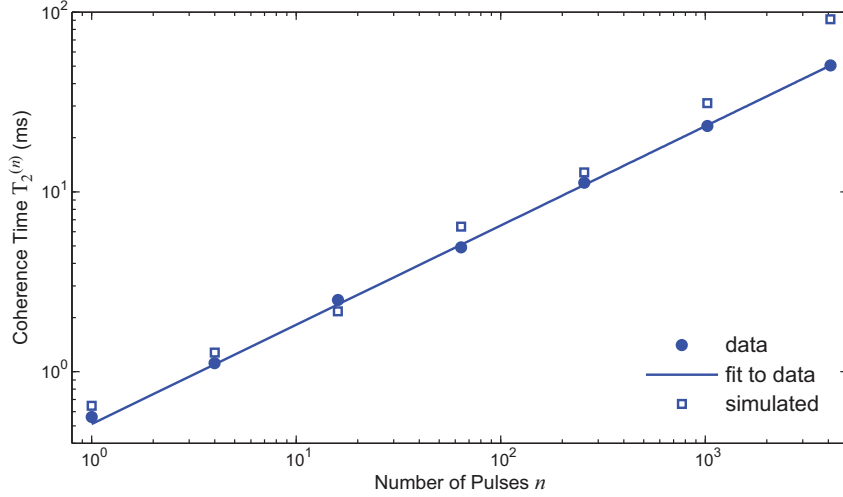
Figure 7.4: Scaling of $T_2^{(n)}$ with the number n of CPMG pulses: derived from NV spin coherence decay data $C_n(t)$ (dots); fit of dots to a power law $T_2^{(n)} = (0.54 \pm 0.02 \text{ ms})n^{(0.54\pm0.01)}$ (solid line); and synthesized from the average-fit Lorentzian spin bath spectrum with $\Delta = 12$ kHz, $\tau_c = 52$ μs (open squares), which yields a consistent fit $T_2^{(n)} = (0.54 \pm 0.08 \text{ ms})n^{(0.59\pm0.03)}$.

a factor of ~ 3) for Sample C. However, we find a striking discrepancy between the measured and expected values of τ_c for the two samples with 1.1% ^{13}C concentration (Samples F and G): both samples have measured spin bath correlation times that are more than an order of magnitude longer than that given by the simple electronic spin bath model, though the relative values of τ_c for these two samples scale inversely with N concentration, as expected.

7.3 Discussion

7.3.1 Spin bath suppression

We explain the observed suppression of spin bath dynamics as a result of random, relative detuning of electronic spin energy levels due to interactions between proximal electronic (N) and nuclear (^{13}C) spin impurities (similar to processes identified by Bloembergen [123] and Portis [124] for other solid-state spin systems). The ensemble average effect of such random electronic-nuclear spin interactions is to induce an inhomogeneous broadening ΔE of the resonant electronic spin transitions in the bath, which reduces the electronic spin flip-flop rate R ($\sim 1/\tau_c$) given by [125, 126]

$$R \simeq \frac{\pi}{9} \frac{\Delta_N^2}{\Delta E}, \tag{7.8}$$
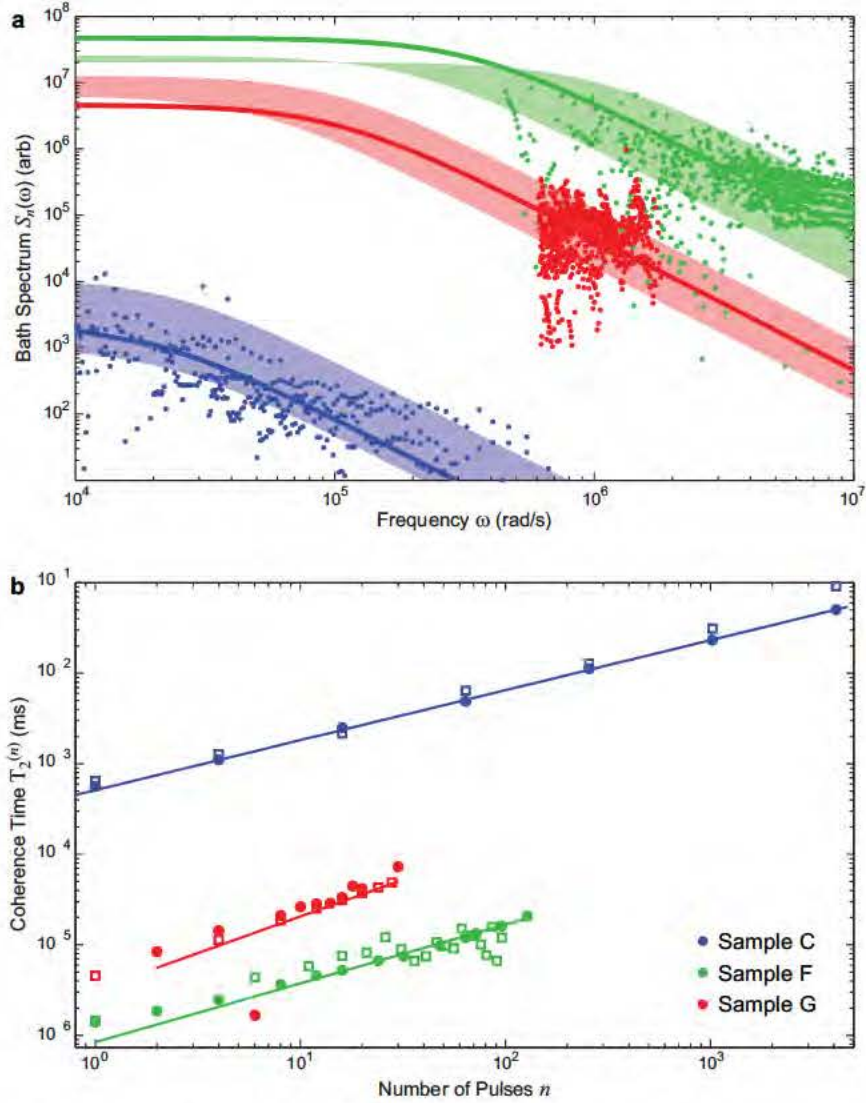
Figure 7.5: Comparison of spectral decomposition results from Samples C (blue), F (green) and G (red). (a) Spin bath spectral functions data for all CPMG pulse sequences (dots), and associated Lorentzian fits using the average-fit method (solid lines) and the individual-fit method (color bands). (b) Scaling of $T_2^{(n)}$ with the number of CPMG pulses n as extracted from NV spin coherence decay data $C_n(t)$ (dots) and as synthesized from the average-fit Lorentzian spin bath spectrum (open squares). The solid lines are power-law fits to the data with scaling powers: $T_2^{(n)} \propto n^{(0.54\pm0.01)}$ for Sample C, $T_2^{(n)} \propto n^{(0.65\pm0.05)}$ for Sample F, $T_2^{(n)} \propto n^{(0.7+0.1)}$ for Sample G.

Chapter 7: Spectral Decomposition

Table 7.1: Comparison of key characteristics and extracted "average-fit" Lorentzian spin bath parameters for the samples studied in this work.

	Sample C	Sample F	Sample G
Meas. technique	ensemble (77K)	ensemble	single NV
N concentration	~ 1 ppm	~ 100 ppm	~ 50 ppm
NV density	~ 0.6 ppb	~ 0.1 ppm	~ 0.01 ppb
^{13}C concentration	0.01%	1.1%	1.1%
Spin echo T_2	(520 ± 20) μs	(2 ± 1) μs	(5 ± 1) μs
$T_2^{(n)}$ scaling	$n^{(0.54 \pm 0.01)}$	$n^{(0.65 \pm 0.05)}$	$n^{(0.7 \pm 0.1)}$
Δ (expected)	~ 60 kHz	~ 6 MHz	~ 3 MHz
Δ (measured)	(12 ± 1) kHz	(7 ± 3) MHz	(1 ± 1) MHz
τ_c (expected)	~ 15 μs	~ 0.17 μs	~ 0.34 μs
τ_c (measured)	(52 ± 11) μs	(3 ± 2) μs	(10 ± 5) μs

where Δ_N is the dipolar interaction between N electronic spins. In this physical picture, ΔE is proportional to the concentration of ^{13}C impurities and to the N ^{13}C hyperfine interaction energy, whereas Δ_N is proportional to the N concentration.

In Samples F and G, the N ^{13}C hyperfine interaction is dominated by the strong contact term (compared to the weaker dipolar contribution, see [127, 128]). Therefore, the inhomogeneous broadening energy ΔE does not scale simply with the concentration of ^{13}C. To make a realistic estimate of ΔE, we carried out a Monte-Carlo simulation of 1000 pairs of N spin impurities, each with a different random distribution of ^{13}C spin impurities in a diamond lattice at their natural abundance of 1.1%. The calculated relative electronic spin resonance frequency shift for each N pair is plotted in Figure 7.6. We find the average value of this detuning ≈ 9.5 MHz and the standard deviation ≈ 30 MHz, with a few rare events in which a ^{13}C occupies the nearest lattice to the N, producing a frequency shift ~ 300 MHz. Thus, we estimate $\Delta E \sim 10$ MHz and $\Delta_N \sim 1$ MHz for Samples F and G. These values imply an order of magnitude suppression of R compared to the bare electronic spin flip-flop rate ignoring N ^{13}C interactions ($R_{\text{bare}} \sim \Delta_N$), which is consistent with our experimental results for $\tau_c \sim 1/R$ (see Table 7.1). For Sample C, the low concentration of ^{13}C spins greatly reduces the magnitude of ΔE, and hence the spin bath suppression is negligible.

7.3.2 Ensemble averaging

Independent measurements of N and NV concentration were performed on each sample to confirm that sample inhomogeneities are within acceptable ranges and

Chapter 7: Spectral Decomposition
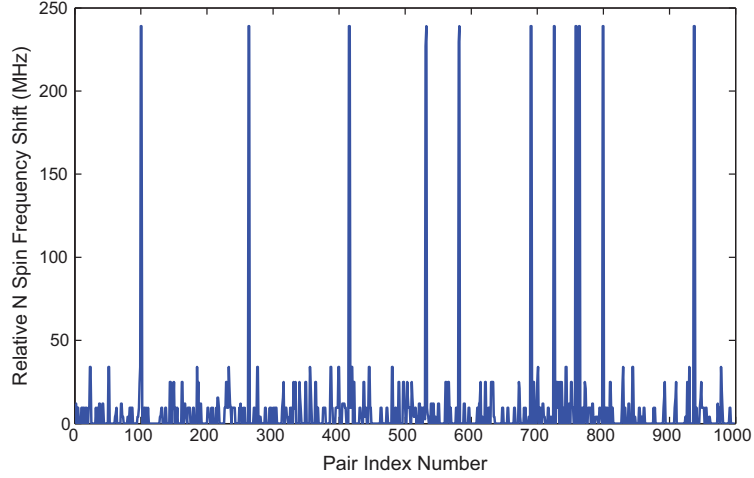
Figure 7.6: Monte Carlo simulation of the relative frequency shift between 1000 pairs of N electronic spins induced by hyperfine interactions with ^{13}C nuclear spin impurities that are randomly distributed in a diamond lattice at the natural abundance concentration of 1.1%.

therefore do not greatly affect the results of the spectral decomposition analysis. Sample C has a low N concentration that is below the detection threshold of the standard secondary ion mass spectroscopy (SIMS) technique; as a result, we performed confocal scans on the sample to measure the spatial distribution of NV centers (see Figure 7.7). The sample consists of a type 1b HPHT substrate with typical high N and low NV concentration (corresponding to the $160 - 260\,\mu$m range in Figure 7.7) which was overgrown with a CVD layer $\sim 160\,\mu$m thick. The majority of the NV fluorescence comes from a $\sim 60\,\mu$m thick region within the CVD layer (corresponding to the $75 - 135\,\mu$m range in Figure 7.7). Consequently, the measurements performed on this sample exclusively probe this region, which shows less than a factor of two variation in NV concentration throughout its depth. With the reasonable assumption that N and NV concentrations are proportional to each other, we conclude that the N concentration probed in this sample is similarly homogeneous to within about a factor of two.

We performed SIMS measurements on Sample F to characterize inhomogeneity in the N concentration (see Figure 7.8). Again assuming the N and NV concentrations are locally proportional to each other, we determined the mean N concentration probed by NV fluorescence measurements, $\overline{n_{\rm N}}$, from a weighted average over the local N concentration $n_{\rm N}(z)$:

$$\overline{n_{\rm N}} = \frac{\int_0^Z dz\, n_{\rm N}^2(z)}{\int_0^Z dz\, n_{\rm N}(z)}. \tag{7.9}$$

Using the SIMS data we find $\overline{n_{\rm N}} \simeq (2.6 \pm 1.7) \times 10^{19}\,{\rm cm}^{-3} (\simeq 150 \pm 100\ {\rm ppm})$, which is
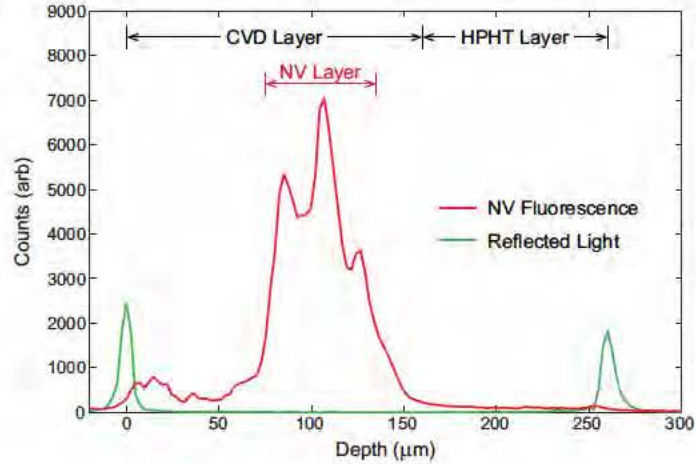
Figure 7.7: Confocal scan of NV fluorescence and hence concentration (red) as a function of depth in Sample C. The green line indicates the surfaces of the sample as measured by enhanced reflection of the green excitation light.

consistent with the coupling strength Δ extracted using the spectral decomposition technique and with Monte Carlo simulations of the spin environment. In addition, our measurements were carried out on a confined lateral region $\sim 10 \, \mu m \times 10 \, \mu m$ to suppress the effects of inhomogeneities on a larger scale. The SIMS measurements also indicate that within the detection limits (1 ppm) there are no other extrinsic defects present, such as Boron or Si.

As is typical of type 1b HPHT diamonds, Sample G contains a high concentration of N impurities (~ 50 ppm) and very low concentration of NV centers, allowing for single NV measurements using a confocal apparatus. As a result, possible inhomogeneities of the N concentration do not affect the measured data. The sample was characterized by SIMS to have an N concentration of approximately $50 - 150$ ppm, consistent with the value for coupling strength Δ extracted using the spectral decomposition technique.

For all three samples, the spectral decomposition technique yielded values for coupling strength Δ which are consistent with independent measurements and estimates of the N concentration, suggesting that sample inhomogeneities are within expected ranges and understood to within a factor of 2-3. As a result, we have confidence that the values for the N spin bath correlation time τ_c provided by the spectral decomposition technique are, for Samples F and G, an order of magnitude longer than the expected values given by a simple model of the N spin bath that ignores N ^{13}C interactions. Furthermore, the results we obtained via spectral decomposition could not be recreated with any combination of Δ and τ_c that follow the expected scaling with N concentration, regardless of the actual value of the assumed concentration and even when inhomogeneous effects are taken into account. Therefore, the com-
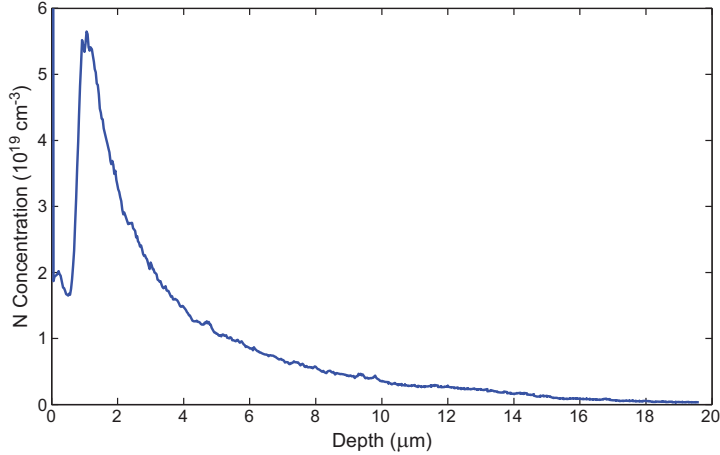
Figure 7.8: Inhomogeneity of N concentration in Sample F as measured using secondary ion mass spectroscopy.

bined results from the three samples, along with the independent measurements of N concentration and the consistency of the extracted values for Δ, strongly support the validity of the unexpectedly long correlation time τ_c observed in Samples F and G.

7.4   Summary

In summary, we applied the spectral decomposition technique to three diamond samples with different composite spin environments in order to characterize their spin bath dynamics. For samples with a finite concentration of ^{13}C nuclear spin impurities, this technique revealed an order of magnitude suppression of the N electronic spin bath dynamics, which can be explained by random interactions between proximal electronic and ^{13}C nuclear spin impurities. This spin bath suppression enhances the efficacy of dynamical decoupling in samples with high N impurity concentration and therefore has important implications in achieving optimized NV ensemble magnetometry.

Recall that NV magnetic sensitivity is dependent on the product of NV spin coherence time and the number of photons collected per measurement, where the photons collected is typically proportional to the number of NV centers probed, which is in turn proportional to the N concentration. In this work, we realized a product of NV spin density and coherence time of $\sim 3 \times 10^{14}$ ms/cm^3 in Sample F at room temperature due to spin bath suppression. This spin density-coherence time product is within an order of magnitude of the state-of-the-art product achieved in atomic systems [129]. Further optimization may be possible by engineering the spin bath suppression, e.g., with ^{13}C concentration higher than the natural value. Such optimization, along with spectral decomposition studies of samples with varying ^{13}C and

N concentrations, in a range of temperatures, and at high magnetic fields, will be pursued in future work.

Finally, it is also worthwhile to note that the spectral decomposition technique presented here, based on well-known pulse sequences and a simple reconstruction algorithm, can be applied to other composite solid-state spin systems, such as quantum dots and phosphorous donors in silicon. Such measurements could provide a powerful approach for the study of many-body dynamics of complex spin environments, potentially exhibiting nontrivial effects related to the interplay between nuclear and electronic spin baths.

Chapter 8

Outlook

8.1 Sensitivity of an NV magnetic sensor

In addition to the techniques discussed in this dissertation, there have been a number of efforts in recent years to improve the sensitivity of NV based magnetometers. Recall from Chapter 2 that NV sensitivity is dependent on three main factors   measurement contrast α, number of photons collected per measurement β, and measurement time T (limited by the NV spin dephasing time T_2^* for DC measurements and coherence time $T_2^{(n)}$ for AC measurements)   given by the following equation:

$$\eta \propto \frac{1}{\alpha\sqrt{\beta T}}.$$

(8.1)

We summarize recent improvements to each of these factors individually.

8.1.1 Measurement contrast

In Chapter 5, we discussed using diamonds that have been CVD-grown such that the NV centers are preferentially oriented along two axes in order to increase the contrast of an ensemble measurement by a factor of ~ 2. As discussed previously however, using these diamonds has several disadvantages. First, these samples only allow for the measurement of magnetic field projections along two independent axes whereas three are necessary for a full vector reconstruction. Also, because preferential NV orientation has thus far only been observed in CVD-grown samples, there are constraints on the additional material processing that can be performed on the diamond. Further irradiation and annealing to increase the typically poor as-grown N-to-NV conversion will destroy the preferential orientation. However, a technique wherein an external strain is introduced to the diamond crystal during annealing in

order to induce a re-orientation of the defects along a preferred direction has been demonstrated on neutral carbon <100>-split interstitial defects in diamond [89] and may also prove applicable to NV centers.

There are other possible methods for improving measurement contrast, which may be employed in addition to or as an alternative to using samples with preferential NV orientation. For example, an additional MW π pulse may be applied to the three degenerate non-aligned NV orientation classes after initialization to transfer their spin population into the less fluorescent $|1\rangle$ state, thus reducing their contributions to the background. Another technique for reducing background fluorescence is to apply a high enough static field (~ 500 G) such that NV spin state mixing suppresses fluorescence in the non-aligned NV orientation classes [130]. These additional contrast improvement techniques and others will be explored in future work.

8.1.2   Number of photons collected per measurement

There are two main factors that determine the number of photons collected per measurement: the number of NV sensors probed in the measurement and the photon collection efficiency of the experimental apparatus.

Number of NV sensors

As discussed previously, increasing the number of NV sensors involved in the measurement i.e., the NV concentration in the measurement volume in practice often requires a corresponding increase in N incorporation into the diamond. The increased N electronic spin impurity concentration decreases the NV spin coherence time which in turn adversely affects the magnetic sensitivity. Instead, much recent work has focused on improving the N-to-NV conversion efficiency, which is typically very low in as-grown N-doped CVD samples ($< 0.5\%$) and standard N ion implanted samples ($\sim$ 1-5%). By irradiating with, e.g., electrons [36, 34, 35], protons [34], neutrons [33], carbon ions [17], or heavy ions [36] in order to create vacancies in the diamond crystal and subsequently annealing, N-to-NV conversion efficiencies as high as $\sim 50\%$ have been achieved [16, 17].

Photon collection efficiency

The refractive index of diamond is ≈ 2.42, which corresponds to a critical angle of $\approx 24.5°$ at a diamond-air interface and, in a typical bulk setup, $\sim 90\%$ of the NV fluorescence being totally internally reflected back into the diamond. Taking into account the numerical aperture (NA) of the objective lens, the loss through
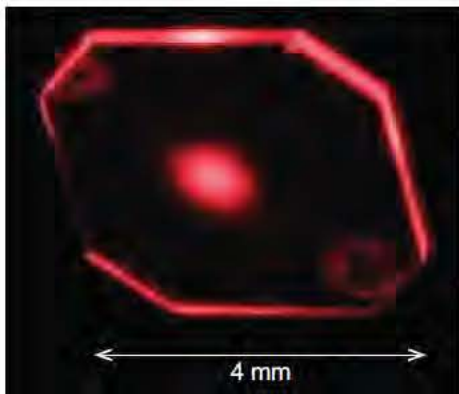
Figure 8.1: Red-filtered photograph of NV fluorescence from a planar diamond sample containing a relatively high NV concentration (NV $\sim$ 1 ppm). Guiding of NV fluorescence light is evident as a bright glow around the diamond's perimeter, while a 532-nm laser beam passes through its center [70].

various optical elements in the experimental apparatus, and the detection efficiency of the CCD, a typical wide-field setup collects $\sim$ 3-8% of the NV fluorescence photons emitted during a measurement.

In order to improve photon collection efficiency, there have been various recent efforts to fabricate diamond microstructures designed to couple NV fluorescence more strongly to a detector. For example, a diamond solid immersion lens (SIL) of radius $\sim$ 500 μm demonstrated a collection efficiency of slightly less than 20% [67], whereas another diamond SIL of radius $\sim$ 2.5 μm gave a (calculated) collection efficiency of $\sim$ 30% [68]. Another geometry that has been recently reported is a diamond nanowire; such a waveguiding microstructure of radius $\sim$ 100 nm and height $\sim$ 2 μm demonstrated a collection efficiency of $\sim$ 40% [69].

An alternative to fabricating microstructures in diamond, which can be quite a difficult material to etch, is to simply collect the totally internally reflected NV fluorescence as it escapes out of the edges of a typical planar diamond sample (see Figure 8.1). A prototype device in which four photon detectors are positioned at the edges a diamond sample has demonstrated a collection efficiency of $\sim$ 47%, with up to $\sim$ 90% theoretically achievable [70].

8.1.3 Coherence Time

In ultra-pure diamonds engineered with low N electronic spin impurities and low ^{13}C nuclear spin impurities, single NV center spin coherence times as long as $\sim$ 2 ms have been observed at room temperature [1]. By applying dynamical decoupling techniques as discussed in Chapter 6, comparable coherence times have been

achieved in NV ensembles with higher NV concentrations desirable for enhanced magnetic sensitivity. The NV spin coherence time is limited by spin-phonon relaxation to several milliseconds at room temperature; however as discussed in Chapter 6, for magnetic sensing applications where the temperature requirements are less constrained, longer coherence times and hence more sensitive magnetic field measurements may be achieved by operating at colder temperatures. An NV coherence time $T_2^{(n)} \gtrsim 10$ ms is achievable with thermoelectric cooling and $T_2^{(n)} > 0.5$ s with liquid nitrogen cooling [131].

8.2 Spatial resolution of an NV magnetic sensor

One region of parameter space that NV based magnetic sensors can cover which is inaccessible to most currently available magnetic sensing technologies is in performing sensitive magnetic field measurements with high spatial resolution under ambient conditions. Figure 8.2 plots the spatial resolution and magnetic sensitivity of a variety of recently demonstrated magnetometers. Note that NV based magnetic sensors have the added benefit of operating sensitively under ambient conditions. In contrast, superconducting quantum interference devices (SQUIDs) require cryogenic temperatures; Bose-Einstein condensates (BECs) require vacuum; and magnetic resonance force microscopes (MRFMs) operate optimally under vacuum at cryogenic temperatures. Furthermore, while the wide-field and confocal setups discussed in this dissertation are fundamentally limited by optical diffraction to ~ 300 nm, several techniques have been proposed and demonstrated to achieve significantly better spatial resolution.

Scanning tip magnetometer

There have been several recent demonstrations of magnetic sensing using single NV centers in a scanning-tip geometry. *Rondin et al.* attached a diamond nanocrystal containing a single NV to an atomic force microscope (AFM) tip and performed DC magnetometry with $\approx 9\,\mu T/\sqrt{Hz}$ sensitivity and tens of nm spatial resolution [154]. *Maletinsky et al.* fabricated a diamond nanopillar containing a single NV center at the tip and demonstrated AC magnetometry with $\approx 56\,nT/\sqrt{Hz}$ sensitivity and ~ 10 nm spatial resolution [155]. These initial demonstrations already surpass the spatial resolutions achieved by any of the alternative magnetic sensing technologies except for MRFM, which has the same geometry. It is important to note however that while the scanning-tip geometry allows for significantly improved spatial resolution, there are also trade-offs: due to the small volume of the tip, incorporating more than one NV center into the desired region is rather difficult without significantly degrading
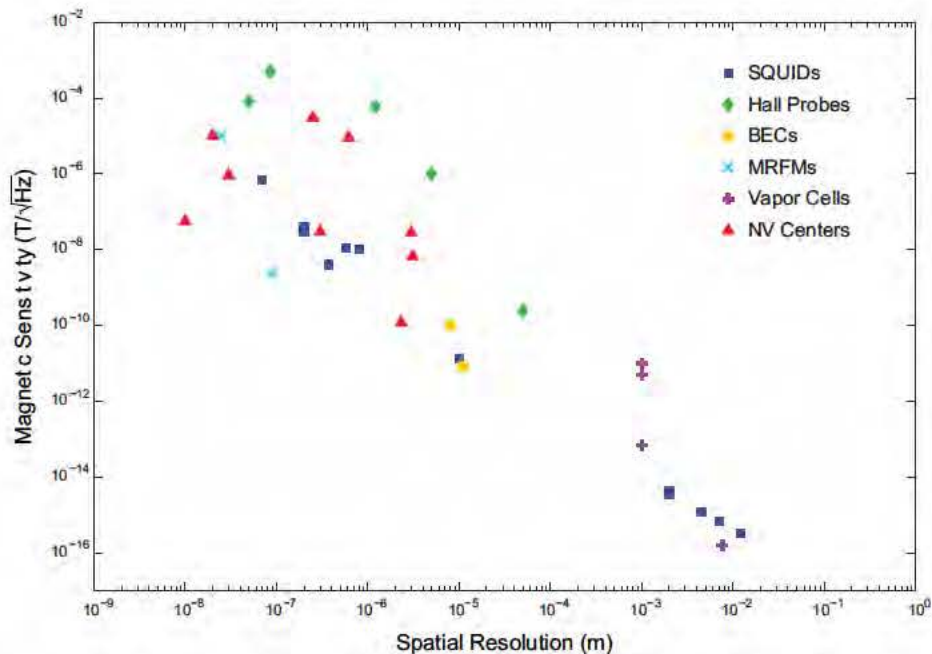
Figure 8.2: Plot of the spatial resolution versus magnetic sensitivity of a variety of recently demonstrated magnetic sensing technologies: superconducting quantum interference devices (SQUIDs) [132, 133, 134, 135, 136, 137, 138, 139], scanning Hall probes [140, 141, 142, 143, 144], magnetometers employing Bose-Einstein condensates (BECs) [145, 146], magnetic resonance force microscopes (MRFMs) [147, 148], atomic vapor cells and spin exchange relaxation-free (SERF) magnetometers [149, 150, 151, 152], and NV magnetometers [65, 59, 85, 153, 70, 154, 155].

the NV spin coherence and consequently magnetic sensitivity. The NV center often also experiences surface effects which can shorten the coherence time. We will discuss these trade-offs in more detail in the next section.

Stimulated emission depletion microscopy

Another approach for achieving sub-optical-diffraction-limited spatial resolution is to employ super-resolution optical schemes. For example, *Rittweger et al.* were able to use a stimulated emission depletion (STED) microscope to resolve single NV centers with 5.8 nm spatial resolution [156]. This technique has several advantages over a scanning tip geometry in that diamond fabrication is not necessary and higher NV concentrations are more easily probed. Thus far, simultaneous STED microscopy and DC magnetometry has achieved $\approx 1\,\mu T/\sqrt{Hz}$ sensitivity and ~ 30 nm spatial resolution [153], with further improvements in progress.

8.3 Discussion of trade-offs

One of the most powerful advantages of NV based magnetic sensors is their versatility. In this dissertation, we have discussed a variety of diamond geometries (e.g., NV centers homogeneously distributed throughout a bulk sample, NV centers occupying a thin layer at the surface of a bulk sample, and NV centers at the tip of a scanning probe); measurement schemes (e.g., side-collection, simultaneous wide-field imaging onto a CCD, scanning confocal microscopy, and STED microscopy); and techniques for improving magnetic sensitivity (e.g., preferential NV orientation, dynamical decoupling, irradiation and annealing, and performing measurements at low temperatures). However as discussed previously, each technique has advantages and disadvantages. A CCD based measurement scheme allows for simultaneous imaging of magnetic fields over large regions, but spatial resolution is limited by optical diffraction. A scanning tip geometry and STED microscopy allow for sub-optical-diffraction spatial resolution, but both require scanning and are consequently limited in how rapidly large fields of view may be imaged. Also, while many of the geometries, measurement schemes, and magnetic sensitivity enhancing techniques can be combined, some are incompatible. For example, irradiating and annealing diamond samples in order to increase NV concentration and subsequently improve magnetic sensitivity currently irreversibly destroys any preferential NV orientation and the corresponding enhancements to measurement contrast and magnetic sensitivity. Fortunately, the high degree of flexibility in NV based magnetic sensor implementation allows for the optimization of different NV magnetometers for different applications.

8.4 Applications

The ability to map magnetic fields with high sensitivity and spatial resolution at room and near-room temperature may provide additional information in a variety of areas that were previously inaccessible with current magnetic sensing technologies. In particular, an NV based magnetic imager may be applied to study bio-magnetic fields in living organisms, recently demonstrated for the first time on magnetotactic bacteria (see Figure 8.3) [54].

Another potential bio-application for an NV ensemble magnetic field imager is in studying connectivity and signaling in functional, cultured neuronal networks. These collections of neurons interconnected by synapses provide the physical basis of central and peripheral nervous systems, but despite rapid advances in neuroscience, a clear understanding has yet to emerge of how microscopic connectivity of neurons encodes macroscopic function of the network. Determining the rules for translating neuronal connectivity to network function will require experimental tools that are
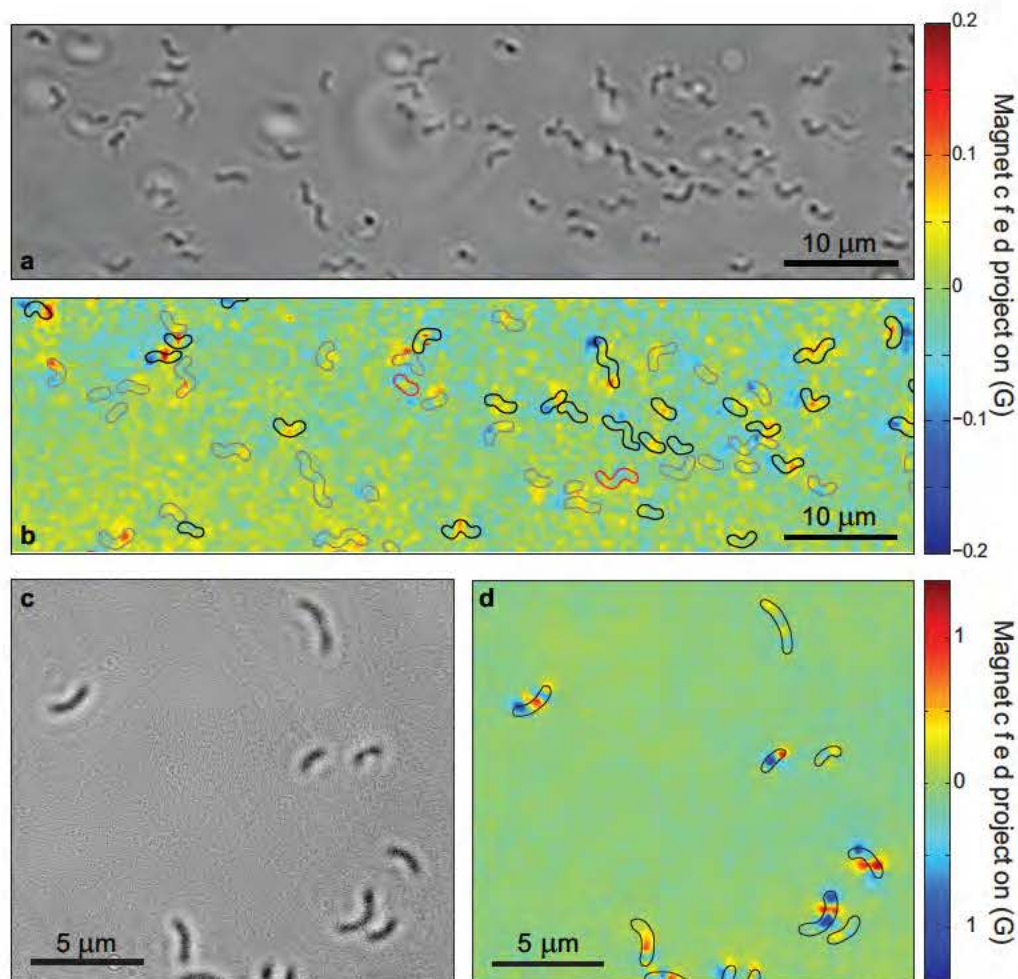
Figure 8.3: Wide-field optical and magnetic images of magnetotactic bacteria. (a) Bright-field optical images of MTB adhered to the diamond surface while immersed in phosphate buffer solution. Several out-of-focus bacteria are also visible floating above the diamond surface. (b) Image of magnetic field projection along the [111] crystallographic axis in the diamond for the same region shown in (a) determined from NV ESR spectra. Outlines are superimposed on the magnetic field image to indicate the locations of the MTB determined from bright-field images, and the colour of the outlines indicate the results of a bacterial live-dead assay performed after measuring the magnetic field (black for living, red for dead, and grey for indeterminate). (c) Bright-field image of several dried MTB on the surface of the diamond chip. (d) Image of magnetic field projection along the [111] axis for the same region shown in (c) determined from NV ESR spectra, with outlines to indicate the locations of MTB determined from (c) [54].

capable of real-time mapping of both local and global spatiotemporal connectivity among neurons and signal propagation between them. However, given the size of a biologically relevant, functional neuronal network ($\sim$ 1 mm or larger), such real-time functional imaging is a formidable challenge beyond the capabilities of existing experimental instruments and methodologies.

With further technical improvements such as those discussed in this dissertation, an optimized NV ensemble magnetic field imager may be able to address this challenge by providing micron-scale mapping of magnetic fields on a sub-millisecond time scale for all neurons within a functional network cultured on the bio-inert surface of a diamond magnetometer chip. This mapping of neuronal activity via magnetic field imaging is minimally invasive and can be correlated against stimulation and/or reward administration to identify the presence and emergence of persistent patterns of local and global activity.

NV magnetic sensors have also recently been employed to measure nuclear magnetic resonance from organic material deposited at the surface of the diamond substrate [55, 56]. More potential applications   such as in biomagnetism (e.g., cardiac cells, magnetic organs used for navigation, etc.), novel material characterization (e.g., graphene), and paleomagnetism (e.g., dynamo theory)   will be explored as the capabilities NV magnetic sensing technology continue to improve.

Appendix A

NV Magnetic Sensitivity

A.1   DC magnetometry: ESR

To derive the optimum sensitivity of an NV magnetometer which uses ESR spectra to measure DC magnetic fields, first consider the intensity profile of an NV resonance in the ESR spectrum (see Figure A.1):

$$\mathcal{I}(\nu_{\mathrm{m}}) = \mathcal{R}\left[1 - \alpha\mathcal{F}\left(\frac{\nu_{\mathrm{m}} - \nu_0}{\Delta\nu}\right)\right] \tag{A.1}$$

where $\mathcal{R}$ is the rate of detected photons per second, α is the contrast of the resonance dip, $\mathcal{F}$ is a function describing the lineshape of the resonance, $\Delta\nu$ is the linewidth (full-width at half-maximum) of the resonance, and ν_0 is the resonance frequency. Recall that the resonance frequency is related to the magnetic field by the simple Larmor equation $\nu_0 = \gamma B_0$, where B_0 is the projection of the magnetic field along the NV symmetry axis and the NV gyromagnetic ratio is $\gamma = \frac{\mathrm{g}\mu_{\mathrm{B}}}{\mathrm{h}} \approx 2.8$ MHz/G.

The linewidth $\Delta\nu$ is fundamentally limited by the characteristic dephasing time T_2^*, which is dependent on inhomogeneities in the magnetic environment of the NV center(s), as discussed in Chapter 1. The lineshape $\mathcal{F}$ of the resonance may be described by a Gaussian function (e.g., when a large number of nuclear ^{13}C spins dominate the dephasing), a Lorentzian function (e.g., when paramagnetic spins corresponding to nitrogen defects dominate the dephasing or when the resonance is power-broadened due to continuous laser or microwave excitation), or possibly a convolution of both (i.e., a Voigt function).

The fluorescence intensity $\mathcal{I}$ is most sensitive to small changes in the magnetic field at the point of maximum slope:

$$\max\left|\frac{\partial\mathcal{I}}{\partial\nu_{\mathrm{m}}}\right| = \frac{\alpha\mathcal{R}}{\Delta\nu\mathcal{P}_{\mathcal{F}}} \tag{A.2}$$
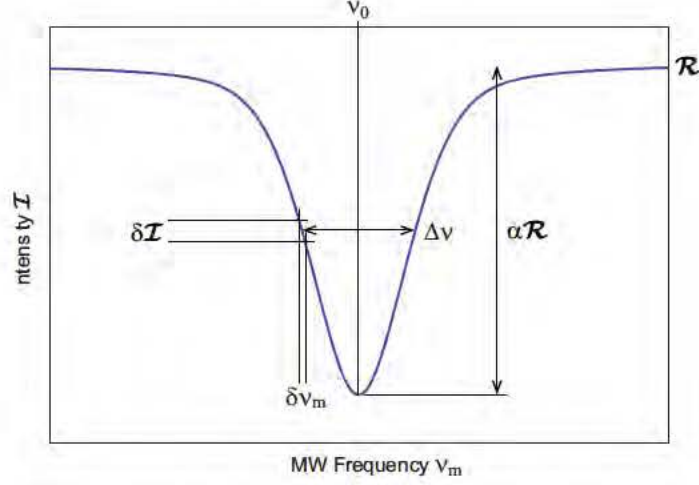
Figure A.1: Intensity profile of an NV resonance in the ESR spectrum illustrating the sensitivity of an ESR based DC magnetic field measurement.

We define the numerical parameter $\mathcal{P}_\mathcal{F}$, which is related to the specific profile $\mathcal{F}$ of NV resonance. For a Gaussian lineshape, $\mathcal{P}_\mathcal{F} = \sqrt{e/8\ln2} \approx 0.70$; for a Lorentzian lineshape, $\mathcal{P}_\mathcal{F} = 4/3\sqrt{3} \approx 0.77$ [57].

Consider a measurement of duration t_m. Assuming low contrast α, the number of photons collected per measurement $\beta = \mathcal{I}t_\mathrm{m}$ can be approximated by $\beta \approx \mathcal{R}t_\mathrm{m}$, and the corresponding photon shot noise can be approximated by $\delta\beta \approx \sqrt{\mathcal{R}t_\mathrm{m}}$. The shot-noise-limited minimum detectable field $\delta\mathrm{B}_\mathrm{min}$ for this measurement can be calculated from the photon shot noise at the point of maximum slope (Figure A.1):

$$\gamma\delta\mathrm{B}_\mathrm{min} = \delta\nu_{\mathrm{m,min}} = \frac{\delta\beta}{\max\left|\frac{\partial\beta}{\partial\nu_\mathrm{m}}\right|} \approx \frac{\sqrt{\mathcal{R}t_\mathrm{m}}}{t_\mathrm{m}\max\left|\frac{\partial\mathcal{I}}{\partial\nu_\mathrm{m}}\right|} \tag{A.3}$$

Substituting in Equation A.2, Equation A.3 becomes:

$$\delta\mathrm{B}_\mathrm{min} \approx \mathcal{P}_\mathcal{F}\frac{\mathrm{h}}{\mathrm{g}\mu_\mathrm{B}}\frac{\Delta\nu}{\alpha\sqrt{\beta}} \tag{A.4}$$

The sensitivity η_esr of the measurement is then given by the following relation [60, 52]:

$$\eta_\mathrm{esr} = \delta\mathrm{B}_\mathrm{min}\sqrt{t_\mathrm{m}} = \mathcal{P}_\mathcal{F}\frac{\mathrm{h}}{\mathrm{g}\mu_\mathrm{B}}\frac{\Delta\nu\sqrt{t_\mathrm{m}}}{\alpha\sqrt{\beta}} \tag{A.5}$$

The magnetic field sensitivity is dependent on resonance contrast α, number of photons collected per measurement β, resonance linewidth $\Delta\nu$, and measurement duration t_m. These parameters are not independent of each other: the resonance contrast α may be increased by increasing the power of the microwave excitation at the expense

of increasing the linewidth $\Delta\nu$ due to power broadening. Likewise, the linewidth $\Delta\nu$ may be decreased (up to a limit defined by the NV spin characteristic dephasing time T_2^*) by lowering the laser excitation power to reduce power broadening; however doing so decreases number of photons collected per measurement β. Optimizing these parameters to achieve best DC magnetic field sensitivity using the ESR method yields [57]:

$$\eta_{\mathrm{esr}} \sim \mathcal{P}_{\mathcal{F}} \frac{2\hbar}{\mathrm{g}\mu_{\mathrm{B}}} \frac{1}{\alpha\sqrt{\beta\mathrm{T}_2^*}} \tag{A.6}$$

A.2   DC magnetometry: Ramsey sequence

To derive the optimum sensitivity of an NV magnetometer that uses the Ramsey pulse sequence to measure DC magnetic fields, first consider the signal $\mathcal{S}$, defined previously as the number of photons collected in one measurement and dependent on the magnitude B of the static magnetic field to be measured. (Note that B is an additional static field separate from the known static field B_0, which was applied to spectrally distinguish the four NV orientation classes.) As a result, the unknown magnetic field magnitude B can be extracted from the signal $\mathcal{S}$, and the uncertainty in the signal $\delta\mathcal{S}$ is related to a corresponding uncertainty in the measured field δB by the slope:

$$\delta\mathcal{S} = \frac{\partial\mathcal{S}}{\partial B}\delta B \tag{A.7}$$

The signal is most sensitive to small changes in the magnetic field at the point of maximum slope. As a result, the minimum resolvable magnetic field δB_{min} is given by:

$$\delta B_{\mathrm{min}} = \frac{\delta\mathcal{S}}{\max\left|\frac{\partial\mathcal{S}}{\partial B}\right|} \tag{A.8}$$

where the maximum slope can be determined from the Ramsey magnetometry curve given in the main text by Equation 2.3:

$$\max\left|\frac{\partial\mathcal{S}}{\partial B}\right| = \max\left|-2\pi\gamma\tau\frac{(a-b)}{2}\sin\left(2\pi\gamma B\tau\right)\right| = 2\pi\gamma\tau\frac{(a-b)}{2} \tag{A.9}$$

Equation A.9 can be written in terms of the average number of photons collected per measurement $\beta = (a+b)/2$ and the measurement contrast $\alpha = (a-b)/(a+b)$:

$$\max\left|\frac{\partial\mathcal{S}}{\partial B}\right| = 2\pi\gamma\tau\frac{(a-b)}{(a+b)}\frac{(a+b)}{2} = 2\pi\gamma\tau\alpha\beta \tag{A.10}$$

In typical NV measurements, the number of photons collected from each NV is quite small. As a result, the uncertainty in the signal is dominated by photon shot noise
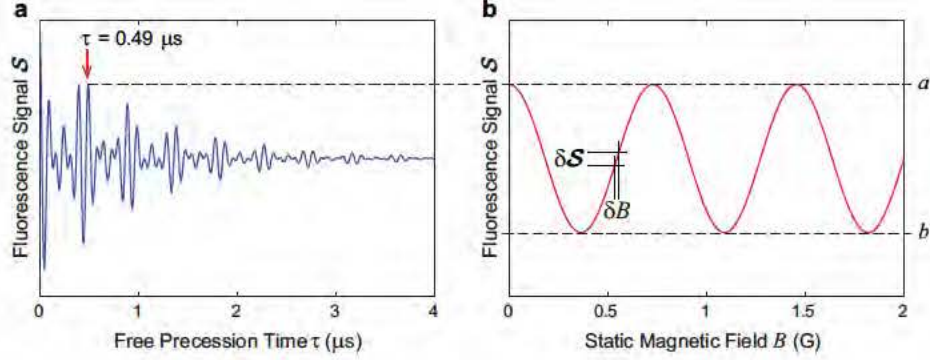
Figure A.2: Sensitivity of a Ramsey based DC magnetic field measurement. (a) Modeled Ramsey FID curve, with the free precession time $\tau = 0.49\,\mu\text{s}$ used for the magnetic measurement indicated by a red arrow. (b) Example magnetometry curve illustrating the uncertainty δB in the measured magnetic field due to fluctuations $\delta\mathcal{S}$ in the fluorescence signal.

and can be approximated by $\delta\mathcal{S} \approx \sqrt{\beta}$:

$$\delta B_{\min} \approx \frac{\sqrt{\beta}}{2\pi\gamma\tau\alpha\beta} \approx \frac{\hbar}{\text{g}\mu_{\text{B}}}\frac{1}{\tau}\frac{1}{\alpha\sqrt{\beta}} \tag{A.11}$$

In more advanced measurement schemes with higher photon collection and measurement contrast (e.g., single-shot read-out), spin projection noise must also be incorporated into the uncertainty $\delta\mathcal{S}$ [52]. Note that other noise sources, such as electronic noise, may also limit the magnetic sensitivity.

The sensitivity η_{ramsey} of the measurement is then given by the following relation:

$$\eta_{\text{ramsey}} = \delta B_{\min}\sqrt{t_{\text{m}}} \approx \frac{\hbar}{\text{g}\mu_{\text{B}}}\frac{1}{\sqrt{\tau}}\frac{1}{\alpha\sqrt{\beta}} \tag{A.12}$$

where the time t_{m} of a measurement is approximated by the free precession time τ.

As in the DC magnetometry scheme utilizing ESR spectroscopy, the magnetic field sensitivity is dependent on resonance contrast α, number of photons collected per measurement β, and measurement duration τ. Also as before, these parameters are not independent. The measurement contrast decays as a result of NV spin dephasing, with characteristic time scale T_2^*. Thus, increasing the measurement duration τ degrades the contrast α; the optimum magnetic field sensitivity is achieved when $\tau \sim \text{T}_2^*$:

$$\eta_{\text{ramsey}} \sim \frac{\hbar}{\text{g}\mu_{\text{B}}}\frac{1}{\alpha\sqrt{\beta\text{T}_2^*}} \tag{A.13}$$

Figure A.3: Sensitivity of a spin echo based AC magnetic field measurement. (a) Measured spin echo decoherence curve of an NV ensemble, with the spin echo time $\tau = 324.4\,\mu s$ used for the magnetic measurement indicated by a red arrow. (b) Example magnetometry curve illustrating the uncertainty δB in the measured magnetic field due to fluctuations δS in the fluorescence signal.

A.3 AC magnetometry

In this section, we derive the sensitivity of an NV magnetometer which employs a spin echo pulse sequence to measure an AC magnetic field along the NV axis, described by $b(t) = B\sin\left(2\pi f_{ac}t - \varphi_0\right)$. The MW echo pulse of the sequence occurs at $t = \tau/2$, where the full pulse duration τ is related to the magnetic field frequency f_{ac} as stated in Chapter 2.

The phase ϕ accumulated by the NV spins over the pulse sequence duration is given by:

$$\phi = \int_0^{\frac{\tau}{2}} 2\pi\gamma b(t)dt - \int_{\frac{\tau}{2}}^{\tau} 2\pi\gamma b(t)dt \qquad (A.14)$$

$$\phi = 4\pi\gamma B \int_0^{\frac{\tau}{2}} \sin\left(2\pi f_{ac}t - \varphi_0\right)dt \qquad (A.15)$$

$$\phi = 4\gamma B\tau \cos\left(\varphi_0\right) \qquad (A.16)$$

For simplicity, let us focus on the optimal situation where the MW pulses coincide with the nodes of the AC field [see Figure 2.3(a)]. In this case, $\varphi_0 = 0$ and the phase accumulated by the NV spins and subsequently the sensitivity to magnetic fields is maximized. As mentioned previously, AC magnetic fields with randomly fluctuating phases may also be measured using a variant of the spin echo pulse sequence; however, the sensitivity is poorer, as discussed elsewhere [63, 64].

Appendix A: NV Magnetic Sensitivity

As in the Ramsey DC magnetometry technique, we define the signal $\mathcal{S}$ as the number of photons collected in one measurement, where $\mathcal{S}$ oscillates between a (corresponding to a phase accumulation of $\phi = 0$) and b (corresponding to a phase accumulation of $\phi = \pi$):

$$\mathcal{S} = \frac{(a+b)}{2} + \frac{(a-b)}{2}\cos(\phi) \tag{A.17}$$

$$\mathcal{S} = \frac{(a+b)}{2} + \frac{(a-b)}{2}\cos(4\gamma B\tau) \tag{A.18}$$

The unknown magnetic field amplitude B can be extracted from the signal $\mathcal{S}$, and the uncertainty in the signal $\delta\mathcal{S}$ is related to a corresponding uncertainty in the measured field δB by the slope:

$$\delta\mathcal{S} = \frac{\partial\mathcal{S}}{\partial B}\delta B \tag{A.19}$$

The signal is most sensitive to small changes in the magnetic field at the point of maximum slope, which from Equation A.18 is:

$$\max\left|\frac{\partial\mathcal{S}}{\partial B}\right| = \max\left|-4\gamma\tau\frac{(a-b)}{2}\sin(4\gamma B\tau)\right| \tag{A.20}$$

$$\max\left|\frac{\partial\mathcal{S}}{\partial B}\right| = 4\gamma\tau\frac{(a-b)}{2} \tag{A.21}$$

Equation A.21 can be written in terms of the average number of photons collected per measurement $\beta = (a+b)/2$ and the measurement contrast $\alpha = (a-b)/(a+b)$:

$$\max\left|\frac{\partial\mathcal{S}}{\partial B}\right| = 4\gamma\tau\frac{(a-b)}{(a+b)}\frac{(a+b)}{2} = 4\gamma\tau\alpha\beta \tag{A.22}$$

In typical NV measurements, the number of photons collected from each NV is quite small. As a result, the uncertainty in the signal is dominated by photon shot noise and can be approximated by $\delta\mathcal{S} \approx \sqrt{\beta}$. The minimum resolvable magnetic field $\delta B_{\min}$ is therefore given by:

$$\delta B_{\min} = \frac{\delta\mathcal{S}}{\max\left|\frac{\partial\mathcal{S}}{\partial B}\right|} \tag{A.23}$$

$$\delta B_{\min} \approx \frac{\sqrt{\beta}}{4\gamma\tau\alpha\beta} \approx \frac{\pi\hbar}{2g\mu_{\mathrm{B}}}\frac{1}{\tau}\frac{1}{\alpha\sqrt{\beta}} \tag{A.24}$$

In more advanced measurement schemes with higher photon collection and measurement contrast (e.g., single-shot read-out), spin projection noise must also be incorporated into the uncertainty $\delta\mathcal{S}$ [52]. Note that other noise sources, such as electronic noise, may also limit the magnetic sensitivity.

Appendix A: NV Magnetic Sensitivity

The sensitivity η_{se} of the spin echo measurement is then given by the following relation:

$$\eta_{se} = \delta B_{min}\sqrt{t_m} \approx \frac{\pi\hbar}{2g\mu_B} \frac{1}{\sqrt{\tau}} \frac{1}{\alpha\sqrt{\beta}} \tag{A.25}$$

where the measurement time t_m is approximated by the full free precession time τ.

Similar to the other NV magnetometry schemes discussed thus far, the magnetic field sensitivity is dependent on resonance contrast α, number of photons collected per measurement β, and measurement duration τ. Again, these parameters are not independent; the measurement contrast decays as a result of NV spin decoherence, with characteristic time scale T_2. Thus, increasing the measurement duration τ degrades the contrast α; the optimum magnetic field sensitivity for an spin echo measurement is achieved when $\tau \sim T_2$ [52]:

$$\eta_{se} \sim \frac{\pi\hbar}{2g\mu_B} \frac{1}{\alpha\sqrt{\beta T_2}} \tag{A.26}$$

As expected, the magnetic field sensitivity of a spin echo based AC measurement is limited by T_2 rather than T_2^* as in the Ramsey based DC measurement. Typical spin echo coherence times in high-purity samples are on the order of $\sim 500\,\mu$s, though T_2 times on the order of ~ 2 ms have been observed in high-purity isotopically engineered samples [1].

Appendix B

Experimental Apparatus

B.1 CCD based wide-field fluorescence microscope

NV ensemble measurements were performed using a custom-built wide-field fluorescence microscope (see Figure B.1), a setup which has been used both for averaging the collective behavior of a large number of NV centers over a several-cubic-micron detection volume as well as for imaging NV behavior over large fields of view. In particular, the latter modality allowed for the demonstrations of 2-dimensional magnetic field imaging with thin-layer NV-diamond samples discussed in Chapter 4.

Optical excitation was provided by a 3-W 532-nm laser (Laser Quantum Opus) which illuminated a region of interest on the diamond surface through a $20\times$ NA $=$ 0.75 objective (Nikon). An acousto-optic modulator (AOM) (Isomet M1133-aQ80L-H) acted as an optical switch, to pulse the laser with precise timing in order to prepare and detect the NV spin states. A loop antenna was positioned near the diamond surface and connected to the amplified (Mini-circuits, ZHL-16W-43-S+) output of a microwave signal generator (Agilent E8257D) to generate a homogeneous MW field over the region of interest. Fast switching of the microwave field (ZASWA-2-50DR) enabled coherent manipulation of the NV spin states necessary for applying standard pulse sequences, such as spin echo and CPMG. Phase modulation of the MW pulses was achieved using an in-phase/quadrature (IQ) mixer (Marki IQ-1545). Optical and MW pulse timings were controlled through a computer-based digital delay generator (SpinCore PulseBlaster PRO ESR500).

NV fluorescence was collected by the objective, filtered through a dichroic mirror (Semrock LM01-552-25) and additional filters, and imaged onto a cooled Charge-Coupled Device (CCD) camera (Starlight Xpress SXV-H9). As the duration of a single measurement is shorter than the minimum exposure time of the camera, the measurement was repeated for several thousand averages within a single exposure
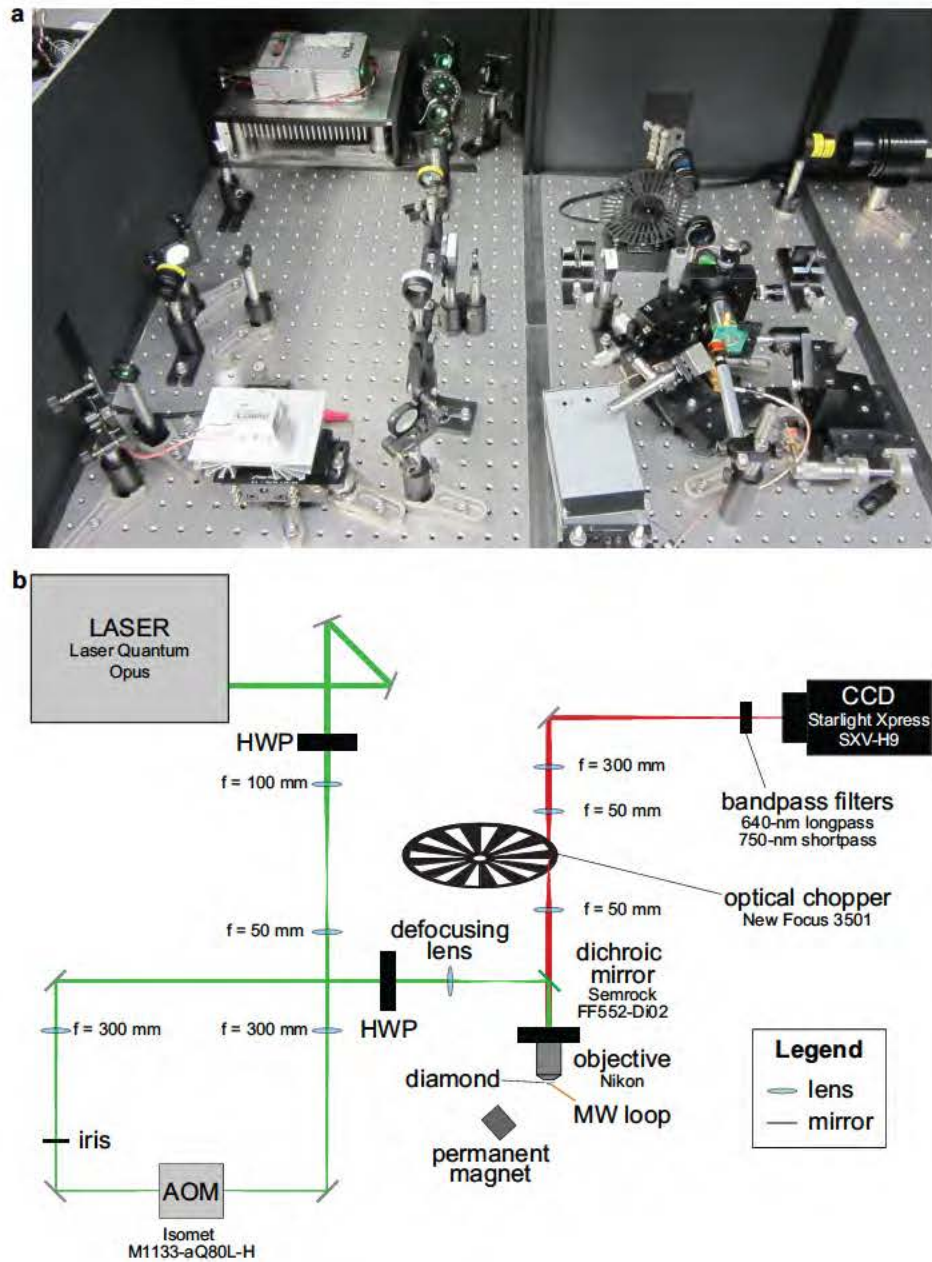
Figure B.1: CCD based wide-field fluorescence microscope (a) photograph and (b) schematic.

and synchronized to an optical chopper (New Focus 3501) placed before the CCD in order to block fluorescence from the optical initialization pulse.

B.2 Scanning confocal microscope

NV measurements on single centers were performed using a custom-built scanning confocal microscope. Optical excitation was provided by a 300-mW 532-nm diode pumped solid-state (DPSS) laser (Changchun New Industries Optoelectronics Tech MLLIII532-300-1), focused onto the sample using a $100\times$, NA = 1.3 oil immersion objective (Nikon CFI Plan Fluor 100x oil). The excitation laser was pulsed by focusing it through an AOM (Isomet 1205C-2). NV fluorescence was collected through the same objective and separated from the excitation beam using a dichroic filter (Semrock LM01-552-25). The light was additionally filtered (Semrock LP02-633RS-25) and focused onto a single-photon counting module (Perkin-Elmer SPCM-ARQH-12).

MW was delivered to the sample using a 20 μm-diameter wire soldered across the diamond. The wire was driven by an amplified (Mini-circuits ZHL-16W-43-S+) MW synthesizer (Agilent E4428C). Phase modulation of the MW pulses was achieved using an in-phase/quadrature (IQ) mixer (Marki IQ-1545). Microwave and optical pulses were controlled using a computer-based digital delay generator (SpinCore PulseBlaster ESR400).

B.3 Low temperature setup

For NV measurements at low temperatures, the sample was mounted inside a continuous-flow cryostat (Janis ST-500) with active temperature control (Lakeshore 331). Optical excitation was applied with a 532-nm laser beam focused on the diamond surface through a NA = 0.6 air objective. The resulting NV fluorescence was collected through the same objective and directed to a multimode fiber coupled to a single-photon counting module (Perkin-Elmer SPCM-ARQH-12). This semi-confocal experimental setup resulted in a $\sim 30 \ \mu\text{m}^3$ detection volume. Microwave control pulses were delivered to the NV spins using a 70 μm-diameter copper wire at the diamond surface. The wire was driven by an amplified (Mini-circuits ZHL-16W-43-S+) MW synthesizer (Stanford Research Systems SG 384). Phase modulation of the MW pulses was achieved using an in-phase/quadrature (IQ) mixer (Marki IQ-1545). Microwave and optical pulses were controlled using a computer-based digital delay generator (SpinCore PulseBlaster ESR400).
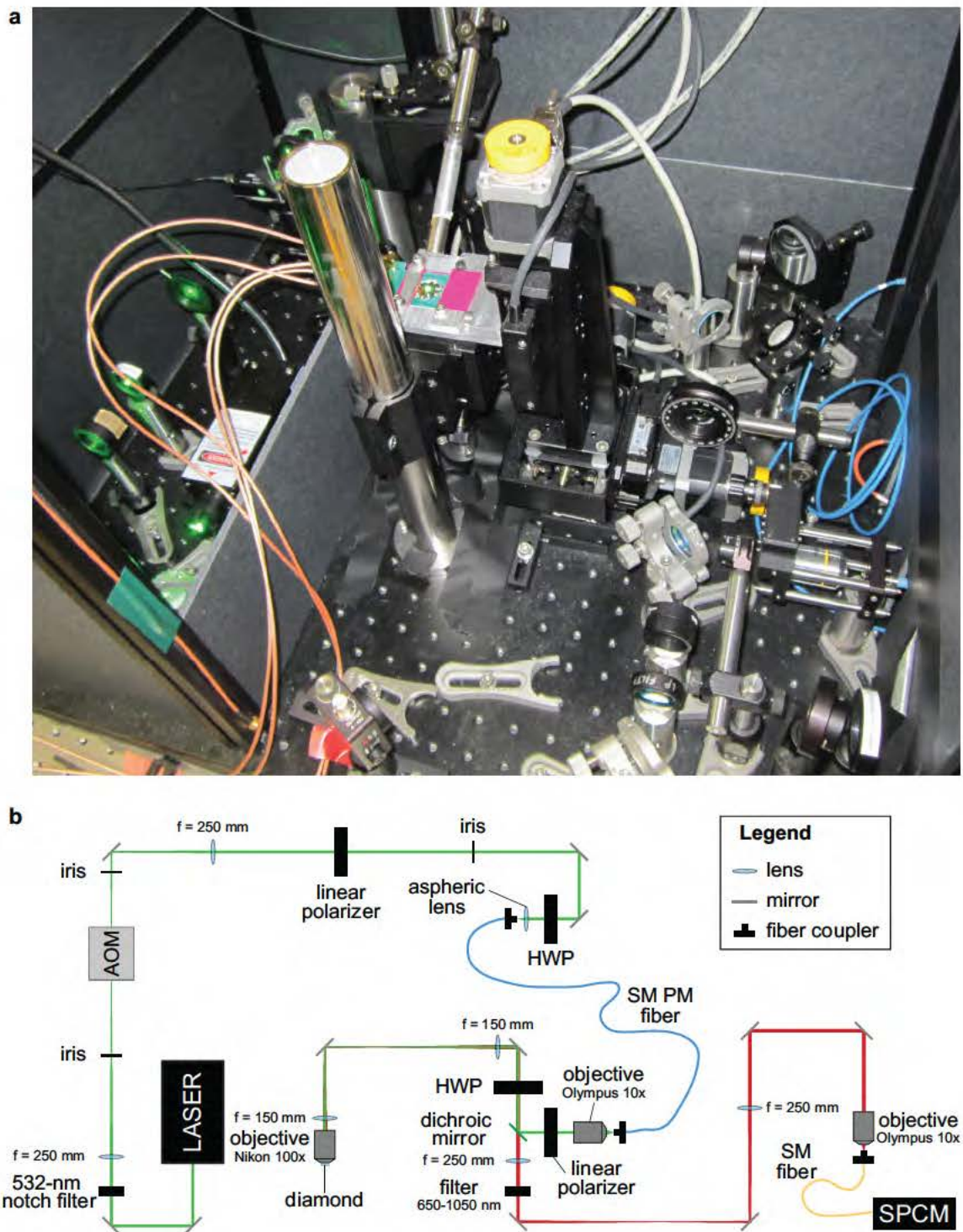
Figure B.2: NV scanning confocal microscope (a) photograph and (b) schematic.

Appendix B: Experimental Apparatus
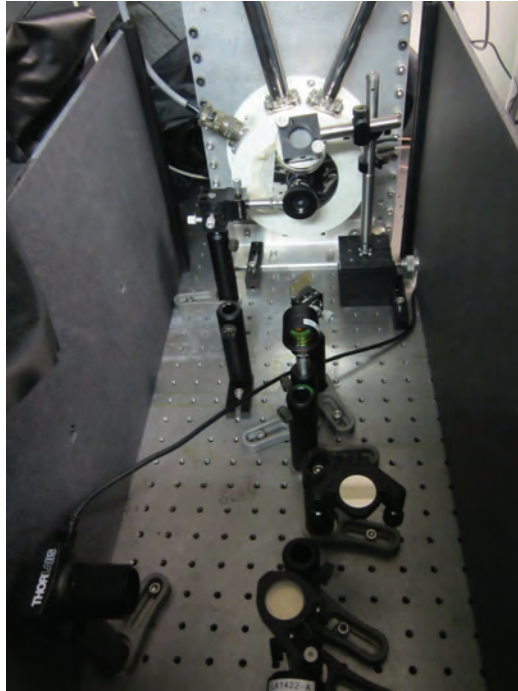
Figure B.3: Photograph of the low temperature NV measurement setup.

Appendix C

Coherence Time T_2 Theoretical Limit

Here we calculate the limit imposed on the coherence time T_2 by the longitudinal relaxation time T_1. (Note that in this discussion, T_2 refers to the general coherence time rather than the coherence time associated with a spin echo measurement as is the convention elsewhere in this dissertation.) For this purpose we assume that there are no direct decoherence processes (i.e., no σ_z noise) and only state-changing (longitudinal) relaxation processes are present.

The analysis is based on generalized Bloch rate equations, assuming that the transition rates are known. The effective decoherence rate between two states $|a\rangle$ and $|b\rangle$, γ_2^{ab}, resulting from longitudinal relaxation is given by [101]:

$$\gamma_2^{ab} = \frac{1}{2} \left(\sum_{k \neq a} \gamma_1^{a \to k} + \sum_{k \neq b} \gamma_1^{b \to k} \right), \tag{C.1}$$

where $\gamma_1^{j \to k}$ is the transition rate from state $|j\rangle$ to state $|k\rangle$.

Two-level system coupled to a zero-temperature bath

First we consider a two-level system, which can decay from state b to state a with rate γ, but has no reverse transitions (from a to b). We can therefore directly write the effective decoherence rate γ_2 using Equation C.1:

$$\gamma_2 = \frac{1}{2}\gamma. \tag{C.2}$$

We can also use rate equations to calculate the actual relaxation rate $\gamma_1 = 1/T_1$ of the two levels:

$$
\begin{aligned}
\dot{p}_a &= \gamma p_b, \\
\dot{p}_b &= -\gamma p_b.
\end{aligned}
\tag{C.3}
$$

Appendix C: Coherence Time T_2 *Theoretical Limit*

The solution is simply

$$
\begin{aligned}
p_a(t) &= 1 - e^{-\gamma t}, \\
p_b(t) &= e^{-\gamma t}.
\end{aligned}
\tag{C.4}
$$

Thus, as expected, we obtain a relaxation rate of $\gamma_1 = \gamma$, and a decoherence rate of $\gamma_2 = \frac{1}{2}\gamma_1$ (which translates into $T_2 = 2T_1$).

Two-level system coupled to an infinite-temperature bath

We next consider the two-level system coupled to an infinite temperature bath, such that transitions are allowed both from state b to state a, as well as from a to b (as would be the case for an electronic spin coupled to a room temperature, solid-state phonon bath). We assume that both transitions occur at a rate γ. Invoking Equation C.1 we find:

$$
\gamma_2 = \frac{1}{2}(\gamma + \gamma) = \gamma.
\tag{C.5}
$$

The rate equations for this system are:

$$
\begin{aligned}
\dot{p}_a &= -\gamma p_a + \gamma p_b, \\
\dot{p}_b &= \gamma p_a - \gamma p_b.
\end{aligned}
\tag{C.6}
$$

Instead of the second equation we can simply use the normalization condition $p_b = 1 - p_a$ to obtain

$$
\dot{p}_a = -\gamma p_a + \gamma(1 - p_a) = \gamma - 2\gamma p_a.
\tag{C.7}
$$

Solving this equation gives:

$$
\begin{aligned}
p_a(t) &= \frac{1}{2}(1 - e^{-2\gamma t}), \\
p_b(t) &= \frac{1}{2}(1 + e^{-2\gamma t}).
\end{aligned}
\tag{C.8}
$$

Thus, the relaxation rate is $\gamma_1 = 2\gamma$, and the decoherence rate is $\gamma_2 = \gamma = \frac{1}{2}\gamma_1$.

This example demonstrates that although the decoherence rate γ_2 is now equal to the transition rate γ (as opposed to being $\frac{1}{2}\gamma$ in the previous example), the relaxation rate γ_1 is also doubled, such that the relation between γ_1 and γ_2 remains the same as before, again yielding $T_2 = 2T_1$.

Three-level system

The NV center is actually a three-level spin system in its electronic ground state, with possible phonon-mediated transitions between the spin levels $|0\rangle$, $|\pm 1\rangle$. For simplicity we assume that all these transitions have the same rate γ, and the corresponding rate equations for two levels involved in our experiment ($|0\rangle$,$|+1\rangle$) are

$$
\begin{aligned}
\dot{p}_0 &= -2\gamma p_0 + \gamma p_{+1} + \gamma p_{-1} \\
\dot{p}_{+1} &= -2\gamma p_{+1} + \gamma p_0 + \gamma p_{-1},
\end{aligned}
\tag{C.9}
$$

with the normalization condition $p_{-1} = 1 - p_0 - p_{+1}$. Substituting the normalization into Equation C.9 we find

$$
\begin{aligned}
\dot{p}_0 &= \gamma - 3\gamma p_0 \\
\dot{p}_{+1} &= \gamma - 3\gamma p_{+1},
\end{aligned}
\tag{C.10}
$$

the solution of which is given by

$$
p_i = A e^{-3\gamma t} + \frac{1}{3},
\tag{C.11}
$$

where $i = \{0, +1\}$ and A is a normalization coefficient. We therefore obtain a relaxation rate of $\gamma_1 = 3\gamma$. According to Equation C.1, the decoherence rate is $\gamma_2 = 2\gamma$, and thus $\gamma_2 = \frac{2}{3}\gamma_1$, yielding $\mathrm{T}_2 = \frac{3}{2}\mathrm{T}_1$.

A more realistic scenario for the NV system assumes no direct transitions between the $|\pm 1\rangle$ states. In this case the rate equations are

$$
\begin{aligned}
\dot{p}_0 &= -2\gamma p_0 + \gamma p_{+1} + \gamma(1 - p_0 - p_{+1}) = -3\gamma p_0 + \gamma \\
\dot{p}_{+1} &= -\gamma p_{+1} + \gamma p_0,
\end{aligned}
\tag{C.12}
$$

using again the normalization condition $p_{-1} = 1 - p_0 - p_{+1}$. Solving this set of equations we find

$$
\begin{aligned}
p_0(t) &= -2C_2 e^{-3\gamma t} + \frac{1}{3}, \\
p_{+1}(t) &= C_1 e^{-\gamma t} + C_2 e^{-3\gamma t} + \frac{1}{3},
\end{aligned}
\tag{C.13}
$$

with normalization coefficients $C_{1,2}$.

Although in this case the resulting relaxation exhibits a double exponential form (at the rates γ and 3γ), the dominant decay will be given by $\gamma_1 = 3\gamma$. Using again Equation C.1, we obtain a decoherence rate of $\gamma_2 = \frac{3}{2}\gamma$, which results in the relation $\gamma_2 = \frac{1}{2}\gamma_1$ and $\mathrm{T}_2 = 2\mathrm{T}_1$. Thus we find that although the dynamics in the three-level system are richer, we always obtain $\gamma_2 < \gamma_1$ and $\mathrm{T}_2 > \mathrm{T}_1$.

Generalization to N levels

If we assume that all state-changing transition rates are equal to γ, then a simple rule can be derived for the decoherence rate γ_2 and the relaxation rate γ_1 of an N-level system:

$$
\begin{aligned}
\gamma_2 &= (N-1)\gamma, \\
\gamma_1 &= N\gamma,
\end{aligned}
\tag{C.14}
$$

which leads to $\gamma_2 < \gamma_1$ and $T_2 > T_1$ for any N.

Appendix D

Diamond Samples

Table D.1: Summary of NV, N, and ^{13}C spin impurity concentrations in each sample employed in this dissertation.

Sample	NV concentration	N concentration	^{13}C concentration
A	$\sim 5 \times 10^{12}$ cm^{-3}	$\gtrsim 1 \times 10^{15}$ cm^{-3}	$\approx 1.1\%$
B	$\sim 1 \times 10^{14}$ cm^{-3}	$\gtrsim 2 \times 10^{16}$ cm^{-3}	$\approx 1.1\%$
C	$\sim 1 \times 10^{14}$ cm^{-3}	$\sim 2 \times 10^{17}$ cm^{-3}	$\approx 0.01\%$
D	$\approx 8 \times 10^{10}$ cm^{-2}	$\approx 1 \times 10^{12}$ cm^{-2}	$\approx 1.1\%$
E	$\sim 3 \times 10^{12}$ cm^{-3}	$\gtrsim 1 \times 10^{15}$ cm^{-3}	$\approx 0.01\%$
F	$\sim 2 \times 10^{16}$ cm^{-3}	$\sim 2 \times 10^{19}$ cm^{-3}	$\approx 1.1\%$
G	$\sim 2 \times 10^{12}$ cm^{-3}	$\sim 1 \times 10^{19}$ cm^{-3}	$\approx 1.1\%$

Sample A

Sample A is a single-crystal diamond sample CVD-grown by Apollo Diamond Inc. The spin impurities are distributed uniformly across the area and thickness of the sample with the following concentrations:

$$
\begin{aligned}
\text{NV concentration} \quad &\sim 5 \times 10^{12} \text{ cm}^{-3} \quad (\sim 0.03 \text{ ppb}) \\
\text{N concentration} \quad &\gtrsim 1 \times 10^{15} \text{ cm}^{-3} \quad (\gtrsim 5 \text{ ppb}) \\
^{13}\text{C concentration} \quad &\approx 1.1\%
\end{aligned}
$$

Sample B

Sample B is a single-crystal diamond sample CVD-grown by Apollo Diamond Inc. The sample consists of a pure diamond substrate with low ambient nitrogen

impurity and $< 10^{12}$ cm^{-3} $(< .006$ ppb$)$ NV density, which was overgrown with a nitrogen-doped layer $\sim 3\,\mu$m thick. Due to the negligible NV concentration in the high-purity substrate, all NV measurements performed on this sample are dominated by the NV centers in the nitrogen-doped layer, whose concentrations of spin impurities are:

$$
\begin{array}{ll}
\text{NV concentration} & \sim 1 \times 10^{14}\ \text{cm}^{-3} \quad (\sim 0.6\ \text{ppb}) \\
\text{N concentration} & \gtrsim 2 \times 10^{16}\ \text{cm}^{-3} \quad (\gtrsim 100\ \text{ppb}) \\
^{13}\text{C concentration} & \approx 1.1\%
\end{array}
$$

Sample C

Sample C is a single-crystal diamond sample CVD-grown on a type 1b HPHT substrate by Element Six. The type 1b HPHT substrate is $\sim 100\,\mu$m thick and contains typical large N ~ 100 ppm and low NV ~ 0.01 ppb concentrations, such that the NV centers in the nitrogen-doped CVD layer dominate measurements. The NV concentration is primarily distributed over $\sim 60\,\mu$m thick layer in the center of the sample, where the estimated spin impurity concentrations are:

$$
\begin{array}{ll}
\text{NV concentration} & \sim 1 \times 10^{14}\ \text{cm}^{-2} \quad (\sim 0.6\ \text{ppb}) \\
\text{N concentration} & \sim 2 \times 10^{17}\ \text{cm}^{-2} \quad (\sim 1\ \text{ppm}) \\
^{13}\text{C concentration} & \approx 0.01\%
\end{array}
$$

Sample D

Sample D is a single-crystal type 2a HPHT diamond synthesized by Sumitomo Electric Industries, Ltd. In order to introduce NV centers into this high-purity diamond, the sample was implanted with 15-keV N$_2^+$ molecular ions while the substrate was cooled to liquid nitrogen temperature. From Monte-Carlo simulations performed by the SRIM software [21], the mean depth of implanted nitrogen atoms is estimated to be ~ 11 nm, with ~ 4 nm vertical straggle. Seven regions of the sample were implanted with different dosages; however in this dissertation work, we only employed one implant region, with spin impurity concentrations given by:

$$
\begin{array}{ll}
\text{NV concentration} & \approx 8 \times 10^{10}\ \text{cm}^{-2} \\
\text{N concentration} & \approx 1 \times 10^{12}\ \text{cm}^{-2} \\
^{13}\text{C concentration} & \approx 1.1\%
\end{array}
$$

Sample E

Sample E is a single-crystal diamond sample CVD-grown by Element Six. The sample was grown in a step-flow mode — as indicated by the observed NV fluorescence striations and terraced surface morphology before polishing — and exhibits nearly complete preferential NV orientation as discussed in Chapter 5. The concentrations of spin impurities in the sample are:

$$
\begin{aligned}
&\text{NV concentration} && \sim 3 \times 10^{12}\,\text{cm}^{-3} && (\sim 0.02\ \text{ppb}) \\
&\text{N concentration} && \gtrsim 1 \times 10^{15}\,\text{cm}^{-3} && (\gtrsim 6\ \text{ppb}) \\
&{}^{13}\text{C concentration} && \approx 0.01\%
\end{aligned}
$$

Sample F

Sample F is a single-crystal diamond sample CVD-grown by Apollo Diamond Inc. The sample consists of a pure diamond substrate with low ambient nitrogen and NV impurity concentrations, which was overgrown with a nitrogen-doped layer $\sim 10\,\mu$m thick. Due to the negligible NV concentration in the high-purity substrate, all NV measurements performed on this sample are dominated by the NV centers in the nitrogen-doped layer, whose concentrations of spin impurities are:

$$
\begin{aligned}
&\text{NV concentration} && \sim 2 \times 10^{16}\,\text{cm}^{-3} && (\sim 0.1\ \text{ppm}) \\
&\text{N concentration} && \sim 2 \times 10^{19}\,\text{cm}^{-3} && (\sim 100\ \text{ppm}) \\
&{}^{13}\text{C concentration} && \approx 1.1\%
\end{aligned}
$$

Sample G

Sample G is a single-crystal type 1b HPHT diamond synthesized by Element Six. With no further processing performed on the sample, the concentrations of spin impurities are:

$$
\begin{aligned}
&\text{NV concentration} && \sim 2 \times 10^{12}\,\text{cm}^{-3} && (\sim 0.01\ \text{ppb}) \\
&\text{N concentration} && \sim 1 \times 10^{19}\,\text{cm}^{-3} && (\sim 50\ \text{ppm}) \\
&{}^{13}\text{C concentration} && \approx 1.1\%
\end{aligned}
$$

Bibliography

[1] G. Balasubramanian, P. Neumann, D. Twitchen, M. Markham, R. Kolesov, N. Mizuochi, J. Isoya, J. Achard, J. Beck, J. Tissler, V. Jacques, P. R. Hemmer, F. Jelezko, and J. Wrachtrup, Nature Materials **8**, 383 (2009).

[2] N. Bar-Gill, L. M. Pham, C. Belthangady, D. Le Sage, P. Cappellaro, J. R. Maze, M. D. Lukin, A. Yacoby, and R. L. Walsworth, Nature Communications **3**, (2012).

[3] L. M. Pham, N. Bar-Gill, C. Belthangady, D. Le Sage, P. Cappellaro, M. D. Lukin, A. Yacoby, and R. L. Walsworth, Physical Review B **86**, 045214 (2012).

[4] J. H. N. Loubser and J. A. van Wijk, Diamond Research **11**, 11 (1977).

[5] R. Hanson, O. Gywat, and D. D. Awschalom, Physical Review B **74**, 161203(R) (2006).

[6] A. Gali, Physical Review B **79**, 235210 (2009).

[7] F. P. Bundy, H. T. Hall, H. M. Strong, and R. H. Wentorf, Nature **176**, 51 (1955).

[8] A. M. Edmonds, U. F. S. D'Haenens-Johansson, M. E. Newton, K. M. C. Fu, C. Santori, R. G. Beausoleil, D. J. Twitchen, and M. L. Markham, Physical Review B **86**, 035201 (2012).

[9] A. Chayahara, Y. Mokuno, Y. Horino, Y. Takasu, H. Kato, H. Yoshikawa, and N. Fujimori, Diamond and Related Materials **13**, 1954 (2004).

[10] J. Achard, A. Tallaire, R. Sussmann, and A. Gicquel, Journal of Crystal Growth **284**, 396 (2005).

[11] A. Tallaire, A. T. Collins, D. Charles, J. Achard, R. Sussmann, A. Gicquel, M. E. Newton, A. M. Edmonds, and R. J. Cruddace, Diamond and Related Materials **15**, 1700 (2006).

[12] J. Achard, F. Silva, O. Brinza, A. Tallaire, and A. Gicquel, Diamond and Related Materials **16**, 685 (2007).

[13] H.-D. Li, G.-T. Zou, Q.-L. Wang, S.-H. Cheng, B. Li, J.-N. Lu, X.-Y. Lu, and Z.-S. Jin, Chinese Physics Letters **25**, 1803 (2008).

[14] Q. Liang, C.-S. Yan, Y. Meng, J. Lai, S. Krasnicki, H.-K. Mao, and R. J. Hemley, Diamond and Related Materials **18**, 698 (2009).

[15] K. Ohno, F. J. Heremans, L. C. Bassett, B. A. Myers, D. M. Toyli, A. C. B. Jayich, C. J. Palmstrøm, and D. D. Awschalom, Applied Physics Letters **101**, 082413 (2012).

[16] J. Meijer, B. Burchard, M. Domhan, C. Wittmann, T. Gaebel, I. Popa, F. Jelezko, and J. Wrachtrup, Applied Physics Letters **87**, 261909 (2005).

[17] B. Naydenov, V. Richter, J. Beck, M. Steiner, P. Neumann, G. Balasubramanian, J. Achard, F. Jelezko, J. Wrachtrup, and R. Kalish, Applied Physics Letters **96**, 163108 (2010).

[18] S. Pezzagna, B. Naydenov, F. Jelezko, J. Wrachtrup, and J. Meijer, New Journal of Physics **12**, 065017 (2010).

[19] J. O. Orwa, C. Santori, K. M. C. Fu, B. Gibson, D. Simpson, I. Aharonovich, A. Stacey, A. Cimmino, P. Balog, M. Markham, D. Twitchen, A. D. Greentree, R. G. Beausoleil, and S. Prawer, Journal of Applied Physics **109**, 083530 (2011).

[20] B. K. Ofori-Okai, S. Pezzagna, K. Chang, M. Loretz, R. Schirhagl, Y. Tao, B. A. Moores, K. Groot-Berning, J. Meijer, and C. L. Degen, Physical Review B **86**, 081406(R) (2012).

[21] J. F. Ziegler, J. P. Biersack, and M. D. Ziegler, *SRIM, the stopping and range of ions in matter* (SRIM Co., Chester, MD, 2008).

[22] D. M. Toyli, C. D. Weis, G. D. Fuchs, T. Schenkel, and D. D. Awschalom, Nano Letters **10**, 3168 (2010).

[23] M. S. Grinolds, P. Maletinsky, S. Hong, M. D. Lukin, R. L. Walsworth, and A. Yacoby, Nature Physics **7**, 687 (2011).

[24] S. Pezzagna, D. Rogalla, H.-W. Becker, I. Jakobi, F. Dolde, B. Naydenov, J. Wrachtrup, F. Jelezko, C. Trautmann, and J. Meijer, Physical Status Solidi A **208**, 2017 (2011).

[25] F. C. Waldermann, P. Oliverob, J. Nunna, K. Surmacza, Z.Y. Wanga, D. Jakscha, R.A. Taylora, I.A. Walmsleya, M. Draganskic, P. Reichartb, A.D. Greentreed, D.N. Jamiesond, and S. Prawer, Diamond and Related Materials **16**, 1887 (2007).

[26] C. Santori, P. E. Barclay, K.-M. C. Fu, and R. G. Beausoleil, Physical Review B **79**, 125313 (2003).

[27] K.-M. C. Fu, C. Santori, P. E. Barclay, and R. G. Beausoleil, Applied Physics Letters **96**, 121907 (2010).

[28] E. Kim, V. M. Acosta, E. Bauch, D. Budker, and P. R. Hemmer, Applied Physics Letters **101**, 082410 (2012).

Bibliography

[29] T. Gaebel, M. Domhan, C. Wittmann, I. Popa, F. Jelezko, J. Rabeau, A. Greentree, S. Prawer, E. Trajkov, P. R. Hemmer, and J. Wrachtrup, Applied Physics B **82**, 243 (2006).

[30] P. Neumann, R. Kolesov, B. Naydenov, J. Beck, F. Rempp, M. Steiner, V. Jacques, G. Balasubramanian, M. L. Markham, D. J. Twitchen, S. Pezzagna, J. Meijer, J. Twamley, F. Jelezko, and J. Wrachtrup, Nature Physics **6**, 249 (2010).

[31] J. R. Rabeau, P. Reichart, G. Tamanyan, D. N. Jamieson, S. Prawer, F. Jelezko, T. Gaebel, I. Popa, M. Domhan, and J. Wrachtrup, Applied Physics Letters **88**, 023113 (2006).

[32] I. Aharonovich, C. Santori, B. A. Fairchild, J. Orwa, K. Ganesan, K.-M. C. Fu, R. G. Beausoleil, A. D. Greentree, and S. Prawer, Journal of Applied Physics **106**, 124904 (2009).

[33] Y. Mita, Physical Review B **53**, 11360 (1996).

[34] V. M. Acosta, E. Bauch, M. P. Ledbetter, C. Santori, K.-M. C. Fu, P. E. Barclay, R. G. Beausoleil, H. Linget, J. F. Roch, F. Treussart, S. Chemerisov, W. Gawlik, and D. Budker, Physical Review B **80**, 115202 (2009).

[35] J. Schwartz, S. Aloni, D. F. Ogletree, and T. Schenkel, New Journal of Physics **14**, 043024 (2012).

[36] J. Martin, R. Wannemacher, J. Teichert, L. Bischoff, and B. Köhler, Applied Physics Letters **75**, 3096 (1999).

[37] G. Davies, S. C. Lawson, A. T. Collins, A. Mainwood, and S. J. Sharp, Physical Review B **46**, 13157 (1992).

[38] D. J. Twitchen, personal communication, 2011.

[39] M. W. Doherty, N. B. Manson, P. Delaney, F. Jelezko, J. Wrachtrup, and L. C. L. Hollenberg (unpublished).

[40] L. Robledo, H. Bernien, T. van der Sar, and R. Hanson, New Journal of Physics **13**, 025013 (2011).

[41] L. Childress, M. V. Gurudev Dutt, J. M. Taylor, A. S. Zibrov, F. Jelezko, J. Wrachtrup, P. R. Hemmer, and M. D. Lukin, Science **314**, 281 (2006).

[42] E. Togan, Y. Chu, A. S. Trifonov, L. Jiang, J. Maze, L. Childress, M. V. G. Dutt, A. S. Sørensen, P. R. Hemmer, A. S. Zibrov, and M. D. Lukin, Nature **466**, 730Ű734 (2010).

[43] G. D. Fuchs, V. V. Dobrovitski, D. M. Toyli, F. J. Heremans, C. D. Weis, T. Schenkel, and D. D. Awschalom, Nature Physics **6**, 668 (2010).

[44] G. Waldherr, J. Beck, M. Steiner, P. Neumann, A. Gali, Th. Frauenheim, F. Jelezko, , and J. Wrachtrup, Physical Review Letters **106**, 157601 (2011).

[45] G. D. Fuchs, V. V. Dobrovitski, R. Hanson, A. Batra, C. D. Weis, T. Schenkel, and D. D. Awschalom, Physical Review Letters **101**, 117601 (2008).

[46] N. D. Lai, D. W. Zheng, F. Jelezko, F. Treussart, and J. F. Roch, Applied Physics Letters **95**, 133101 (2009).

[47] F. Dolde, H. Fedder, M. W. Doherty, T. Noebauer, F. Rempp, G. Balasubramanian, T. Wolf, F. Reinhard, L. C. L. Hollenberg, F. Jelezko, and J. Wrachtrup, Nature Physics **7**, 459 (2011).

[48] R. Hanson, V. V. Dobrovitski, A. E. Feiguin, O. Gywat, and D. D. Awschalom, Science **320**, 352 (2008).

[49] M. V. G. Dutt, L. Childress, L. Jiang, E. Togan, J. Maze, F. Jelezko, A. S. Zibrov, P. R. Hemmer, and M. D. Lukin, Science **316**, 1312 (2007).

[50] S. Felton, A. M. Edmonds, M. E. Newton, P. M. Martineau, D. Fisher, D. J. Twitchen, and J. M. Baker, Physical Review B **79**, 075203 (2009).

[51] N. Mizuochi, P. Neumann, F. Rempp, J. Beck, V. Jacques, P. Siyushev, K. Nakamura, D. J. Twitchen, H. Watanabe, S. Yamasaki, F. Jelezko, and J. Wrachtrup, Physical Review B **80**, 041201 (2009).

[52] J. M. Taylor, P. Cappellaro, L. Childress, L. Jiang, D. Budker, P. R. Hemmer, A. Yacoby, R. Walsworth, and M. D. Lukin, Nature Physics **4**, 810 (2008).

[53] C. P. Slichter, *Principles of magnetic resonance* (Springer-Verlag, New York, NY, 1990).

[54] D. Le Sage, K. Arai, D. R. Glenn, S. J. DeVience, L. M. Pham, L. Rahn-Lee, M. D. Lukin, A. Yacoby, A. Komeili, and R. L. Walsworth, Nature **496**, 486 (2013).

[55] H. J. Mamin, M. Kim, M. H. Sherwood, C. T. Rettner, K. Ohno, D. D. Awschalom, and D. Rugar, Science **339**, 557 (2013).

[56] S. Pezzagna J. Meijer J. Du C. A. Meriles F. Reinhard J. Wrachtrup T. Staudacher, F. Shi, Science **339**, 561 (2013).

[57] A. Dréau, M. Lesik, L. Rondin, P. Spinicelli, O. Arcizet, J.-F. Roch, and V. Jacques, Physical Review B **84**, 195204 (2011).

[58] B. J. Maertz, A. P. Wijnheijmer, G. D. Fuchs, M. E. Nowakowski, and D. D. Awschalom, Applied Physics Letters **96**, 092504 (2010).

[59] S. Steinert, F. Dolde, P. Neumann, A. Aird, B. Naydenov, G. Balasubramanian, F. Jelezko, and J. Wrachtrup, Review of Scientific Instruments **81**, 043705 (2010).

[60] R. S. Schoenfeld and W. Harneit, Physical Review Letters **106**, 030802 (2011).

Bibliography

[61] C. A. Meriles, L. Jiang, G. Goldstein, J. S. Hodges, J. Maze, M. D. Lukin, and P. Cappellaro, Journal of Chemical Physics **133**, 124105 (2010).

[62] P. C. Maurer, G. Kucsko, C. Latta, L. Jiang, N. Y. Yao, S. D. Bennett, F. Pastawski, D. Hunger, N. Chisholm, M. Markham, D. J. Twitchen, J. I. Cirac, and M. D. Lukin, Science **336**, 1283 .

[63] L. T. Hall, C. D. Hill, J. H. Cole, and L. C. L. Hollenberg, Physical Review B **82**, 045208 (2010).

[64] G. de Lange, D. Riste, V. V. Dobrovitski, and R. Hanson, Physical Review Letters **106**, 080202), year = 2011, .

[65] J. R. Maze, P. L. Stanwix, J. S. Hodges, S. Hong, J. M. Taylor, P. Cappellaro, L. Jiang, M. V. Gurudev Dutt, E. Togan, A. S. Zibrov, A. Yacoby, R. L. Walsworth, and M. D. Lukin, Nature **455**, 644 (2008).

[66] L. M. Pham, N. Bar-Gill, D. Le Sage, C. Belthangady, A. Stacey, M. Markham, D. J. Twitchen, M. D. Lukin, and R. L. Walsworth, Physical Review B **86**, 121202 (2012).

[67] P. Siyushev, F. Kaiser, V. Jacques, I. Gerhardt, S. Bischof, H. Fedder, J. Dodson, M. Markham, D. Twitchen, F. Jelezko, and J. Wrachtrup, Applied Physics Letters **97**, 241902 (2010).

[68] J. P. Hadden, J. P. Harrison, A. C. Stanley-Clarke, L. Marseglia, Y.-L. D. Ho, B. R. Patton, J. L. O'Brien, and J. G. Rarity, Applied Physics Letters **97**, 241901 (2010).

[69] T. M. Babinec, B. J. M. Hausmann, M. Khan, Y. Zhang, J. R. Maze, P. R. Hemmer, and M. Loncar, Nature Nanotechnology **5**, 195 (2010).

[70] D. Le Sage, L. M. Pham, N. Bar-Gill, C. Belthangady, M. D. Lukin, A. Yacoby, and R. L. Walsworth, Physical Review B **85**, 121202 (2012).

[71] B. Naydenov, F. Dolde, L. T. Hall, C. Shin, H. Fedder, L. C. L. Hollenberg, F. Jelezko, and J. Wrachtrup, Physical Review B **83**, 081201 (2011).

[72] E. Van Oort and M. Glasbeek, Chemical Physics **143**, 131 (1990).

[73] E. Van Oort and M. Glasbeek, Chemical Physics **152**, 365 (1991).

[74] A. Imamoğlu, Physical Review Letters **102**, 083602 (2009).

[75] Y. Kubo, F. R. Ong, P. Bertet, D. Vion, V. Jacques, D. Zheng, A. Dréau, J.-F. Roch, A. Auffeves, F. Jelezko, J. Wrachtrup, M. F. Barthe, P. Bergonzo, and D. Esteve, Physical Review Letters **105**, 140502 (2010).

[76] D. Marcos, M. Wubs, J. M. Taylor, R. Auado, M. D. Lukin, and A. S. Sorensen, Physical Review Letters **105**, 210501 (2010).

Bibliography

[77] J. R. Maze, J. M. Taylor, and M. D. Lukin, Physical Review B **78**, 094303 (2008).

[78] T. A. Kennedy, J. S. Colton, J. E. Butler, R. C. Linares, and P. J. Doering, Applied Physics Letters **83**, 4190 (2003).

[79] S. Takahashi, R. Hanson, J. van Tol, M. S. Sherwin, and D. D. Awschalom, .

[80] A. Gali, M. Fyta, and E. Kaxiras, Physical Review B **77**, 155206 (2008).

[81] T. Gaebel, M. Domhan, I. Popa, C. Wittmann, P. Neumann, F. Jelezko, J. R. Rabeau, N. Stavrias, A. D. Greentree, S. Prawer, J. Meijer, J. Twamley, P. R. Hemmer, and J. Wrachtrup, Nature Physics **2**, 408 (2006).

[82] V. V. Dobrovitski, A. E. Feiguin, D. D. Awschalom, and R. Hanson, Physical Review B **77**, 245212 (2008).

[83] A. Abragam, *Principles of Nuclear Magnetism* (Oxford University Press, USA, New York, NY, 1983).

[84] V. M. Acosta, E. Bauch, A. Jarmola, L. J. Zipp, M. P. Ledbetter, and D. Budker, Applied Physics Letters **97**, 174104 (2010).

[85] L. M. Pham, D. Le Sage, P. L. Stanwix, T. K. Yeung, D. Glenn, A. Trifonov, P. Cappellaro, P. R. Hemmer, M. D. Lukin, H. Park, A. Yacoby, and R. L. Walsworth, New Journal of Physics **13**, 045021 (2011).

[86] P. L. Stanwix, L. M. Pham, J. R. Maze, D. Le Sage, T. K. Yeung, P. Cappellaro, P. R. Hemmer, A. Yacoby, M. D. Lukin, and R. L. Walsworth, Physical Review B **82**, 201201 (2010).

[87] F. Silva, J. Achard, O. Brinza, X. Bonnin, K. Hassouni, A. Anthonis, K. De Corte, and J. Barjon, Diamond and Related Materials **18**, 683 (2009).

[88] P. M. Martineau, S. C. Lawson, A. J. Taylor, S. J. Quinn, D. J. F. Evans, and M. J. Crowder, Gems & Gemology **40**, 2 (2004).

[89] D. C. Hunt, D. J. Twitchen, M. E. Newton, J. M. Baker, T. R. Anthony, W. F. Banholzer, and S. S. Vagarali, Physical Review B **61**, 3863 (2000).

[90] G. de Lange, Z. H. Wang, D. Riste, V. V. Dobrovitski, and R. Hanson, Science **330**, 60 (2010).

[91] C. A. Ryan, J. S. Hodges, and D. G. Cory, Physical Review Letters **105**, 200402 (2010).

[92] H. Y. Carr and E. M. Purcell, Physical Review **94**, 630 (1954).

[93] S. Meiboom and D. Gill, Review of Scientific Instruments **29**, 688 (1958).

[94] A. Jarmola, V. Acosta, K. Jensen, S. Chemerisov, and D. Budker, Physical Review Letters **108**, 197601 (2012).

Bibliography

[95] A. Tyryshkin, S. Tojo, J. Morton, H. Riemann, N. Abrosimov, P. Becker, H.-J. Pohl, T. Schenkel, M. Thewalt, K. Itoh, and S. Lyon, Nature Materials **11**, 143 (2012).

[96] T. Gullion, D. B. Baker, and M. S. Conradi, Journal of Magnetic Resonance **89**, 479 (1990).

[97] G. S. Uhrig, Physical Review Letters **98**, 100504 (2007).

[98] W. Yang and R.-B. Liu, Physical Review Letters **101**, 180403 (2008).

[99] M. P. Ledbetter, K. Jensen, R. Fischer, A. Jarmola, and D. Budker, Physical Review A **86**, 052116 (2012).

[100] A. Ajoy and P. Cappellaro, Physical Review A **86**, 062104 (2012).

[101] C. Cohen-Tannoudji, J. Dupont-Roc, and G. Grynberg, *Atom-Photon Interactions: Basic Processes and Applications*, *Wiley Science Paperback Series* (John Wiley & Sons, Hoboken, NJ, 1998).

[102] M. W. Doherty, F. Dolde, H. Fedder, F. Jelezko, J. Wrachtrup, N. B. Manson, and L. C. L. Hollenberg, Physical Review B **85**, 205203 (2012).

[103] R. de Sousa, in *Electron Spin Resonance and Related Phenomena in Low-Dimensional Structures*, Vol. 115 of *Topics in Applied Physics*, edited by Marco Fanciulli (PUBLISHER, ADDRESS, 2009), pp. 183 220.

[104] J. H. Shim, I. Niemeyer, J. Zhang, and D. Suter, Europhysics Letters **99**, 40004 (2012).

[105] C. Gross, T. Zibold, E. Nicklas, J. Estève, and M. Oberthaler, Nature **464**, 1165 (2010).

[106] C. Gross, H. Strobel, E. Nicklas, T. Zibold, N. Bar-Gill, G. Kurizki, and M. Oberthaler, Nature **480**, 219 (2011).

[107] M. Kitagawa and M. Ueda, Physical Review A **47**, 5138 (1993).

[108] P. Cappellaro and M. D. Lukin, Physical Review A **80**, 032311 (2009).

[109] J. S. Waugh, L. M. Huber, and U. Haeberlen, Physical Review Letters **20**, 180 (1968).

[110] W.-K. Rhim, D. D. Elleman, and R. W. Vaughan, Journal of Chemical Physics **59**, 3740 (1973).

[111] T. van der Sar, Z. Wang, M. Blok, H. Bernien, T. Taminiau, D. Toyli, D. Lidar, D. Awschalom, R. Hanson, and V. Dobrovitski, Nature **484**, 82 (2012).

[112] N. Y. Yao, C. R. Laumann, A. V. Gorshkov, S. D. Bennett, E. Demler, P. Zoller, and M. D. Lukin, Physical Review Letters **109**, 266804 (2012).

[113] G. A. Álvarez and D. Suter, Physical Review Letters **107**, 230501 (2011).

Bibliography

[114] J. Bylander, S. Gustavsson, F. Yan, F. Yoshihara, K. Harrabi, G. Fitch, D. G. Cory, Y. Nakamura, J.-S. Tsai, and W. D. Oliver, Nature Physics **7**, 565 (2011).

[115] I. Almog, Y. Sagi, G. Gordon, G. Bensky, G. Kurizki, and N. Davidson, Journal of Physics B: Atomic Molecular and Optical Physics **44**, 154006 (2011).

[116] J. R. Klauder and P. W. Anderson, Physical Review **125**, 912 (1962).

[117] G. Gordon, N. Erez, and G. Kurizki, Journal of Physics B: Atomic Molecular and Optical Physics **40**, S75 (2007).

[118] E. Barnes, L. Cywiński, and S. Das Sarma, Physical Review B **84**, 155315 (2011).

[119] E. L. Hahn, Physical Review **80**, 580 (1950).

[120] L. Cywiński, R. M. Lutchyn, C. P. Nave, and S. Das Sarma, Physical Review B **77**, 174509 (2008).

[121] J. Medford, L. Cywiński, C. Barthel, C. M. Marcus, M. P. Hanson, and A. C. Gossard, Physical Review Letters **108**, 086802 (2012).

[122] K. M. Salikhov, S. A. Dzuba, and A. M. Raitsimring, Journal of Magnetic Resonance **42**, 255 (1981).

[123] N. Bloembergen, Physica **15**, 386 (1949).

[124] A. M. Portis, Physical Review **104**, 584 (1956).

[125] R. de Sousa and S. Das Sarma, Physical Review B **67**, 033301 (2003).

[126] W. M. Witzel, M. S. Carroll, A. Morello, L. Cywiński, and S. Das Sarma, Physical Review Letters **105**, 187602 (2010).

[127] A. Cox, M. E. Newton, and J. M. Baker, Journal of Physics: Condensed Matter **6**, 551 (1994).

[128] R. C. Barklie and J. Guven, Journal of Physics C: Solid State Physics **14**, 3621 (1981).

[129] J. C. Allred, R. N. Lyman, T. W. Kornack, and M. V. Romalis, Physical Review Letters **89**, 130801 (2002).

[130] R. J. Epstein, F. M. Mendoza, Y. K. Kato, and D. D. Awschalom, Nature Physics **1**, 94 (2005).

[131] N. Bar-Gill, L. M. Pham, A. Jarmola, D. Budker, and R. Walsworth, Nature Communications **4**, (2013).

[132] J. R. Kirtley, M. B. Ketchen, K. G. Stawiasz, J. Z. Sun, W. J. Gallagher, S. H. Blanton, and S. J. Wind, Applied Physics Letters **66**, 1138 (1995).

[133] L. Hao, J. C. Macfarlane, J. C. Gallop, D. Cox, J. Beyer, D. Drung, and T. Schurig, Applied Physics Letters **92**, 192507 (2008).

Bibliography

[134] C. Granata, E. Esposito, A. Vettoliere, L. Petti, and M. Russo, Nanotechnology **19**, 275501 (2008).

[135] A. Finkler, Y. Segev, Y. Myasoedov, M. L. Rappaport, L. Ne'eman, D. Vasyukov, E. Zeldov, M. E. Huber, J. Martin, and A. Yacoby, Nano Letters **10**, 1046 (2010).

[136] S. K. H. Lam, J. R. Clem, and W. R. Yang, Nanotechnology **22**, 455501 (2011).

[137] A. Finkler, D. Vasyukov, Y. Segev, L. Ne'eman, E. O. Lachman, M. L. Rappaport, Y. Myasoedov, E. Zeldov, and M. E. Huber, Review of Scientific Instruments **83**, 073702 (2012).

[138] M. Schmelz, R. Stolz, V. Zakosarenko, T. Schönau, S. Anders, L. Fritzsch, M. Mück, M. Meyer, and H.-G. Meyer, Physica C **482**, 27 (2012).

[139] E. Esposito, C. Granata, M. Russo, R. Russo, and A. Vettoliere, IEEE Transactions on Magnetics **49**, 140 (2013).

[140] V. Cambel, D. Gregušová, R. Kúdela, and S. J. Bending, Journal of Magnetism and Magnetic Materials **272**, 2141 (2004).

[141] A. Sandhu, K. Kurosawa, M. Dede, and A. Oral, Japanese Journal of Applied Physics Part 1 **43**, 777 (2004).

[142] A. Sandhu, A. Okamoto, I. Shibasaki, and A. Oral, Microelectronic Engineering **73-4**, 524 (2004).

[143] K. R. Rostami, Instruments and Experiment Techniques **47**, 809 (2004).

[144] C. W. Hicks, L. Luan, K. A. Moler, E. Zeldov, and H. Shtrikman, Applied Physics Letters **90**, 133512 (2007).

[145] M. Vengalattore, J. M. Higbie, S. R. Leslie, J. Guzman, L. E. Sadler, and D. M. Stamper-Kurn, Physical Review Letters **98**, 200801 (2007).

[146] M. Gierling, P. Schneeweiss, G. Visanescu, P. Federsel, M. Häffner, D. P. Kern, T. E. Judd, A. Günther, and J. Fortágh, Nature Nanotechnology **6**, 445 (2011).

[147] D. Rugar, R. Budakian, H. J. Mamin, and B. W. Chui, Nature **430**, 329 (2004).

[148] H. J. Mamin, T. H. Oosterkamp, M. Poggio, C. L. Degen, C. T. Rettner, and D. Rugar, Nano Letters **9**, 3020 (2009).

[149] V. Shah, S. Knappe, P. D. Schwindt, and J. Kitching, Nature Photonics **1**, 649 (2007).

[150] H. B. Dang, A. C. Maloof, and M. V. Romalis, Applied Physics Letters **97**, 151110 (2010).

[151] W. Clark Griffith, S. Knappe, and J. Kitching, Optics Express **18**, 27167 (2010).

Bibliography

[152] Ricardo Jiménez-Martínez, W. Clark Griffith, Svenja Knappe, John Kitching, and Mark Prouty, Journal of the Optical Society of America B: Optical Physics **29**, 3398 (2012).

[153] D. Wildanger, J. R. Maze, and S. W. Hell, Physical Review Letters **107**, 017601 .

[154] L. Rondin, J.-P. Tetienne, P. Spinicelli, C. Dal Savio, K. Karrai, G. Dantelle, A. Thiaville, S. Rohart, J.-F. Roch, and V. Jacques, Physical Review Letters **100**, 153118 (2012).

[155] P. Maletinsky, S. Hong, M. S. Grinolds, B. Hausmann, M. D. Lukin, R. L. Walsworth, M. Loncar, and A. Yacoby, Nature Nanotechnology **7**, 320Ũ324 .

[156] E. Rittweger, K. Y. Han, S. E. Irvine, C. Eggeling, and S. W. Hell, Nature Photonics **3**, 144 (2009).